VOLUME 13 NUMBER 2 2022 ISSN 2218-7987
eISSN 2409-5508

International Journal of Mathematics and Physics

Al-Farabi Kazakh National University

The International Journal of Mathematics and Physics is a peer-reviewed international journal covering all branches of mathematics and physics. The Journal welcomes papers on modern problems of mathematics and physics, in particular, Applied Mathematics, Algebra, Mathematical Analysis, Differential Equations, Mechanics, Informatics, Mathematical Modeling, Applied Physics, Radio Physics, Thermophysics, Nuclear Physics, Nanotechnology, and etc.

International Journal of Mathematics and Physics is published twice a year by al-Farabi Kazakh National University, 71 al-Farabi ave., 050040, Almaty, Kazakhstan
website: http://ijmph.kaznu.kz/

Any inquiry for subscriptions should be send to:
Prof. Tlekkabul Ramazanov, al-Farabi Kazakh National University
71 al-Farabi ave., 050040, Almaty, Kazakhstan
e-mail: Tlekkabul.Ramazanov@kaznu.kz

EDITORIAL

The most significant scientific achievements are attained through joint efforts of different sciences, mathematics and physics are among them. Therefore, publication of the Journal, which shows results of current investigations in the field of mathematics and physics, will allow wider exhibition of scientific problems, tasks and discoveries. One of the basic goals of the Journal is to promote extensive exchange of information between scientists from all over the world. We propose publishing service for original papers and materials of Mathematical and Physical Conferences (by selection) held in different countries and in the Republic of Kazakhstan. Creation of the special International Journal of Mathematics and Physics is of great importance because a vast amount of scientists is willing to publish their articles and it will help to widen the geography of future dissemination. We will also be glad to publish papers of scientists from all the continents.

The Journal will publish experimental and theoretical investigations on Mathematics, Physical Technology and Physics. Among the subject emphasized are modern problems of Applied Mathematics, Algebra, Mathematical Analysis, Differential Equations, Mechanics, Informatics, Mathematical Modeling, Astronomy, Space Research, Theoretical Physics, Plasma Physics, Chemical Physics, Radio Physics, Thermophysics, Nuclear Physics, Nanotechnology, etc.

The Journal is issued on the base of al-Farabi Kazakh National University. Leading scientists from different countries of the world agreed to join the Editorial Board of the Journal. The Journal is published twice a year by al-Farabi Kazakh National University. We hope to receive papers from many laboratories, which are interested in applications of the scientific principles of mathematics and physics and are carrying out researches on such subjects as production of new materials or technological problems.

IRSTI 41.17.41 https://doi.org/10.26577/ijmph.2022.v13.i2.01

Namrata I. Jain

Maharshi Dayanand College of Arts, Science and Commerce, Mumbai, India
e-mail: namrata.jain.jain2@gmail.com
(Received 18 May 2022; received in revised form 2 December 2022; accepted 15 December 2022)

The early universe scenario in FRW and K-K models: A study

Abstract. The early Universe has been a subject of research for many cosmologists and it is reviewed and analyzed rigorously in cosmology recently. Thermal history and theory of phase transition coordinate us to elucidate the evolution of the Universe at its early stages and is interesting to get a gist of early universe behavior. At phase transition, effective potential plays a significant role for the kinds of transition that occurred during the evolution. The temperature, at which phase transition occurs, can be determined at minimum effective potential. It is also known fact that temperature of the Universe has changed considerably with its evolution. The present work investigates the time-temperature relation in four- dimensional and five-dimensional cosmological models. A comparison of time- temperature relation in FRW model with that of Kaluza-Klein (K-K) model demonstrates that temperature decreases faster in Kaluza-Klein model. The investigation demonstrates the important role played by extra dimension in the study of time-temperature relation at the early Universe scenario.
Keywords: The Early Universe, Phase transition, effective potential, FRW model, Kaluza-Klein cosmology.

Introduction

Man is always curious about secrets of the Universe. Birth of the Universe, Origin, its behavior at early stages are long standing issues which are still being explored by researchers. In this regard, major revolution is caused by Big-Bang theory which is the most successful yet incomplete, as it is unable to explain certain features of the Universe, such as, presence of Dark Matter, Dark Energy, Large Scale Structure, Accelerated Expansion etc. Emergence of the universe from nothing has been an amazing situation. In this regard, Lamaitre has proposed ‘hypothesis of primeval atom’ in 1927 [1]. The theory has also predicted that just after 10^{-37} second when the temperature and pressure had been very high enough to cause cosmic inflation [2]. The Universe was in the soup of matter and radiation which were in thermal equilibrium with each other. Thermal history of the Universe revealed that it had undergone several phase transitions during its evolutions. In this regard, a detail information with deep theoretical analysis have been provided by the published literature [3 – 5]. It is interesting to note that theoretical analysis of thermal history have been done by mechanism of Higg’s boson [3] which has been discovered recently [4]. Weinberg [5] has ingeniously elucidated various stages of phase transitions at the early era of the universe.

First order phase transition is similar to process of thermal equilibrium at bubble walls [6]. If pressure difference across the bubble wall is different than bubble wall can be broken and energy is released which can be in other forms. Consequences of First order transition give rise to formation of domain walls, generation of gravitational waves and other certain topological defects. Cosmic strings are also topological defects which came into existence before the Electro – Weak Transition.

Second Phase transition [7] occurred which resulted in Quark-Gluon -Plasma State at 10^{-6} sec. After Big-Bang, although temperature was not so high, pair production and annihilation was happening that resulted into production of quarks and leptons. Today quarks and leptons are basic building blocks for elementary particles. Baryogenesis [8], i.e. generation of Baryons continued with the evolution of the Universe. It has also seen that Baryogenesis even violated the conservation of baryon number in the process of matter creation so as to have some structure for the Universe. Although matter creation at early stages of the Universe sounds to be appealing but it is found that the natur has preferred matter generation over antimatter creation. In the Universe, matter-antimatter ratio is unequal. This Problem is yet to be solved.

With the time evolution of the Universe, due to pair annihilation it was filled with photons, neutrinos, electrons, protons. The Second Order phase transitions are also called crossover transition that took place at time 10^6 sec where the temperature is about 1 GeV. As Universe expanded, it cooled down so the quarks- Hadron interaction resulted into its appearance in bound form in baryons and mesons. Before this transition, quarks were free to move in space which is called as Quark -Gluon plasma state [9]. The impact of the transition on quarks is to interact in such a way that led to the formations of baryons and mesons. In this way, they became building blocks for Hadrons or baryons. In other words, Second Order Transition led to confinement of Quarks, so also the formation of Hadrons. The inflation caused the Universe to expand continuously. As a result, the temperature of the Universe has fallen to several Kelvin. It had been predicted by several workers [10, 11, 12] that the Universe at very early stages was initially anisotropic, later due to its expansion it becomes isotropic.

There are several effects of the phase transitions in the normal matter. The major effect of the Phase transition is the symmetry breaking. In normal matter, it is observed that water is more symmetric than ice, steam is more symmetric than water. From here, we also observe that symmetry of the matter is related to the temperature. There is more symmetry for high temperature. Thus, for the Universe, a fraction of second after its birth, it was highly symmetric as its temperature was very high. Phase transition is well understood from thermal history of the Universe. Evolution of the Universe with its thermal history has been discussed by Prokopec [13]. Besides phase transition, attempt has been made to unite all forces as it is believed that just before the Big-Bang all forces except gravity are together as per Grand Unified Theory (GUT) which had been first forth by Guth [14-15]. Weinberg [16] has indigenously illustrated these forces which had been later put together as standard model in particle physics. Later on Kaluza in 1921[17] and Klein in 1926 [18] have made indigenous effort for it and propounded Kaluza-Klein theory which proved a milestone for the further development in the early Universe cosmology.

Thermal history successfully depicts evolution of the Universe [19] but the cause of phase transition cannot be understood by it. Theoretical aspects of phase transition have been explained by Toy model [20, 21] which illuminates phase transition by inclusion of effective potential. The theory of phase transition [19-21] provides the relation between effective potential and critical temperature and it has been given by

$$V_{eff}(\varphi,T) = \frac{\lambda}{4}\varphi^4 + \frac{g^3T}{4\pi}\varphi^3 + + \frac{1}{2}\left[\left(\frac{\lambda}{3}+\frac{g^2}{4}\right)T^2 - \lambda v^2\right]\varphi^2 \qquad (1)$$

where λ, v, are constants. g is the charge, φ is gauge potential and T is the temperature. It is also found that effective potential is minimized at critical temperature. There are three minima of potentials observed at different temperatures which are termed as critical temperatures. The order of phase transition depends upon these temperatures. As discussed previously, structure, geometry and present universe scenario are the consequences of phase transitions. The effective potential and critical temperature can be obtained from Friedmann-Robertson-Walker (FRW) model also. The FRW model is also called as steady state model under certain conditions.

Big Bang model had been challenged by 'Steady state model' (FRW) [22]. The Steady state model of the Universe explained the Universe and its behavior with the help of 'Cosmological Principle' which is termed as perfect Cosmological principle. The expansion of the Universe, its isotropic nature, matter creation etc. are well explained by the steady state model. However certain observations created a major setback to steady state model. In this regard, Big-Bang model is proved to be more successful than Steady state model. The observations by Deep space radio telescope indicated that the Universe at its early stages was quite different than the present Universe [23, 24]. Cosmic microwave background for the Universe as per COBE satellite [25, 26] was inferred by which the Universe appeared to be permeated uniformly by Cosmic radiation in background, thus, it appears to be isotropic in present time. Apart from Big-Bang model, higher dimension theory as a consequence of string theory in the field of Cosmology brought a revolution which can be mainly applied in the study of the early Universe [27,28]. Many researchers worked on Kaluza-Klein theory [29-31] and set up the model so as to study the early universe.

Motivated with the above discussion, time-temperature relations have been obtained in Friedmann Robertson Walker (FRW) and Kaluza-Klein (KK) cosmological models in this paper. We have also studied effective potential for four dimensional and five dimensional models. It is observed that with evolution, temperature is decreased. The present study also emphasizes the implication of extra dimension on time temperature.

The organization of the paper is in five sections. We began with Introduction in first section followed by discussion on determination of time-temperature relation in FRW metric in section 2 and in K-K model in section 3. Section 4 comprises of discussion followed by conclusion in the 5th section.

Time-Temperature relation in FRW metric

Friedmann derived field equations in 1922 with the help of Einstein's general theory of relativity in the context of expansion of the universe, assuming homogeneous and isotropic. Universe. These equations are called as Friedmann equations. In 1926 Lemaitre independently carried out the similar work explaining expansion of the universe. Later in 1930s, Robertson and Walker independently obtained metric equation in order to explain complete geometrical properties of the universe. Using Robertson-Walker metric, the Einstein Field Equations (EFE) have been derived which resembled the equations obtained by Friedmann, The cosmological model representing Friedmann equations thus named as Friedmann-Lemaitre-Robertson-Walker cosmological model (FLRW), or FRW model in more general form. The FRW model is also called standard model as it can explain most of the features of the universe as discussed in previous section. Here, let us have a glance at FRW model for the study of time-temperature relation, which will enable us to set up a new model in higher dimension, to be discussed in next section.

Consider FRW metric [32,33] as given below,

$$ds^2 = -dt^2 + \\ +R^2(t)\left[\frac{dr^2}{1-kr^2} + r^2 d\theta^2 + r^2 sin^2\theta d\varphi^2\right] \quad (2)$$

Let $x^0 = -t$, $x^1 = r$, $x^2 = \theta$, $x^3 = \varphi$ are space –time coordinates. In a curved space time, the line element is given as, $ds^2 = g_{ij}dx^i dx^j$ where g_{ij} is a 4×4 metric tensor. k is a curvature constant, $k = 0$ for flat universe, $k = 1$ for closed universe and $k = -1$ for open universe. The Einstein field equations can be obtained from the following Eq. (3)

$$R_j^i - \frac{1}{2}Rg_j^i = -8\pi G T_j^i + \Lambda g_j^i \quad (3)$$

R^i_j – Ricci tensor, R – Ricci scalar, T^i_j – nergy-momentum tensor, Λ – Cosmological constant and G – gravitational constant. Field Equations (Eq. 3) can also be written as,

$$G_j^i = -\frac{8\pi G}{c^2}T_j^i + \Lambda g_j^i \quad (4)$$

where $G_j^i = R_j^i - \frac{1}{2}Rg_j^i$.

Energy momentum tensor T^i_j is represented as given below.

$$T_j^i = (p+\rho)u^i u_j + g_j^i p \quad (5)$$

$$u_i = \frac{dx_i}{dt}$$

is the 4 – vector velocity component such that $\mathbf{u}^i\mathbf{u}_j = -1$, when $i = 0,1,2,3$ (space-time coordinates); p and ρ are pressure and density of matter distribution of the universe, respectively. Hence, from above equation, the energy momentum tensor is given by $T^i_j = (-\rho, p, p, p)$. We have assumed $\hbar = c = 1$ for deriving field equations in accordance with the cosmological principle. Field equations for FRW cosmological model are obtained by solving Eqs (2-5) as follows,

$$3\frac{\dot{R}^2}{R^2} + 3\frac{k}{R^2} = 8\pi G\rho + \Lambda \quad (6)$$

$$2\frac{\ddot{R}}{R} + \frac{\dot{R}^2}{R^2} + \frac{k}{R^2} = -8\pi G p + \Lambda \quad (7)$$

Let $H = \frac{\dot{R}}{R}$ then Eq. (6) and (7) are modified as:

$$3H^2 + 3\frac{k}{R^2} = 8\pi G\rho + \Lambda \quad (8)$$

$$(1-2q)H^2 + 3\frac{k}{R^2} = -8\pi G p + \Lambda \quad (9)$$

In Eq. (9), q is deceleration parameter defined as,

$$q = -\left|\frac{R\ddot{R}}{\dot{R}^2}\right|$$

Here Λ the Cosmological constant plays a significant role in the study of early Universe as it represents Vacuum Energy. At the early stage of the Universe k can be taken zero (k = 0) i.e. the universe at its early stage can be assumed to be flat. In order to find T_C, Λ is assumed to be constant factor at the early universe although it is not really constant which was inferred through the observations recently [34, 35]. To determine T_C, we consider energy conservation $T^i_{j;j} = 0$ which gives the following equation.

$$\dot{\rho} + (\rho + p)3\mathrm{H} = 0 \tag{10}$$

Substituting k=0 and constant Λ in equation (4) and solving it with Eq. (10) we get,

$$\frac{d}{dR}(\rho R^3) + 3pR^2 = 0 \tag{11}$$

For radiation dominated Universe , p = 1/3ρ, substituting p in above equation and solving it, we get $\rho \propto R^{-4}$. let us consider radiation density ρ = U for past epoch in the early era. The radiation density for past epoch R is given by $U = U_0 \frac{R_0^4}{R^4}$ (where U_0, R_0 are the initial radiation energy density and initial epoch at t=0 respectively.

If we consider the early universe as perfect black body then Energy density in the perfect black body is given by

$U = \sigma T^4$,where σ is radiation constant and T is the Temperature of it . In this situation we obtain $= \frac{K}{R}$, where K is constant depending upon σ and constant of proportionality. At very early epoch we neglect Λ as compared to very high temperature. Substituting $\rho = U = \sigma T^4$, Eq.(6) is rewritten as,

$$\frac{\dot{R}^2}{R^2} = \frac{8\pi G\sigma T^4}{3} \tag{12}$$

On substitution of *T = A/R* and assuming at t=0 R=0,

$$R = A\left(\frac{3}{32\pi G\sigma}\right)^{\frac{-1}{4}}\left(t^{\frac{1}{2}}\right) \tag{13}$$

So,

$$T = A\left(\frac{3}{32\pi G\sigma}\right)^{\frac{1}{4}}\left(t^{-\frac{1}{2}}\right) \tag{14}$$

Above equation gives direct relation between T and t. It is known to us that at early stage of the Universe, the particles are relativistic and it is assumed to behave as relativistic gas at high temperature. If particle interaction is slower than expansion rate H [20,21], density is modified as

$$\rho = \frac{\pi^2}{30} g^* T^4 \tag{15}$$

From Eq. (8) considering k=0 and neglecting Λ , we write Eq. (8) as

$$3H^2 = 8\pi G\rho(T) \tag{16}$$

Assuming Plank's mass $M_{pl} = \frac{1}{\sqrt{8\pi G}}$

$$H = \frac{\dot{R}}{R} = \left(\frac{\pi^2}{90}\right)^{\frac{1}{2}} (g^*)^{\frac{1}{2}} \frac{T^2}{M_{pl}^2} \tag{17}$$

As found earlier $T \propto 1/R$ and we can get an expression,

$$R\dot{R} = \left(\frac{\pi^2}{90}\right)^{\frac{1}{2}} (g^*)^{\frac{1}{2}} \frac{1}{8\pi G} \tag{18}$$

Assuming 8πG =1, integrating and rearranging the terms in above equation, we get,

Solving above equation we obtain the following relation between time and temperature

$$t = \sqrt{\frac{90}{\pi^2}} \frac{1}{\sqrt{g^*}}\left(\frac{1}{T^2}\right) \tag{19}$$

In above equation, g^* is number of degrees of freedom of the particles.

Direct information of the critical temperature could not be revealed from Eq.(14) and (19), but Calculations of T_C can be made simple by knowing g^* at the phase transitions. Consider the GUT transition, $g^* = g_b + g_f$ where g_b and g_f are internal degrees of freedom for bosons and fermions respectively. From the Particle Data group [36,37] g^* is calculated as 106.75 at the time of GUT transition while $g^* = 17.25$ at QCD transition. For different g^* at the phase transitions, temperature T_C's are calculated which are different at GUT, electroweak and QCD transitions. The relation (14) is not obeyed strictly at the transitions as it represents continuous t-T variations. In the next section, we obtain the relation between time and temperature for Kaluza-Klein cosmological model.

Time – Temperature relation in Kaluza- Klein Cosmological model

The Kaluza-Klein metric is the $5D$ FRW metric i.e. four dimensional FRW metric with an extra dimension [38,39] which is as given below:

$$ds^2 = -dt^2 + \\ +R^2(t)\left[\frac{dr^2}{1-kr^2} + r^2 d\theta^2 + r^2 sin^2\theta d\varphi^2\right] + \\ +A^2(t)d\psi^2 \quad (20)$$

where, k is a curvature constant equal to 0, 1 , -1 for flat , closed and open universe, respectively. $R(t)$ and $A(t)$ are fourth and fifth dimensional scale factors. The five-dimensional coordinates in above equation are given by $x^0 = t$, and $x^1, x^2, x^3, x^4 = r, \theta, \varphi, \psi$, respectively. Following the Eqs. (3-5) for Kaluza-Klein metric, the field equations are obtained as given below.

$$3\frac{\dot{R}^2}{R^2} + 3\frac{\dot{R}\dot{A}}{RA} + 3\frac{k}{R^2} = 8\pi G\rho + \Lambda \quad (21)$$

$$2\frac{\ddot{R}}{R} + \frac{\dot{R}^2}{R^2} + \frac{k}{R^2} + 2\frac{\dot{R}\dot{A}}{RA} + \frac{\ddot{A}}{A} = -8\pi Gp + \Lambda \quad (22)$$

$$3\frac{\ddot{R}}{R} + 3\frac{\dot{R}^2}{R^2} + 3\frac{k}{R^2} = -8\pi Gp + \Lambda \quad (23)$$

In above field equations A is the extra dimension. For early Universe k can be taken as zero as The Universe is almost flat at very early Universe and assuming Λ is constant, Field equations can easily be solved to get the relation between R and A. In order to get an expression for density, we consider five dimensional energy momentum tensor as $T^i_j = (-\rho, p, p, p, p)$. Energy conservation relation hence obtained as given below.

$$\dot{\rho} + (\rho + p)\left(3\frac{\dot{R}}{R} + \frac{\dot{A}}{A}\right) = 0 \quad (24)$$

As per Cosmological Principal the Universe is filled with perfect fluid so Equation of State for it is given by $p = (\gamma-1)\rho$ so we get an expression as follows

$$\rho = \rho_0 R^{-3\gamma} A^{-\gamma} \quad (25)$$

Here, we assume ansatz $A = R^n$ ('n' is constant) [The universe is anisotropic at its early stages, so $\sigma^2 \propto \theta$, where σ is shear scalar and θ is expansion scalar. Due to this the metric potentials are related by power relations [40]]. Substituting A in Eq. (25), we get,

$$\rho = \rho_0 R^{-\gamma(n+3)} \quad (26)$$

In this case Temperature dependence on scale will be given by

$$T = T_0 R^{-\frac{\gamma(n+3)}{4}} \quad (27)$$

[[$T_0 = \left(\frac{\rho_0}{\sigma}\right)^{1/4}$], σ is the Stefan's constant.]

Assuming $8\pi G = 1$ and neglecting Λ as compared to density and pressure of the universe, Solving field equations (21) – (23) we get,

$$R = d\left[\frac{\gamma(n+3}{2}t - C\right]^{\frac{2}{\gamma(n+3)}} \quad (28)$$

If we assume initial conditions i.e. at $t = t_0$, $R = R_0$, $H = H_0$ we obtain

$$C = \frac{\gamma(n+3)}{2}t_0 - \frac{1}{H_0},$$

$$d = (H_0)^{\frac{2}{\gamma(n+3)}} R_0$$

So time-temperature relation can be obtained as,

$$T = T_0\left[\frac{\gamma(n+3)}{2}H_0(t - t_0) + 1\right]^{-\frac{2}{\gamma(n+3)}} \quad (29)$$

From above equation, temperatures at Radiation dominated phase, matter dominated phase can be determined.

Discussion

Comparing Eq. (14) and Eq. (29) it is observed that in FRW model $T \propto t^{-1/2}$ while in K-K cosmological model, temperature of the universe depends upon n which is an index factor for extra dimension. Since early Universe is supposed to be in radiation dominated phase, so, for radiation dominated phase time-temperature expression depicts dependency of temperature on time. To determine it, consider $\gamma = 4/3$ as universe is radiation dominated at its early stage, therefore equation (23) is modified in the following form.

$$T = T_0\left[\frac{3(n+3)}{2}H_0(t-t_0)+1\right]^{-\frac{3}{2(n+3)}} \quad (30)$$

Irrespective of constants in equations (14) and (29), it is observed that temperature in five dimensional model is lower than that four dimensional model. The temperature in FRW model is proportional to $t^{-1/2}$ while it is proportional to $t^{-3/2(n+3)}$. This can be due to the presence of extra dimension in the early Universe. We also observe that T depends upon γ. Hence at different phases, temperatures of the universe can be calculated. Although above expression explains Time-temperature relation in higher dimension but it does not provide any clue to find critical temperature at the phase transition. To determine critical temperature in five-dimensional Universe, it is necessary to account number of degrees of freedom in five-dimension for both Fermions and Bosons which were supposed to be major Constituents at early stage of the Universe. The work by Dienes et.al, Emel'Yanov [37, 41] had explained the implications of extra dimension for t-T relation in higher dimension by calculating effective potential for four as well as in five-dimensional physics. They have shown that effective potential in four-dimensional has been quite different than that of five-dimensional models. Consequently, critical temperature in five dimensional model has been modified and can be compared with that of in five-dimensional model. Critical temperatures in four-dimensional model and in five-dimensional model have been obtained [41]as:

$$(T_C)_{D=4} = 2\frac{\mu}{\sqrt{\lambda}} \quad (31)$$

and,

$$(T_C)_{D=5} = \left(\frac{2\pi}{3\zeta(3)}\frac{\mu^2}{\lambda r}\right)^{\frac{1}{3}} \quad (32)$$

In above equations μ, and λ are the bare mass term for fermions and bosons and coefficient of quadratic quantum field associated with effective potential respectively. Above equations clearly demonstrates the difference in critical temperatures in four and five dimensional physics.

Conclusions

The Universe at early stages had gone through several phases. Phase transition and Critical temperature at different phases in four as well as five dimensional model are obtained and compared in this paper. It is observed that temperature decreases faster with time in Kaluza-Klein model. The extra dimension plays a very important role during phase transition. It is also observed that that constant lambda Λ (cosmological constant) does not affect time-temperature relation as such at the early stage of the universe. It is well known that the present Universe is expanding and accelerating, so, determination of time – temperature relation for Kaluza-Klein cosmological model with variable cosmological constant can reveal the present universe scenario.

Acknowledgements

My sincere gratitude to anonymous referee for providing me their valuable suggestions for improvement of this manuscript.

References

1. Lemaître, G. "Un univers homogène de masse constante et de rayon croissant, rendant compte de la vitesse radiale des nébuleuses extra-galactiques". *Ann. Soc. Sci. Bruxelles, série A*, (1927): 47–49.
(New English translation and Editorial Note in J.-P. Luminet, *Gen. Rel. Grav*, (2013); 45, 1619.
2. Lamaitre, G. "A Homogeneous Universe of Constant Mass and Increasing Radius accounting for the Radial Velocity of Extra-galactic Nebulæ", *M.N.R.A.S.* (1931): 91, 483
3. Kapusta, J, I, and Gale, C. *Finite-Temperature Field Theory*, Cambridge University Press (2006).
4. "ATLAS; CMS Collaborations, Measurements of the Higgs boson production and decay rates and constraints on its couplings from a combined ATLAS and CMS analysis of the LHC pp collision data at √s = 7 and 8 TeV", *Journal of High Energy Physics* (2016) : 2016 (8): 45. [arXiv:1606.02266 [hep-ex]].
5. Weinberg, S. First Three minutes, Basic books Inc., New York, (1977)
6. Steinhardt, P, J. "Relativistic Detonation Waves and Bubble Growth in False Vacuum Decay", *Phys. Rev. D* (1982): 25, 2074.

7. Ignatius, J. Cosmic phase transitions, [arXiv:hep-ph/9312293v1] (introductory part of Ph.D. dissertation, (1993): pg. 53)

8. Barrow J, D. Turner, M, S. "Baryosynthesis and the origin of galaxies", *Nature Physics*, (1981); 291 (5815), 469–472

9. Van Hove, Léon Charles, Prudent. "Theoretical prediction of a new state of matter, the quark-gluon plasma" 17th International Symposium on Multi-particle Dynamics, Seewinkel, Austria, 16 – 20 Jun 1986, (1987); pp.801–818

10. Smoot G, F. et al. "Structure in the COBE Differential Microwave Radiometer First-Year Maps", *Astrophys. J.* (1992); 396, L1

11. Bennett, C, L. et al. "Cosmic temperature fluctuations from two years of COBE differential microwave radiometers observations", *Astrophys. J.* (1994); 436–423.

12. Ajaiab, M. "Anisotropic to Isotropic Phase Transitions in the Early Universe", arXiv:1202.3668v2 (astro-ph.CO.) (2012)

13. Prokopec, T. "The standard cosmological model", *Lecture notes for cosmology* (http://www.phys.uu.nl/prokopec/2scm.pdf) (2008).

14. Ross, G. *Grand Unified Theories*. Westview Press. (1984); ISBN 978-0-8053-6968-7.

15. Guth, A., Inflationary universe: A possible solution to the horizon and flatness problems, *Phys. Rev. D*, (1981); 23, 347

16. Weinberg, S. "Recent progress in gauge theories of the weak, electromagnetic and strong Interactions", *Rev. Mod. Phys*., (1974); 46, 255

17. Kaluza, T. "Zum Unitätsproblem in der Physik", *Sitzungsber. Preuss. Akad. Wiss. Berlin. (Math. Phys.)*, (1921): 966–972

18. Klein, O. "Quantentheorie und fünfdimensionale Relativitätstheorie", *Zeitschrift für Physik A*. (1926); 37 (12), 895–906.

19. Sticlet, D., "Master Program of Theoretical Physics 'Student Seminar in Cosmology", Drd. Maarten VAN DE MEENT (www.physics.umd.edu/courses/)

20. Gleiser, M. "Phase Transitions in the Universe", (1998): Preprint, arXiv : hep-ph/9803291/v1

21. Rajantie, A. "Proceedings Cosmological Phase Transitions and Topological Defects", Porto, Portugal, [arXiv: hep-ph/03112622003] (2003)

22. Bondi, H. "Gold T. The Steady-State Theory of the Expanding Universe", *M.N.R.A.S.* (1948): 108, 252

23. Hubble E, P. "A Relation between Distance and Radial Velocity among Extra-Galactic Nebulae", *Proc.Nat.Acad. Sci*, (1929): 15, 168

24. Hubble E, P. "Distribution of luminosity in elliptical nebulae". *Ap. J.*, (1930): 71, 231

25. Penzias, A, A, and Wilson R, W. "A Measurement of Excess Antenna Temperature at 4080 Mc/s", *Ap.J.,*; (1965); 142, 419

26. Dicke R, H, and Peebles P, J, E. "Roll P. G., Wilkinson D. T., A Measurement of Excess Antenna Temperature at 4080 Mc/s" , *Ap. J.*, (1965): 142, 414

27. Gubser S, S, and Lykken J, D. "Strings, branes and extra dimensions", World scientific Publishing Co Pte. Ltd. , (2004): ISBN 981-238-788-9

28. Ellis G, F, R, and Maartens, R. and MacCallum M, A, H. *Relativistic Cosmology* ,Cambridge University press, (2012): ISBN 978-0-521-38114-4

29. Bailin, D, and Love A, "Kaluza-Klein theories", *Rep. Prog. Phys.*, (1987): 50, 1087

30. Wesson, Paul, S. *Space–Time–Matter: Modern Kaluza–Klein Theory*, Singapore: World Scientific. (1999): ISBN 978-981-02-3588-8.

31. Appelquist, T, and Chodos, A, and Freund P, G, O. *Modern Kaluza–Klein Theories*, Menlo Park, Cal.: Addison–Wesley. (1987): ISBN 978-0-201-09829-7

32. Mohajan H, K. "Friedmann Robertson-Walker (FRW) model in cosmology", *Journal of environmental treatment techniques*, (2013): 1(3), 158-164

33. Jain, N. and Bhoga S, S. "Friedman-Robertson-Walker model: A study", *Int. J. Math. Phys. Sci. Res*., (2014): 2(2), 70–86

34. Weinberg S. The Cosmological Constant Problem, *Reviews of Modern Physics* (1989): 61 (1), 1–23.

35. Carroll S. M., Press W. H., Turner E. L., The Cosmological Constant, *Annual Review of Astronomy and Astrophysics*. (1992); 30 (1), 499–542.

36. Patrignani C.et al. (Particle Data Group), Big-Bang nucleosynthesis, *Chin. Phys. C*. (2016); 40, 100001.

37. Dienes K. R., Dudas E., Gherghetta T., Riotto A., Cosmological Phase Transitions and Radius Stabilization in Higher Dimensions, *Nucl. Phys. B*, (1999); 543, 387–422, [arXiv: hep-ph/9809406 (1998)]

38. Jain N. I., Bhoga S. S., Khadekar G. S., Implications of time varying cosmological constant on Kaluza- Klein cosmological model, *Int. J. Th. Physics*, (2013); 53, 4416

39. Jain N.I., Bhoga S. S., Kaluza-Klein. Bulk Viscous Cosmological model with time dependent Gravitational constant and cosmological constant, *Int. J. Theo. Phys*., (2015); 54, 2991

40. Collins C.B., Global structure of the Kantowski–Sachs cosmological models, *J. Math. Phys*.(1977); 18, 2116

41. Emel'Yanov V. M. Physics in Multidimensional Spaces and the Beginning of Metagalaxy, *Physics Reports*, (1986); 143, 01

Funded by Al-Farabi KazNU.

IRSTI 29.19.31 https://doi.org/10.26577/ijmph.2022.v13.i2.02

B.Z. Polvonov[1*], Yu.I. Gafurov[1], U.A. Otajonov[1], M.X. Nasirov[2], B.B. Zaylobiddinov[3]

[1]Ferghana branch of Tashkent University of Information Technologies, Ferghana, Uzbekistan
[2]Ferghana Polytechnic Institute, Ferghana, Uzbekistan
[3]Branch of National Research Nuclear University “MEPHI” in Tashkent city, Tashkent, Uzbekistan
*e-mail: bakhtiyorp@mail.ru
(Received 7 October 2022; accepted 15 December 2022)

The specificity of photoluminescence n-CdS/p-CdTe in semiconductor heterostructures

Abstract. The low-temperature (4.2 K) near-band-edge photoluminescence spectrum of a thin fine-grained (h, $d_{cr}\leq 1\mu m$) polycrystalline CdTe layer in an n-CdS/p-CdTe film heterostructure subjected to frontal excitation by an Ar^+ laser with an intensity of ~44 W/cm^2 consists of a dominant intrinsic (e-h) emission band with a half-width Δ_A=10-12 meV and a blue shift $\Delta E_r \approx$ 25 meV of the red edge with respect to E_g, its LO+nLA phonon replica ($\Delta_B\approx$40 meV) with a weak doublet structure, and a wide ($\Delta_D\approx$100 meV) surface-interface luminescence band peaking at a frequency ħω≈1.49 eV. Rear-side illumination of the photoresistive CdS layer in the intrinsic absorption range with an intensity $L_{ill\approx}$ 5.10^2 lx almost completely destroys the e-hband and all related luminescence lines, which are replaced with an asymmetric polariton emission doublet having an exciton resonance frequency ħω≈1.59 eV($\Delta_{ex}\approx$ 25 meV) and a wide line of shallow donor–acceptor pairs ($\Delta_{DAP}\approx$40 meV) at a frequency of ħω≈1.54 eV, whose maximum intensity is almost two orders of magnitude lower than that of the A line in the absence of illumination.
Keywords: photoluminescence, intensity,exiton, polariton, resonance, frequency,asymmetric, emission band.

Introduction

Low-temperature photoluminescence (LTPL) spectroscopy is a rapid nondestructive method for studying the electronic, optical, and photoelectric parameters of polycrystalline semiconductor film structures having photovoltaic properties [1–3].Recently this technique has successfully been applied in fine studies of the characteristics of thin-film *n*-CdS/*p*-CdTe heterojunctions in solar cells, which were aimed at increasing the efficiency and improving the fabrication technology of the cells[4–8] (the polycrystalline *p*-CdTe film is the main absorbing layer in these structures).In particular, the LTPL spectra of the CdTe layer in a CdS/CdTe heterostructure (photocell with an efficiency of ~12%) in dependence of the laser excitation power and temperature were studied in [1-5].

The luminescence was found to shift to the red region of dominant impurity–defect emission at low excitation powers and be located mainly near the exciton emission edge at higher excitation levels.Tuteja M. et al.[1], who usedrear-side illumination by a He–Ne laser (λ =0.6328 μm) of a polycrystalline CdTe/CdS solar cell, observed three characteristic regions in the LTPL (10 K) spectra: (a) radiative transitions of bound excitons in the range from 1.58 to 1.60 eV, (b) a wide band of donor–acceptor pairs (DAPs) near 1.53 eV, and (c) a wide emission band of group defects with multiple phonon replicas in the range from 1.4 to 1.46 eV.

I.Caraman et al. [3] investigated the LTPL (78 K) spectra of thin (3–7 μm) CdTe films (both as-prepared and annealed in the presence of $CdCl_2$ saturated vapor) in a SnO_2/CdS/CdTe/Ni solar cell upon excitation by He–Ne laser radiation with an intensity of ~12 kW/cm^2. They showed that the illumination both from the side of the free CdTe surface and through the interface (heterojunction) gives rise to a wide impurity band peaking at 1.45 eV and a narrower band due to free (1.57–1.58 eV) and localized (1.558 eV) excitons. The exciton emission is barely present upon excitation through the interface, which is explained by the high concentration of mechanical and structural defects in the latter. An analysis of the photoluminescence spectra made it possible to determine the spectrum of recombination levels and estimate the composition of the $CdS_x/CdTe_{1-x}$ interface layer: $x = 0.06$.

Interface emission was also observed in other studies [4–7]. LTPL measurements [4, 5, 7] and LTPL study with electric-field modulation [6] proved the existence of a mixed crystalline CdS_xTe_{1-x}layer with a thickness of ~15 nm (with a low density of nonradiative recombination centers, the formation of which in the high-efficiency CdS/CdTe film solar cell is facilitated to a greater extent by the annealing in the presence of $CdCl_2$ vapor. The wide luminescence line at 1.42 eV is assigned to defect complexes involving the cadmium vacancy V_{Cd}, and the narrow line peaking at 1.59 eV is related to the exciton bound on the neutral acceptor [5-10].

In all the aforementioned studies, the thickness h of polycrystalline CdTe films and the crystallite sizes d_{cr} greatly exceeded the light wavelength λ in the luminescence spectral range under study. However, many recent studies (see, e.g., [8–10]) have shown thin-film n-CdS/p-CdTe heterostructures with characteristic sizes h, $d_{\mathrm{cr}} \sim \lambda$ to be promising elements for solar cells.In this case, thin fine-grained CdTe films obviously acquire properties of photonic microcrystals, theLTPL of which has barely been analyzed to date.

Recently we have investigated [11-14] the mechanisms of the formation of LTPL (T = 4.2 K) spectra of thin ($h \approx 0.5 - 0.8\mu\mathrm{m}$) polycrystalline pure CdTe films and indium-doped (CdTe:In) films, obtained by thermal vacuum deposition on glass substrates, in dependence of the presence of point and structural defects. It was shown that, in contrast to single crystals [12] and large-crystallite polycrystals [13, 15], the LTPL spectra of fine-grained ($d_{\mathrm{cr}} \leq 1\mu\mathrm{m}$) films do not exhibit any channels of exciton and DAPs emission. This is obviously caused by the following reasons. First, in the case under consideration, the crystallite size d_{cr} is on the same order of magnitude as the Debye screening length $\ell_{Di} = \left(\frac{2\varepsilon\varepsilon_0\phi_i}{e^2|N_D - N_A|}\right)^{1/2}$ (where ε is the permittivity; ε_0 is the permittivity of free space; e is the elementary charge; N_D and N_A are, respectively, the donor and acceptor concentrations; and φ_i is the height of the surface potential barrier at the crystallite boundaries), and the contribution of the small quasi-neutral crystallite volume to the film LTPL is insignificant. Second, the surface potential barriers of crystallites form internal built-in electrostatic fields in the space charge region (SCR), which leads to spatial separation of photogenerated electron–hole pairs in it and, correspondingly, generation of surface photovoltage and intrinsic luminescence (interbond $e-h$ recombination), correlated by these pairs, of hot photocarriers under the condition

$$\tau_r \leq \tau_0, \tau_M \tag{1}$$

where τ_r, τ_0, and τ_M are, respectively, the radiative, nonradiative, and Maxwell lifetimes. Since the total lifetime of nonequilibrium electron is defined as

$$\frac{1}{\tau} = \frac{1}{\tau_r} + \frac{1}{\tau_0}, \frac{1}{\tau_0} = \frac{1}{\tau_{ex}} + \frac{1}{\tau_{DA}} + \frac{1}{\tau_M} + \frac{1}{\tau_p} + \cdots, \tag{2}$$

are the electron relaxation times from this energy state with the formation of excitons and DAPs, respectively; τ_p is the momentum relaxation time; etc., it is natural that, if the condition

$$\tau_r \ll \tau_{ex}, \tau_{DA} \tag{3}$$

is satisfied, the exciton and DAPs emission channels should be absent in the LTPL spectra in the first approximation; i.e., these channels remain experimentally unobserved against the strong background of the e–h luminescence. However, the situation changes when the condition

$$\tau_r \geq \tau_M \tag{4}$$

is implemented. The main mechanisms of photocarrier removal are nonradiative (e.g., electrical conductivity or surface recombination). Then the direct essential contribution of the radiative recombination of SCR-separated free electrons and holes to the LTPL is weakened, and one can observe weak exciton and DAPs lines in the spectra of thin fine-grained semiconductor films. Here, we propose a nontrivial method for implementing this possibility in an n-CdS/p-CdTe film heterostructure.

Materials and Methods

The purpose of this study was to analyze the mechanisms of the formation of the edge photoluminescence spectrum of thin polycrystalline CdTe layer in an n-CdS/p-CdTe film heterostructure and develop a new optical photoelectric method for detecting weak channels of exciton and DAPs emission. This approach makes it possible to investigate the interface composition and structure for nondestructive monitoring and diagnosing the properties of photovoltaic elements. We observed for the first time the build-up of exciton–polariton and shallow-Daps emission lines for the CdTe layer in the *n*-CdS/*p*-CdTe heterostructure, induced with the aid of additional illumination of the photoresistive CdS layer with intensity $L_{ill} \approx 5 \cdot 10^2$lx.It is believed that illumination of CdS reduces the shunting efficient of the CdTe resistance, weakening the heterojunction electric field and the corresponding exciton Stark effect [15] in the SCR surface crystallites. The Maxwell relaxation time $\tau_M = \varepsilon\varepsilon_0/\sigma_{ph}$ (σ_{ph} is the photoconductivity) of separated photocarriers in the CdTe crystallite volume decreases as well, due to which they leave no radiatively via surface interface levels or due to longitudinal photoconductivity before the radiative *e–h* recombination occurs ($\tau_M < \tau_R$). Specifically this circumstance leads to quenching of all emission lines detected in the absence of illumination and build-up of free-exciton and shallow-DAP lines under additional illumination of the photoresistive CdS substrate.

Results and Discussion

A sharp-interface *n*-CdS/*p*-CdTe film heterostructure (Figure 1) with an active absorbing *p*-CdTe layer was fabricated by thermal vacuum deposition on transparent glass substrate *1* in a unified technological cycle [16]. The lower photoresistive CdS layer (*2*) with an area of 20 × 5 mm^2 and thickness of 0.2–0.4 μm had an electronic conductivity. The multiplicity $K = R_{\text{dark}}/R_{\text{light}}$ of the change in its resistance under illumination by a mercury lamp with $L \approx 10^4$ lx reached $\approx 10^2$–10^3 rel. units. According to the electron micrography data on the transverse cleavage and surface of the CdS film, the latter had columnar structure without pores, the crystallite sizes along the substrate surface turned out to be $d_{cr} \approx 1$–3 μm.The upper *p*-CdTe layer (*3*) of thickness h= 0.5 – 0.8 μm grew at a rate of 1.5–2.0 Å/s at a substrate temperature T_s=423–573 K and had a fine-grained structure (crystallites of cubic modification with sizes $d_{cr} \approx 0.8$–1.0 μm).The active area of the *n*-CdS/*p*-CdTe heterostructure was 70–80 mm^2.

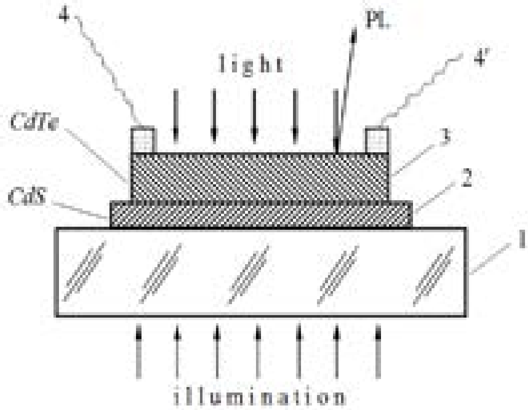

Figure 1 – Schematic diagram of the photoluminescence excitation in the thin CdTe film ($h_f \approx 0.8$ μm) of an n-CdS/p-CdTe heterostructure: (1) transparent glass substrate, (2) CdS photoresistive film ($h_{CdS} \approx 0.3$ μm), (3) photovoltaic layer (CdTe), and (4, 4′) current-collecting ohmic contacts.

To measure the LTPL spectra, the *n*-CdS/*p*-CdTe film heterostructure was directly immersed in pumped liquid helium at a temperature of 4.2 K. Spectra were recorded on a setup based on a DFS-24 spectrometer, operating in the photon-counting mode at a minimum band gap of 0.04 meV. Frontal luminescence excitation (from the free-surface side) of the CdTe layer was performed at a wavelength λ = 476.5 nm by an Ar^+ laser beam focused on the CdTe layer surface into a spot 0.4 × 4 mm in size; the laser power was ∼7 mW. The experiment was performed in the geometry of normal illumination and close-to-normal emission. The rear-side (through the glass substrate, see Figure 1) additional illumination of the CdS layer at different intensities was implemented in the intrinsic absorption range.

Figure 2 shows the photoluminescence spectra of (a)the CdTe layer in an *n*-CdS/*p*-CdTe heterostructure subjected to frontal excitation without CdS illumination and (b) the CdTe layer formed on a pure glass substrate (from [11]); both CdTe layers were grown under identical technological conditions. Note that, in contrast to single crystals [12] and large-crystallite polycrystals [13, 14], theLTPL spectra of fine-grained films exhibit neither exciton nor DAPs emission. Comparison of the spectra in Figures. 2a and 2b show that the presence of a thin polycrystalline CdS layer, which plays a role of a conditional substrate with a heterointerface, is pronounced in only the far edge region.

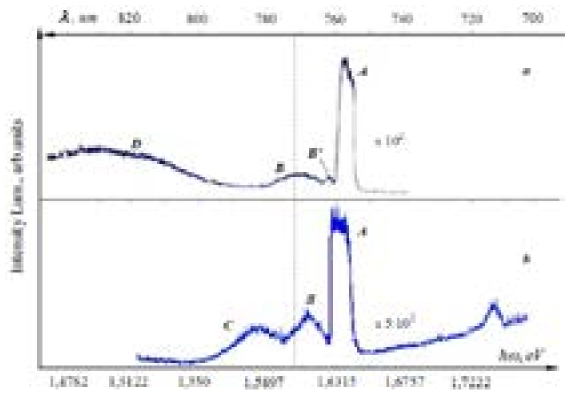

Figure 2 – Photoluminescence spectra of the CdTe layer (a) in an n-CdS/p-CdTe heterostructure in the absence of CdS illumination and (b) on a pure glass substrate; T =4.2 K.

The luminescence spectra of these samples in the range of 750–760 nm qualitatively coincide and consist ofa dominant *e–h* emission band (*A* line) with a half-width of $\Delta E_A \approx 11.2 \pm 0.1$ meV and $\Delta E_A \approx 14.2 \pm 0.1$ meV, respectively. The sharp long-wavelength edges of the *A* lines indicate that the crystallites of the CdTe films grown on both glass and photoresistive substrates have a fairly high bulk structural quality. These edges are shifted above with respect to the bottom of the conduction band (vertical dash-and-dot line) of single crystal at $T = 4.2$ K ($E_g = 1.606$eV) by energies $\Delta E_r \approx 24.4 \pm 0.1$ meV and $\Delta E_r \approx 21.4 \pm 0.1$ meV, so that the sum $\Delta E_r + \Delta E_A = \varphi_0 \approx 35.6 \pm 0.2$ meV remains practically the same for both A lines. The latter is clearly evidenced by the short-wavelength wings of these lines in Figures 2a and 2b.Hence, the following conclusion can apparently be drawn: the φ_0 and$\varphi = \Delta E_r$ values are nothing more but the heights of the surface potential barrier at the crystallite boundary before and after illumination, and ΔE_A is the surface photo-emf, generated by the SCR built-in field (see also [11]).Thus, we have a correlation between the micro photovoltaic property and the intrinsic luminescence of crystallites in thin fine-grained films. Here, we should emphasize the detection of the blue shift of the *A*-line red edge [11], which related to the *e–h* recombination of the hot photocarriers separated by the electric field of interfacial SCR crystallites; this shift is absent in coarse-grained structures [13, 14].

The spectral dependence of the *A*-line intensity can be presented as [11]

$$L(\omega) = A_0(\hbar\omega - E'_g)^{1/2} \exp(-(\hbar\omega - E'_g)/kT_{eh}) \quad (5)$$

where A_0 is a constant, dependent on the type of the film and its photoexcitation conditions; $E'_g = E_g + \Delta E_r$ is the energy of the *A*-line red edge; k is the Boltzmann constant; and T_{eh} is the mean characteristic temperature of photocarriers. Obviously, the second and third factors in the right-hand side of (5) are due to the densities of states in the simple quadratic bands and the quasi-equilibrium photocarrier distribution functions.

As can be seen in Figure 2, the luminescence spectrum of the CdTe layer in the *n*-CdS/*p*-CdTe heterostructure, in contrast to the spectrum of the CdTe monolayer, does not contain any hot-luminescence region in the wavelength range $\lambda < 750$ nm; however, it exhibits an additional relatively strong and wide *D* line of edge luminescence in the range of 790–870 nm, with a half-width $\Delta E_D \approx 120$ meV and a maximum at a frequency $\hbar\omega \approx 1.49$ eV. The energy of this line is lower than E_g by ~40 meV, which is of the same order of magnitude as the ΔE_c value (the discontinuity of the CdTe and CdS conduction band bottoms at the heterojunction interface).

Naturally, one would expect the occurrence of the *D* line of CdTe edge luminescence in *n*-CdS/*p*-CdTe to be due to the contact electric field of the heterojunction, which extracts some part of generated photoelectrons from the *p*-CdTe layer to the surface region of the *n*-CdS layer. These transferred electrons relax in energy to reduce the potential barrier of the heterojunction and undergo radiative tunnel recombination with holes from the *p*-CdTe region or via surface levels E_s (Figure 3); these processes determine the strong broadening of the *D* line, which possesses a long short-wavelength tail and horizontal background. It should be noted that, although the luminescence through the *D* channel is related to only the interface and occurs at a depth equal to the *p*-CdTe layer thickness, it is nevertheless directly correlated by the *A* line, because separated photocarriers in the SCR of *p*-CdTe crystallites contribute to both lines. The quenching of hot luminescence in the spectrum in Figure 2b is also due to the influence of the contact field, possible heterojunction defects, and related crystallite bulk defects on the energy relaxation of hot photocarriers.

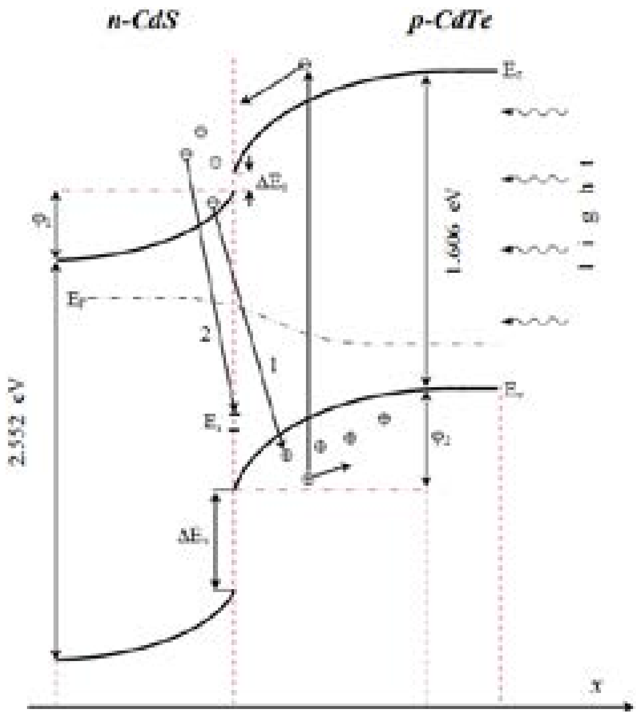

Figure 3 – Schematic energy band diagram of a sharp n-CdS/p-CdTe heterojunction under illumination from the CdTe side and a schematic diagram of the radiative recombination processes (1, 2) leading to the formation of the luminescence D line; T = 4.2 K.

Figure 2a shows also that the long-wavelength wing of the *A* line with a weak doublet fine structure (*B* and *B′* lines) somewhat differs from the similar structure (*B* and *C* lines) of the CdTe monolayer spectrum. The maxima of the *B* and *B′* lines are located at wavelengths of 770 and 762 nm, respectively, and their intensities are almost an order of magnitude lower than the maximum intensity of the *A* line.The mechanisms of the formation of these lines are rather complex. The *B* and *C* lines are most likely the one- and two-LO-phonon replicas of the*A* line [11], although radiative transitions of the "*c*-band → shallow acceptor," "shallow donor → v band,"and "band →crystallite interface levels" types may contribute to their formation. At the same time, it should be noted that, first, the *A*,*B*,*B′*, and *D* lines in the luminescence spectrum of the *p*-CdTe layer in an *n*-CdS/*p*-CdTe heterostructure have not been observed previously by other researchers and, second, their formation obviously involves the luminescence emerging from different depths and the contributions of different structural parts (interface, bulk, surface, barrier regions) of the crystallites forming the fine-grained film.

The illumination of CdS with an intensity L_{ill} = 500 lx leads to a significant transformation of the luminescence spectrum of CdTe layer (Figure 4a). The *A*,*B*,*B′*, and *D* luminescence lines practically disappear. The free-exciton luminescence range of 770–790 nm with a pronounced doublet structure and the DAPs luminescence range of 790.0–820.0 nm can clearly be distinguished. A similar pattern is observed in thereflection spectrum (Figure 4b): the exciton resonance (λ_{ex}=782.5 nm, $\hbar\omega_{ex}$ =1.585 eV) and the DAPs range of 800–812.5 nm.

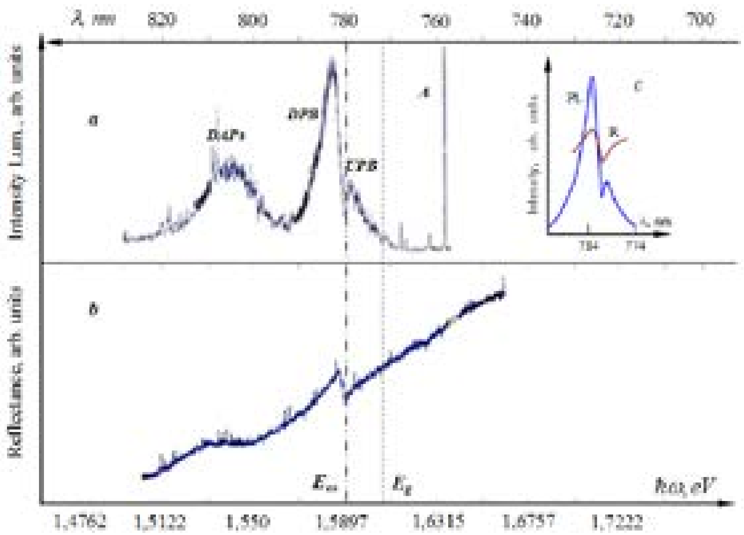

Figure 4 – (a) Photoluminescence spectra of the CdTe layer in an n-CdS/p-CdTe heterostructure with CdS illumination intensity (L_{ill} ≈ 500 lx) and (b) the reflection spectrum of CdTe at T =4.2 K. The inset in panel a shows the photoluminescence (PL) and specular reflection (R) spectra of a CdTe crystal of stoichiometric composition, recorded at T = 77 K [17].

Naturally, the illumination of the CdS region transforms the n-CdS/p-CdTe heterojunction with frontally excited p-CdTe layer into a state similar to that of short-circuited photocell. Depending on the illumination intensity L_{ill}, the surface-barrier height decreases and a short-circuit current arises; specifically this current is responsible for the weakening of the *e–h* emission (luminescence line *A*) and other related emission channels (B,B', and D).At a sufficiently high illumination intensity (L_{ill}≥500 lx),due tothe high photoconductivity of the CdS layer (the condition $\tau_M < \tau_r$is implemented), free photocarriers with energies ħω≥E'_g are almost completely involved in the short-circuit current through the heterojunction. In addition, the CdS illumination weakens the contact electric field of the heterojunction (because of the charge exchange in the surface states), as well as the surface potential barriers of crystallites in the p-CdTe layer. As a result, the exciton and impurity Stark effects (which lead to the luminescence build-up in the exciton and DAPs channels) are weakened. Noteworthy features are the symmetric Lorentzian profile of the DAPs luminescence asymmetric doublet structure of the exciton emission.

For comparison, Figure 4c shows the photoluminescence and reflection spectra of a CdTe crystal with a close-to-stoichiometric composition in the vicinity of free exciton at a temperature of 77.3 K, taken from [17-18].We can see a rather good qualitative coincidence of two spectral lines, although they were recorded for different crystal structures at different temperatures. The spectrum in Figure 4c is adequately described in terms of the quantum polariton luminescence theory developed in [12] with the following values of the main parameters of the exciton resonance $A_{n=1}$ in CdTe crystal: $\hbar\omega_0 = 1.585$eV, $\hbar\omega_{LT} = 1.0$meV, $\hbar\Gamma = 0.62$meV, $M_{ex} = 0.5m_0$ (m_0 is the free-electron mass), background permittivity $\varepsilon_b = 9.65$, and “dead layer” thickness l = 75 Å. The 11-meV red shift of the exciton resonance in the polycrystalline CdTe film under study is explained by the strong damping of mechanical excitons $\hbar\Gamma$,which is caused by the scattering from impurities and grain-boundary potential barriers. Thus, the doublet structure of the exciton luminescence in Figure 4a is described within the polariton model [12-15]. The stronger long-wavelength component peaking at a frequency $\hbar\omega_d$=1.584 eV corresponds to the lower branch polariton emission, and the decisive contribution to the weaker blue satellite peaking at $\hbar\omega_u$=1.590 eV is from the upper branch polariton emission. The dip ("longitudinal") frequency $\hbar\omega_L$=1.588 eV determines the minimum energy of longitudinal excitons.

The symmetric DAPs luminescence profile peaking at the frequency $\hbar\omega_{DA} = 1.540$ eV (λ = 805 nm) has a half-width $\hbar\Delta\omega_{DA} = 33$meVand, in contrast to the spectra of pure crystals [14-19] and the spectra recorded without CdS illumination (Figure

2b), does not contain any inhomogeneous broadening due to the LO replicas. The transitions in a DAPs formed by a shallow donor and a shallow acceptor, whose activation energy is $E_g - \hbar\omega_{\mathrm{DA}} = 1.606 - 1.540 = 0.066$ eV, is responsible for this profile, while the strong homogeneous broadening is due to the strong donor–acceptor interaction in the field of grain boundary potential barriers (and, correspondingly, as a result of the formation of DAPs clusters). The DAPs luminescence occurs mainly in the crystallite barrier regions and in the heterojunction (the CdTe region where photocarriers are separated and, therefore, radiative *e–h* transitions barely exist). The grain boundary potential barriers and donor–acceptor interactions are responsible for the homogeneous broadening of the DAPs emission line.

Conclusions

Thus, using illumination ($L_{\mathrm{ill}} \approx 5 \times 10^2$ lx) of the CdS layer in an *n*-CdS/*p*-CdTe heterostructure, we could detect polariton and shallow-DAPs emission lines from the thin fine-grained CdTe layer. At low illumination levels ($L_{\mathrm{ill}} \leq 5 \times 10^2$ lx), they cannot be clearly selected against the background of the stronger band-to-band emission of the photocarriers separated by the intercrystallite energy field of the high-resistivity polycrystal. The illumination of the CdS layer reduces its shunting resistance, and, correspondingly, the Maxwell relaxation time of separated photocarriers in the crystallite bulk, due to which the photocarriers are pulled in by the heterojunction field before recombining radiatively. Specifically, this circumstance leads to the quenching of the emission lines detected in the absence of illumination and the build-up of the free-exciton and shallow-DAPs lines under illumination.

The *n*-CdS/*p*-CdTe structure elaborated in this work opens new prospects for not only its practical application as a light converter but also for developing new methods of studying photoelectric phenomena in semiconductor micro- and nanostructures.

Acknowledgments

Authors thank the staff of the scientific research laboratory of the Ferghana Polytechnic Institute and the professor of the department of the "Physics" N.Kh. Yuldashev for their scientific advice.

References

1. Tuteja M., Koirala P., Soares J., Collins R., Rockett A. “Low temperature photoluminescence spectroscopy studies on sputter deposited CdS/CdTe junction and solar cells” *Journal of Materials Research* 31(02).(2016):186.

2. Polvonov B.Z., Nasirov M.X., Mirzaev V.T., Razikov J. ”Diagnostika poluprovodnikovix materialov metodom polyaritonnoy lyuminessensii” *General question of world science Collection of scientific papers on materials VII International Scientific Conference.* Izdatelstvo:"Nauka Rossii" *2.(2019):39*

3. Caraman I., Vatavu S., Rusu G., Gasin P. “The luminescence of CdS and CdTe thin films, components of photovoltaic cells”, *Chalcogenide Letters* 3(1).(2006):7.

4. Ikhmayies Sh. J., Ahmad-Bitar R. N. “Interface photoluminescence of the SnO_2:F/CdS:In/CdTe thin film solar cells prepared partially by the spray pyrolysis technique” *Journal of Luminescence* 132(02).(2012):502.

5. Akhmadaliev B.J.,Mamatov O.M., Polvonov B. Z., Yuldashev N.Kh. “Low-temperature photoluminescence of fine-grained CdTe layer in *n*-CdS/*p*-CdTe film heterostructure” *International Journal of Modern Physics and Application* 4(5).(2017):28

6. Nakamura K., Gotoh M., Fujihara T., Toyama T., and et al. “Electromodulated Photoluminescence Study of CdS/CdTe Thin-Film Solar Cell” *Japanese Journal of Applied Physics* 40(1).(2001):4508.

7. Potter M.D., Halliday D.P., Cousins M., Durose K. “Study of the effects of varying cadmium chloride treatment on the luminescent properties of CdTe/CdS thin film solar cells” *Thin Solid Films* 361–362, (2000):248.

8. Kosyachenko L.A., Savchuk A.I., Grushko E.V. “Influence of a thickness of an absorbing layer on efficiency of $CdS/CdTe$ solar cells” *Semiconductors 43*(8). (2009):1060.

9. Ilchuk G.A., Kusnej V.V., Rud V.Yu., Rud Yu.V., Shapoval P.Y., Petrus R.Y. “Photosensitivity of $n-CdS/p-CdTe$ heterotransitions received by chemical superficial sedimentation” *Semiconductors 44*(3).(2010):335.

10. Tuteja M. “Low temperature photoluminescence studies on sputter deposited cadmium sulphide/cadmium telluride heterojunctions and solar sells” *Thesis. University of Illinois at Urbana-Champaing* 31(02). (2014):24.

11. Akhmadaliev B.J., Mamatov O.M., Polvonov B.Z., Yuldashev N.Kh.”Correlation Between the Low-Temperature Photoluminescence Spectra and Photovoltaic Properties of Thin Polycrystalline CdTe Films” *JAMP (USA)* 4(02).(2016):391.

12. Akhmadaliev B.J., Polvonov B.Z., Yuldashev N.Kh. "Influence of Exciton Decay on the Polariton Luminescence Spectra of CdTe Crystal" *Journal of Optics and Spectroscopy* 116(02). (2014):244.

13. Ushakov V.V., Klevkov Yu.V., Dravin V.A. "Ion implantation Er in polycrystalline cadmium telluride", *Semiconductors* 49(5).(2015):644.

14. Bagaev, V.S., Klevlov, Yu.V., Kolosov, S.A., Krivobok, V.S., Shepeli, A.A. "Optical and electrophysical properties of defects in high-purity CdTe" *Physics of the Solid State* 52(01).(2010):37.

15. Polvonov B.Z., Yuldashev N.K. Nasirov M.H., Mirzarakhimova F.K. "Diagnostics of semiconductor materials such as cadmium chalcogenides by the method of low-temperature polariton luminescence" *Journal of International Scientific Review*, *Boston, USA* 11(53).(2018):24.

16. Polvonov B.Z., Yuldashev N.K. "The photo voltage film p-CdTE with the photo responsive-operated substrate n-CdS" *The Third European Conference on Physics and Mathematics, Vienna, Austria*. (2015).12.

17. Akhmadaliev B.J., Mamatov O.M., Polvonov B. Z., Yuldashev N.Kh. "Low-temperature photoluminescence of fine-grained CdTe layer in *n*-CdS/*p*-CdTe film heterostructure" *International Journal of Modern Physics and Application* 4(5).(2017):28.

18. Akhmadaliev B.J., Polvonov B.Z., Yuldashev N.Kh. "Influence of Exciton Decay on the Polariton Luminescence Spectra of CdTe Crystal *"Optics and Spectroscopy* 116 (02).(2014):244.

19. Polvonov B.Z., Nasirov M.X., Polvonov O.Z., Tuychibaev B.K. "Osobennosti povisheniya moshnosti fotovoltaicheskix plenochnix struktur xalkogenidov kadmiya" *Oriental renaissance: Innovative, educational, natural and social sciences* 1(11).(2021):1046

Funded by Al-Farabi KazNU.

IRSTI 89.57.35; 89.53.41 https://doi.org/10.26577/ijmph.2022.v13.i2.03

A.B. Andreyev , V.Yu. Lutsenko* , A.M. Malimbayev

LLP Institute of Ionosphere, Almaty, Kazakhstan
*e-mail: vadim.lutsenko.y@gmail.com
(Received 2 October 2022; accepted 13 December 2022)

A method to determine exact wave parameters of tid

Abstract. Total electron content measurements by using dual-frequency signals of global navigation satellite systems (GNSS) makes it possible to obtain the global distribution of electron density of ionosphere with high spatial and temporal resolution. Such high spatial and temporal resolution allows to explore of small-scale traveling ionospheric disturbances generated by terrestrial geophysical events, including seismic activity, solar terminator passage, and atmospheric cyclones. One of the features of measuring the total electron content of the ionosphere with GNSS is that the measurements are made at the line of intersection of the satellite-receiver beam with the layer of maximum ionization of the ionosphere at height of ≈ 300 km. At the same time, due to the orbital motion of the satellites and the Earth rotation, the ionospheric points at which the measurements are providing carrying out a movement relative to each other, relative to the Earth and relative to the traveling ionospheric disturbances. Such a relative motion of the measurement points causes the occurrence of the Doppler effect and leads to a distortion of the wave parameters of the total electron content variations. In particular, the determination of the period of traveling ionospheric wave disturbances on the basis of time series leads to large distortions depending on the used satellite, the time and coordinates of the receiver. This paper describes a method for determining the exact wave parameters –frequency, wavelength, and propagation velocity of traveling ionospheric wave disturbances, based on the use of godochrones to analyze TEC variations. The difference between the wave parameters measured by the proposed method and from the time series of TEC data is shown on an example of wave disturbances generated by the passage of solar terminator.
Keywords: GPS TEC, ionosphere, data analysis, traveling ionospheric disturbances.

Introduction

The method of measuring the total electron content (TEC) of the ionosphere using navigation satellite systems, also known as the GPS TEC method, has been widely used in recent decades to monitor the influence of various sources of space and terrestrial origin on the Earth's ionosphere. Using this method, the global behavior of the electron density [1,2], the nature of the change in the electron density due to changes in solar activity [3] and other factors have been studied so far, the influence of ground-based sources of disturbances, such as earthquakes [4], powerful explosions, meteorological phenomena, has been discovered [5,6]. A number of anomalous ionospheric disturbances associated with the preparation of powerful earthquakes have been registered [7-9]. All the above sources are presented in TEC data in the form of periodic oscillations of the electron content level, which have a small amplitude relative to the daily TEC change and propagate in horizontal direction, called traveling ionospheric disturbances (TID) [5,10].

The problem of determining the wave characteristics of TID lies in the fact that the ionospheric points at which the TEC is measured move in the horizontal plane during the orbital movement of the satellites and the rotation of the Earth. The ionospheric points for which the TEC is calculated are located at the intersection of the layer of maximum electron density of the ionospheric F2 layer (altitude about 300 km) and the radio beam line from the satellite to the stationary GPS receiver are not fixed relative to the Earth, and their position depends on the orbital motion of satellites and Earth rotation. (Figure 1). The orbits of GPS satellites are located at altitude of about 20000 km, and the orbital period of satellites is about 12 hours [5]. Given this factor, the horizontal speed of the ionospheric points in which the measurement is made can reach 500 km/h, which, due to the Doppler effect, makes it difficult to determine the true period and wavelength of ionospheric disturbances based on data from individual GPS receivers, since the ionospheric point can move along the moving wave disturbance of the ionosphere, in the same or reverse direction, more than doubling the values of its period and wavelength. This effect is determined by the geometry of satellite orbits, geographic latitude and measurement time, i.e. depends on the specific satellite used, time and receiver coordinates [11].

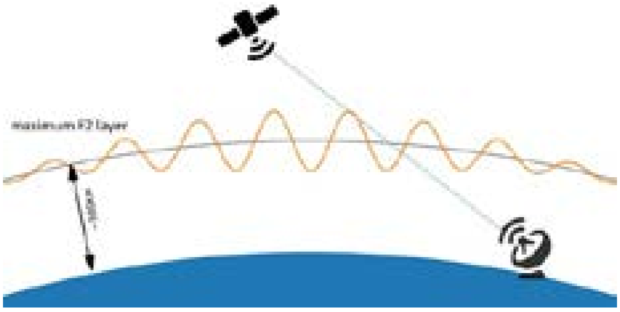

Figure 1 – Illustration of the occurrence of the Doppler effect during TEC measurements

Materials and Methods

The technique proposed in the present study makes it possible to measure the true values of the wave parameters of traveling ionospheric disturbances, its frequency (periods), wavelength, and horizontal velocity. The methods is based on the use of range-time diagrams, also known as hodochrones. Hodochrones are plots on which time is plotted along the abscissa axis, distance is plotted along the ordinate axis. In this case, the range is calculated as the distance between the ionospheric point at a given time and a given point on the Earth's surface. The time series of TEC variations, after removing the regular trend associated with the daily variation of TEC, are plotted with the color of the line, in accordance with the selected color scale. These diagrams are built for all tracks observed for the studied period of time, time series of TEC variations for each pair of satellite-receiver. The distance is plotted along the abscissa axis and calculated by different methods, depending on the type of the studied disturbance source. For quasi point sources (earthquakes, local meteorological phenomena, explosions, etc.), the distance from the point of the epicenter of the earthquake, explosion, cyclone center, etc. to the ionospheric point is calculating. In the case of a point source and in the approximation of spherical wave propagation, the synchronous phases of the wave disturbance will move along the radius vector constructed from the source center, forming a coherent wave pattern on the hodochrone. For extended sources (passage of the solar terminator, global atmospheric phenomena), the "Range" coordinate is calculated as the distance from the ionospheric point to the horizontal line passing through the center of the study area in the direction of propagation of the ionospheric disturbance. In this case, in the case of approaching the propagation of an ionospheric disturbance by a flat wave, a coherent wave pattern will be observed on the hodochrone (Figure 2). In this case, the horizontal cut of the hodochrone gives a temporal sweep of TEC variations, the vertical cut gives a spatial sweep of TEC variations, i.e. wavelength, and the TID velocity is equal to the tangent of the slope angle α of the coherent lines of the TEC variation maxima (Figure 2).

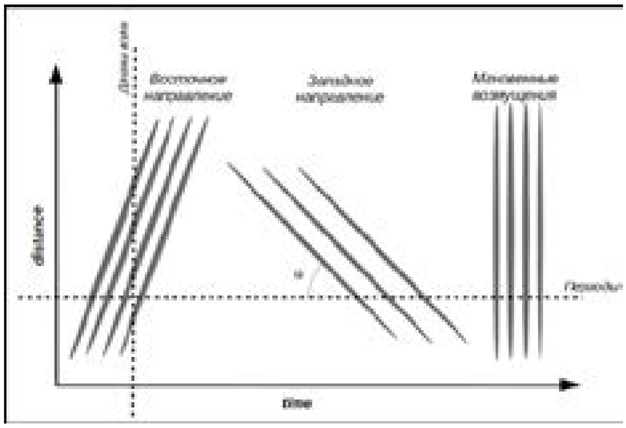

Figure 2 – Information available in the analysis of TEC variations hodochrons

The data used in this work is the data of permanent dual-frequency GNSS receivers (CORS – Continuously Operating Reference Stations), organized into global and regional networks of IGS, UNAVCO, GEONET, etc.

Results and discussion

The following is an example of time series of TEC variations calculated for individual satellites at a given moment and at a given point, and a time series of TEC variations along the horizontal cut of the hodochrone.

Figure 3 shows an example of a hodochrone, which allows illustrating the problem of determining the parameters of wave disturbances. This hodochrone is drawn according to data for April

17, 2018, based on data from GNSS receivers on the US West Coast, and contains a coherent wave pattern of TIDs that arose after the passage of the evening solar terminator. This hodochrone was built for the azimuthal direction 55°, i.e. the distance axis corresponds to the distance along the azimuth of 55°, which coincides with the direction of motion of the considered TIDs. This day is characterized by very low geomagnetic activity, the maximum daily value of the Ap-index was 5, and for the previous day – 4. Low geomagnetic activity causes the absence of irregular disturbances in the data. The disturbance from the solar terminator is directly observed in the interval of 700-800 minutes UT, after which, for nine hours, a coherent TID wave pattern is observed [12]. This hodochron is constructed from the data of all observed GPS satellites.

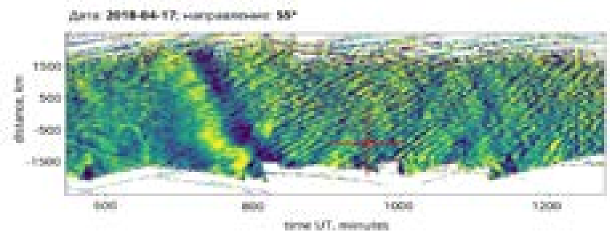

Figure 3 – Fragment of the TEC variations for April 17, 2018

In Figure 3, the red cross indicates the position and time at which the tracks of two GPS prn-26 and GPS prn-7 satellites intersect. The trajectories of these satellites at a given moment of time are such that the ionospheric point for the sounding beam to the prn-26 satellite moves in the same direction as the direction of the TID propagation, and the ionospheric point for the sounding beam to the prn-7 satellite moves in the opposite direction to the direction of the TID propagation direction. Thus, if we consider the ionospheric point at which TEC is calculated as the measurement point, then we have moving receivers, and we observe the Doppler effect. This effect leads to the fact that the time series of TEC variations for these satellites have different observed oscillation periods [13]. Figure 4 shows fragments of the time series for the satellite prn – 26 (upper graph), for the satellite prn – 7 (lower graph), and a slice of the hodochrone along the horizontal line of the red cross in Figure 3. Figure 4 also shows the values of the periods of the first harmonics for all three graphs. It can be seen from the figure that the periods of oscillations of TEC variations for the prn–7 satellite are two times less than the periods for the prn–26 satellite, and are 10.4 and 20.5 minutes, respectively. The oscillation period obtained from the horizontal cut of the hodochrone is 15.7 minutes, and since the Doppler effect is excluded when it is obtained, this period value can be considered true for a given time and place.

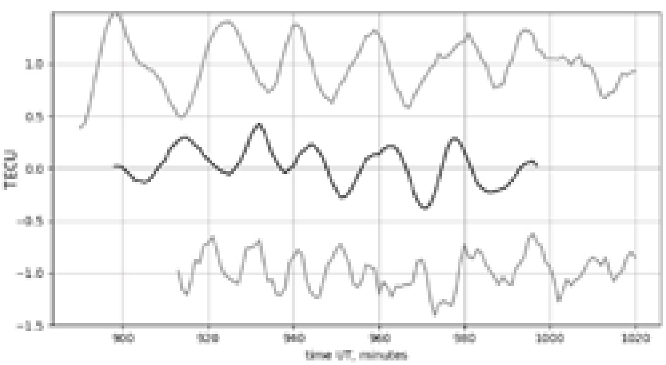

№ GPS satelite	Period (minutes)
26	20.5
26, 7, 9 hodochrone	15.7
7	10.4

Figure 4 – Time series and time slice according to the hodochrone of TEC variations for April 17, 2018

A similar result is observed for any satellites, since the trajectories of the movement of ionospheric points in which the TEC is calculated depend on the complex orbital motion of the satellites and the Earth's rotation (Figure 5).

The TID wavelength is determined in a similar way. To determine it, a vertical (along the distance axis) slice of the hodochrone is taken. So, for the area indicated in Figure 3, the horizontal wavelength of the TID is 170 kilometers.

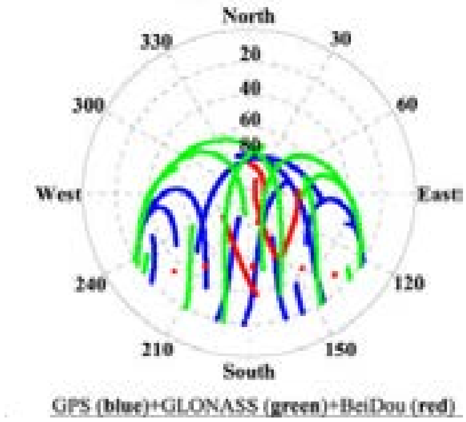

Figure 5 – Trajectories of ionospheric points for various satellites of GPS navigation system.

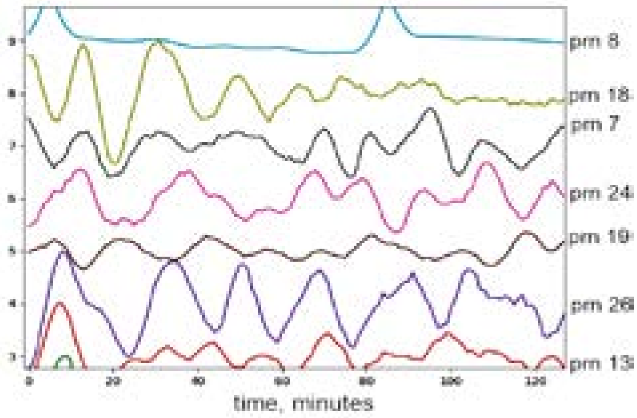

Figure 6 – TEC variations for seven simultaneously visible GPS satellites

The horizontal TID velocity is defined as the tangent of the slope angle α of the coherent lines of the TEC variation maxima. Figure 7 shows the dependence of the signal-to-noise ratio of TEC variations depending on the speed and direction of TID propagation for April 17, 2018 for 15-16 hours UT, which corresponds to the time specified in Figure 3. The maximum signal-to-noise value corresponds to the horizontal velocity of TID propagation ≈ 300 km/h, and direction of propagation 50-60°.

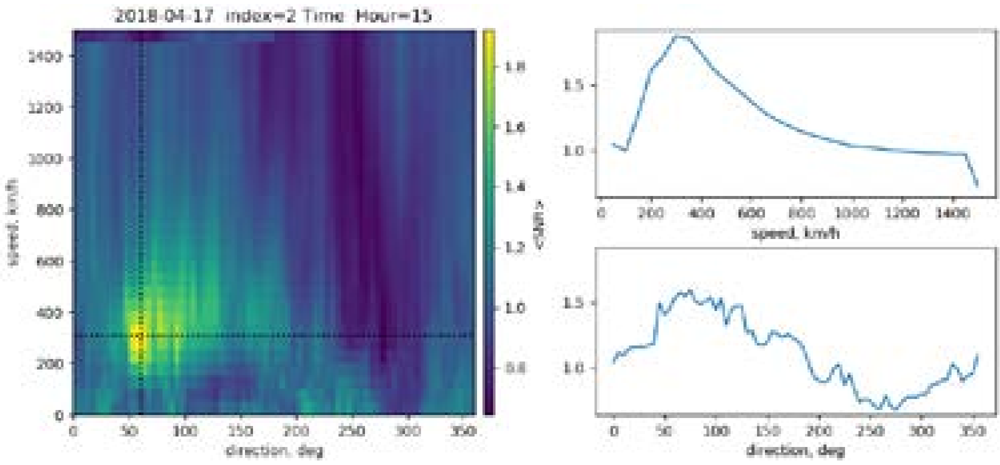

Figure 7 – Distributions of the signal-to-noise ratio of TEC variations depending on the speed and direction of TID propagation for April 17, 2018 for 15-16 hours UT

This signal-to-noise ratio distribution was constructed using the developed system for collecting and analyzing data from GNSS stations [14].

Conclusions

Thus, the applicability of the proposed method for determining the exact wave parameters of moving ionospheric wave disturbances based on the construction of hodochrons – range-time diagrams of TEC variations is shown. It is demonstrated that the direct time series of TEC variations have strong phase and frequency distortions caused by the Doppler effect and are unsuitable for analyzing the frequency characteristics of traveling ionospheric wave disturbances. The proposed method for determining the exact wave parameters of traveling ionospheric wave disturbances is applied in the developing GNSS TEC monitoring system to analyze wave disturbances of the ionosphere from the passage of the solar terminator and other sources.

Acknowledgments

The research work is funded by the Science Committee of the Ministry of Education and Science of the Republic of Kazakhstan (grant No AP09259375).

References

1. Hocke, K. “Oscillations of global mean TEC.” J. Geophys. Res. Volume 113, (2008): A04302.

2. Jakowski, N., Mayer, C., Hoque, M., Wilken, V. “TEC Models And Their Use In Ionosphere Monitoring.” Radio Science. Volume 46, Issue RS0D18. (2011): 1-11.

3. Feng, J., Zhang, Y., Li, W., Han, B., Zhao, Z., Zhang, T., Huang, R. “Analysis of ionospheric TEC response to solar and geomagnetic activities at different solar activity stages.” Advances in Space Research Volume 70, Issue 12. (2022): 78-82.

4. Muslim, B. “Ionospheric earthquake signatures on GPS TEC.” Journal of Physics: Conference Series, Volume 1170, (2019): 012070.

5. Zhang, D.H.; Xiao, Z.; Igarashi, K., Ma, G.Y. “GPS-derived ionospheric total electron content response to a solar flare that occurred on 14 July 2000.” Radio Science Volume 37, Issue 5. (2002): 1086.

6. Astafyeva, E. “Ionospheric detection of natural hazards.” Rev. Geophys. Volume 57, (2019): 1265–1288.

7. Tariq, M., Munawar, S., Hernández-Pajares, M., Talat, I. “Pre-earthquake ionospheric anomalies before three major earthquakes by GPS-TEC and GIM-TEC data during 2015–2017.” Advances in Space Research Volume 63, Issue 7. (2019): 2088-2099.

8. Akhoondzadeh, M. “Anomalous TEC variations associated with the powerful Tohoku earthquake of 11 March 2011.” Nat. Hazards Earth Syst. Sci. Volume 12. (2012): 1453–1462.

9. Dautermann, T., Calais, E., Haase, J., and Garrison, J. “Investigation of ionospheric electron content variations before earthquakes in southern California, 2003–2004.” J. Geophys. Res. Volume 112, (2007): B02106.

10. Nishioka, M., Tsugawa, T., Kubota, M., Ishii, M. “Concentric waves and short-period oscillations observed in the ionosphere after the 2013 Moore EF5 tornado.” Geophys. Res. Lett. Volume 40, (2013): 5581–5586.

11. Zhong, J., Lei, J., Wang, W., Burns, A., Yue, X., Dou X. “Longitudinal variations of topside ionospheric and plasmaspheric TEC.” Journal of Geophysical Research: Space Physics Volume 122, Issue 6. (2017): 6737-6760.

12. Somsikov, V.M. “Solar Terminator and Dynamic Phenomena in the Atmosphere: A Review.” Geomagn. and Aeronomiya Volume 51, (2011): 707–719.

13. Andreyev, A.B. “Dependence of the characteristics of the TEC signal on the angle of inclination of the sounding trajectory.” J. Probl. Evol. Open Syst. Volume 1, (2017): 93–96.

14. Andreyev, A., Kapytin, V., Mukasheva, S., Somsikov, V. “Development of a System for Detecting Traveling Ionospheric Disturbances Based on GNSS Data.” Atmosphere Volume 13, (2022): 183.

IRSTI 41.19.33; 41.51.27; 41.51.29 https://doi.org/10.26577/ijmph.2022.v13.i2.04

A.A. Solodovnik[1]*, P.I. Leontyev[1], S.A. Sartin[1], B.M. Useinov[1], D.V. Alyoshin[1], P. Dalin[2,3]

[1]North Kazakhstan University named after M. Kozybayev, Petropavlovsk, Kazakhstan
[2]Swedish Institute of Space Physics, Kiruna, Sweden
[3]Space Research Institute, RAS, Moscow, Russia
* e-mail: buseinov@gmail.com
(Received 9 May 2022; accepted 16 November 2022)

Physical bases of meteor registration methods and the instrument complex of the NKU Observatory

Abstract. One of the actual directions of studying the physical characteristics of near–Earth space is the assessment of the concentration of meteoroids in it, and the time change of this parameter. In this regard, the principles of setting and implementing meteor observations at the observatory of the North Kazakhstan university named after Manash Kozybayev are considered in chronological order. Meteor observations were carried out on the basis of an integrated approach, including the use of meteor patrols, an All Sky camera, a system for recording radio wave reflections from a remote station from meteor tracks, and a camera based on an optical image intensifier. Based on the analysis of the practical experience of using this equipment, the advantages and disadvantages of each of the methods of meteor registration are revealed. It is shown that the use of the latest image brightness amplifiers and wide–angle cameras with the highest possible sensor sensitivity is the most progressive for their optical observations. The closest attention is paid to the analysis of the experience of implementing the registration of plasma meteor tracks in the radio range. The method is based on the selection of reflected (scattered) musical–speech signals of a remote radio station having a specific pulse structure. Comparison of the obtained results on the frequency of meteor phenomena with the data of known observation points allows us to speak about the effective operation of the newly created meteor monitoring system in the radio range. In the final part of the work, ways to improve the efficiency of recording meteor phenomena in the optical range based on the use of the latest radiation receivers are considered.
Keywords: meteoroids, meteor phenomena, monitoring methods, optical registration, radio observations, instrument complex.

Introduction

Meteor phenomena in the earth's atmosphere that occur when relatively small solid celestial bodies (meteoroids) moving at cosmic speeds invade it have been the subject of scientific research since the end of the XVIII century to the present, and scientific interest in them has not weakened. At the same time, despite significant progress in the development of methods and material base of meteor astronomy, and, as a result, a significant increase in knowledge about the nature and statistics of meteor phenomena, there are a considerable number of important issues that need to be considered.

To a large extent, the existence of such issues (and approaches to their resolution) is due to the stochasticity of the phenomenon. Meteors and fireballs are distinguished by the suddenness of their appearance, which, together with the unpredictability of the direction and the high angular velocity of their movement across the celestial sphere, creates specific problems for their registration and, moreover, for detailed study [1–4].

One of the most important practical tasks of meteor astronomy is the determination of the spatial concentration of meteoroids in the vicinity of the Earth's orbit and its changes in time [5–7]. The value of this quantity is influenced by many cosmic factors. At the same time, knowledge of its magnitude is very important, first of all, from the point of view of the safe functioning of the space infrastructure of modern civilization. In addition to this practically significant task, the problem of the most efficient registration of fireballs for organizing the subsequent search for samples of extraterrestrial matter that fell on the Earth’s surface in the form of meteorites remains topical [3, 8 – 9].

It is impossible to ignore such a promising task as the registration of meteors generated by extremely friable bodies, as well as icy meteoroids. The fact of the existence of friable meteoroids is confirmed by the data of space missions, and ice bodies − by repeated finds of ice meteorites that fell to the Earth. However, the registration of meteors generated by friable, easily evaporated bodies is hardly possible using the instrumentation of modern meteor astronomy [1–2, 10]. The fact is that in the optical range they are not able to radiate intensely enough. And to apply the method of reflection of radio waves, one should hardly expect from them the appearance of plasma tracks with a sufficiently high concentration of free electrons.

It is quite obvious that the complex of these scientific problems and tasks is interconnected. It is also obvious that their solution should be sought through the development and application of various new methods of monitoring the celestial sphere, and monitoring to the maximum extent automated. Our work is devoted to the consideration of the results of efforts to create and material base for monitoring meteor activity and the subsequent study of its capabilities.

Materials and methods

A. Optical observations of meteors at the NKU Observatory

It is paradoxically, but only very recently real alternatives to the human eye in terms of the efficiency of meteor detection appeared. At the same time, the use of visual methods for observing meteors, despite their historical merits, is a thing of the past. The reasons for this are as the high laboriousness of such an observation process, and, unfortunately, the sufficient subjectivity of the data obtained. Therefore, today visual observations can at best be useful in testing the effectiveness of newly created instrument systems.

On the market of scientific instruments, it is difficult to find equipment, which ready for use for meteor observations. Therefore, researchers, as a rule, use for this purpose either astronomical CCD arrays or digital cameras with appropriate short focus optics [11–12]. One of the traditional approaches to the registration of meteors in the optical range is the use of meteor patrols of various designs. The Center for Astrophysical Research (CAR NKU) used a specially made similar equipment. The appearance of the equipment and its scheme are shown in Figure 1. The basis for creating the equipment (Fig. 1) was the Canon 1000D digital cameras [13].

(a)

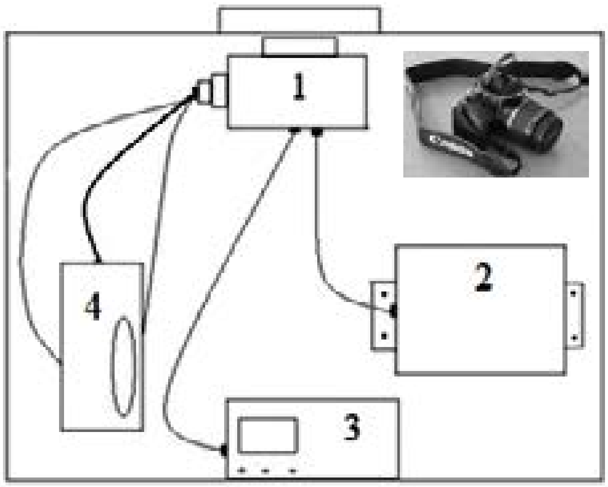

(b)

Figure 1 − Model (a) of the NKU Observatory meteor patrol and scheme (b) of the equipment:
1 − Canon 1000D camera; 2 − exposure control unit; 3 − thermostat; 4 − storage device.

The purpose of the patrol device elements is quite clear. Note that all elements were placed in a case with thermal insulation. At the same time, the thermostat ensured the operation of the equipment at low temperatures, in particular, it protected the optical window from fogging.

The experience of using the installation showed the insufficiently high sensitivity of the cameras, which recorded meteors no weaker than 4 magnitude. In addition, at least 7 recording devices are needed to cover the celestial sphere. This requires the creation of a bulky equipment. This forced us to abandon the further application of the considered construction.

Somewhat later, devices of the celestial sphere (or a significant part of it) panoramic viewing were used in monitoring the celestial sphere. One of them is the Arecont Vision Surround Video 180 panoramic camera, which is used in summer for video recording of the twilight segment of the sky and fields of noctilucent clouds. To eliminate the influence of urban development, the camera was installed on a mast 18 meters high.

The image of objects received by the camera can be output to a computer for real–time observation or recorded in video format. Figure 2 shows the snapshot of the twilight segment taken with the Arecont-Vision SurroundVideo 180 series panoramic camera.

Figure 2 − The snapshot of the twilight segment taken with the ArecontVision SurroundVideo 180 series panoramic camera

However, despite the large viewing angle (180 degrees in azimuth and 33 degrees in altitude), due to insufficient sensor sensitivity the camera proved to be of little use for detecting meteor tracks of moderate brightness. Increasing the sensitivity of this device is achievable by changing the settings of the camera control system to a lower frame rate. In normal mode, the camera frame rate is 1.5 frames per second. In this mode, luminaries with a brightness of at least – 3^m (Venus, Jupiter) are clearly registered. When the frequency is reduced to 0.1 frames per second, it is quite possible to get images of stars and bright meteors. In this case, it is advisable to use at least two panoramic cameras aimed at the zenith, with sensitivity bands orthogonal to one another. Under this condition, most of the meteors with extended tracks will be registered by the system.

Digital photographic cameras with an extremely wide field of view are used to monitor bright meteors and fireballs, during the passage of which meteorites can fall to Earth. To implement this approach, a fisheye lens (Sigma AF, focal length 10 mm, aperture f/2.8) was purchased. This lens used as a feeding optics for the ST 3200 ME matrix (Fig. 3) [14]. The same picture shows a snapshot obtained using this system.

a) b)

Figure 3 − a) Fisheye lens (top) and ST 3200 ME matrix;
b) The image obtained by the camera.
The tower of the RC–30 telescope is visible. A meteor is highlighted with a dotted line.

The use of this registration system is most effective in suburban conditions as far as possible from urban illumination. Therefore, the camera was used to shoot meteors by students and undergraduates living in rural areas during the summer holidays.

The most effective in studying the activity of meteor showers was the use of an optical brightness amplifier (due to the possibility of registering weak meteors). It is known, that even the expression of the brightness of meteors in stellar magnitudes (usual for an astronomer) is fraught with difficulties. Their cause is the movement of meteors. At the same time, visual estimates of the meteors brightness (for all their subjectivity) are closer to reality compared to photographic ones. The explanation lies in the inertia of the visual sensation of the eye, which is not characteristic of most physical light receivers. The light of the star and the part of the meteor track acts on the surface of the radiation receiver during completely different time intervals. For stars, this interval is determined only by the choice of exposure. But the image of the meteor track consists of elements, each of which was exposed to light for a much shorter time. Let's imagine that the meteor track fit on 1000 pixels. The duration of the phenomenon was 0.1 seconds. Then the light acted on each of the pixels for no more than 10^{-4} seconds. In any situation, the effect of the action of a fixed light source will be more pronounced. That is, in order to objectively compare the brightness of meteors and stars, you need to take pictures of stars with exposures of approximately the same duration. In this case, only the rare brightest stars will be displayed on the images. Therefore, photographically we can register only the brightest meteors.

Thus, the study of meteor activity requires the use of either large lenses or technical means (sometimes quite complex in amplifying the light flux [11, 15]). At a certain stage of research, we tried to implement the latter direction by proposing to use an electron–optical converter (EOC) on a microchannel plate MPN–8KM to obtain images of meteor tracks [16].

This is one of the best examples of this type equipment, manufactured by the Novosibirsk Instrument–Making Plant (Fig. 4). The device is designed to observe objects in the dark, with natural illumination from the Moon and stars. Interchangeable lenses allow you to change the magnification from $1^{\times}$ to $4^{\times}$. The electronic circuit of the device provides protection of the EOC from short–term illumination by intense sources. The device can operate in the temperature range ± 40° C.

Figure 4 − General view of the MPN–8KM device − on the left (1 − eyepiece with eyecup; 2 − lens; A − lens focusing unit; 3 infrared filter; 4 − battery pack), on the right is a device with a CANON–600D camera.

Important features of the device, which determine the prospects for its application in meteor observations, are the use of the EOC 2+ generation (microchannel image brightness amplifier), as well as the presence of adapters for attachment to photo and video cameras. According to the passport data of the device, the increase in the brightness of the image reaches 20,000 – 30,000 times. From the point of view of the penetrating power of the optics, this is equivalent to increasing the aperture by hundreds of times. In this case, the field of view is about 36 degrees! This value is comparable to the viewing angle of the human eye in visual observations of meteors.

The first observations with the help of the MPN–8KM instrument were carried out on the night of August 12–13, 2015. The date, the epoch of the Perseid maximum, was chosen in order to obtain images of meteor tracks with the highest probability. The receiver was a CANON–1000D camera. The instruments were placed on an azimuthal tripod, since compensation for the daily movement of the luminaries is not required at short exposures. The survey was conducted with the onset of astronomical night, in the absence of clouds at a point located at a distance of about 6 kilometers from Petropavlovsk. When shooting, exposures from 1.6 to 15 seconds were used.

20 images of satisfactory quality were selected for analysis. At the same time, meteor tracks were confidently detected in 6 images (Fig. 5). It is interesting that in two cases the same meteor was recorded on consecutive images. Perhaps this was possible because thanks to the significant amplification of the MPN8KM device. The system allows you to register the afterglow of a meteor trail, despite the short duration of the phenomenon. When using photographic emulsions, this is practically impossible, due to their low sensitivity.

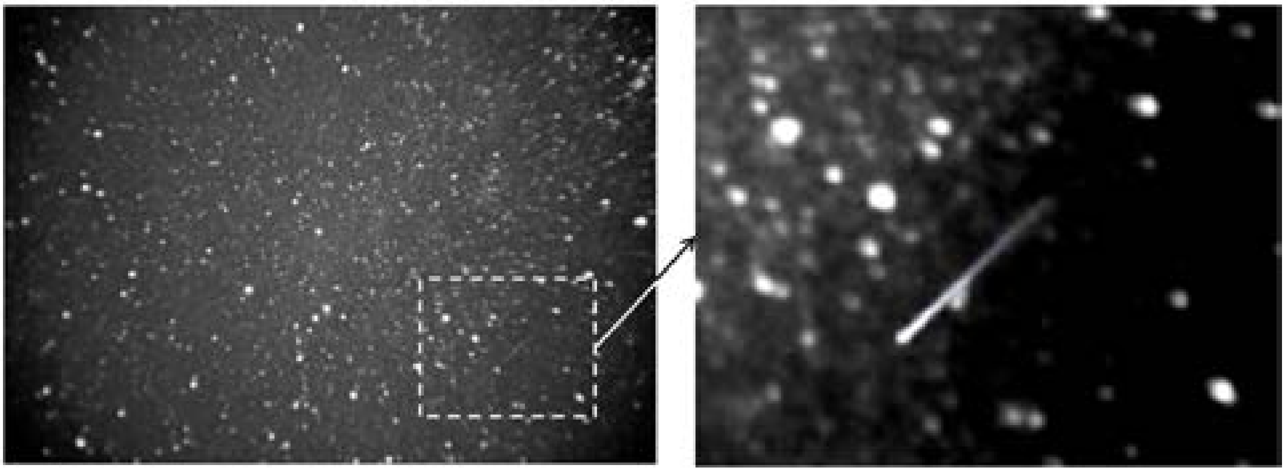

Figure 5 − Image of the starry sky section (the constellation Perseus) 12.08.2015 18h.45m.12s. UTC (exposure 6.0 s). A section with a meteor track is highlighted.

The expected number of meteors in visual observations can be estimated based on the maximum activity of the shower and the height of the radiant [1, 3]. In this case, this number was about 1.3 meteors per minute [16]. Taking into account the size of the observed area (about 30 degrees), this estimate should be reduced to 0.3 meteors per minute. During the total exposure time (159 s), we can expect the registration of approximately one meteor with the naked eye. Photographing meteors on an emulsion would reduce this value by about 4–5 times. It is more difficult to estimate the efficiency of meteor registration by digital cameras. It can be based on a comparison of their sensitivity with photographic emulsions. When shooting the sky, the sensitivity of cameras at the level of 400 – 800 ASA units is used. Taking into account that the sensitivity of astronomical films during long exposures is about 50 ASA units, the number of meteors recorded by a conventional digital camera would be approximately twice as large as in visual observations.

Thus, in the considered experiment, the number of registered meteors exceeds their expected number in visual observations by about 10 times. In comparison with ordinary photographic observations, the gain would be from 30 to 40 times. Even compared to observations with digital cameras, the gain can be up to 4–6 times.

Registration of meteor phenomena in the radio range

Optical methods for observing meteor phenomena are rapidly improving. However, these methods have fundamental limitations − the influence of negative meteorological conditions and illumination of the sky by the Moon. In addition, optical registration of meteors is completely impossible during daylight hours. At the same time, there are quite a lot of meteor showers operating during the daytime [1, 4, 17].

When studying meteor phenomena, their observations in the radio range are most free from photometric and meteorological interference [1, 18–20]. Therefore, in the process of developing the instrument base for meteor observations, a complex, which makes it possible to record meteor tracks in the radio range, was created at the CAR NKU [21].

The physical basis of the method is the existence of a plasma track along the meteor flight path. Such plasma track at altitudes ranging from 100 to 60 km can exist from fractions of a second to tens of seconds, depending on the mass and speed of the body that created the meteor. This is enough to detect a plasma track due to the effect of radio waves reflected from it. Moreover, it becomes possible to study the temporal evolution of the track associated with atmospheric effects on it at high altitudes [1–4]. The ideal for this would be the use of radars. Meteor radar is a good technological approach both for registering the occurrence of a phenomenon, but also for determining the coordinates of an object on the celestial sphere and its speed. However, the required equipment is very specific, its use requires the permission of the special services, and its use in the city is completely prohibited. Therefore, in the practice of a university observatory located in the city, radar observations of meteors are excluded.

There is another approach to the registration of meteor phenomena in the radio range. The functions of the radiation source and the receiver can be separated. The source of radio waves (emitter) can be a powerful radio station operating in the range in which the ionosphere is transparent to radio waves. The observation method is as follows. The transmitting station emits radio waves that scatter on the plasma tracks of meteors. The signal, partially reflected from the track, is accepted by the receiver in the form of a radio pulse, which is then analyzed [18–20, 22].

Then, to register meteors, it is enough to have an external antenna, a sensitive FM (65–108 MHz) radio receiver, a computer for recording and processing information obtained during the observation. Besides that, it is necessary to select the optimal frequencies of the radio range, where there is no permanent presence of local stations, but there are powerful distant stations at distances convenient for meteor reflections. The choice of frequency depends on the geography and the location of the antenna and receiver. The radio station should be located at a distance of 500 – 2000 km from the receiver outside the zone of its direct hearing (up to 50 km).

The reception of the reflected signal of the radio station lasts from fractions to units of seconds, and the time profile of this musical–speech signal (MSS) is characterized by an instantaneous appearance and a smooth decline (signal attenuation). This makes it possible to separate meteor signals (MSS) from signals of a different nature that may appear on the air. Note that the number of MSS depends not only on meteor activity, but also on other factors. These include the number and time of operation of radio stations on this wave, the state of the ionosphere, factors of solar activity.

The instrument complex for recording meteors in the radio range, created at the SKU, includes a dipole antenna 12 meters long, oriented in the north–south direction, a USB FM tuner and a laptop (Fig. 6). In Figure 6, the number 1 indicates the monitor for displaying the status of the workstation. The HDTV program is visible on it, with the help of which the desired FM station is selected. The current waveform record is shown on the laptop screen in real time. Bursts of meteor reflections and interference are visible. Number 2 denotes a network drive that stores observational material in real time for further processing. Number 3 indicates the speakers that allow you to hear the signal from the FM tuner. FM receiver (indicated by number 4) is connected to a laptop that processes data using the standard HDTV program that comes with it. It also serves as a filter that removes most of the interference. The reception was tuned to the transmission frequency 89.8 MHz of the FM station located in Perm, at a distance of 1262 km from Petropavlovsk. To select a station, the program http://www.fmlist.org/ [23] was used, which displays information about all AM and FM transmitters in the world. The number 5 indicates a USB – oscilloscope connected to a laptop. It was used to record oscillograms using the Data Recorder module of the Multi VirAnalyser program.

Observations at the indicated frequency were carried out during the daytime and at night during the seasons of 2019 and 2020 and gave interesting results. A large number of events similar to meteor phenomena have been registered. The average number of such phenomena per day was about a hundred, with an average pulse duration of about 0.4 seconds. The most important was to obtain evidence that the recorded pulses are associated precisely with the reflection of radio waves from plasma meteor tracks.

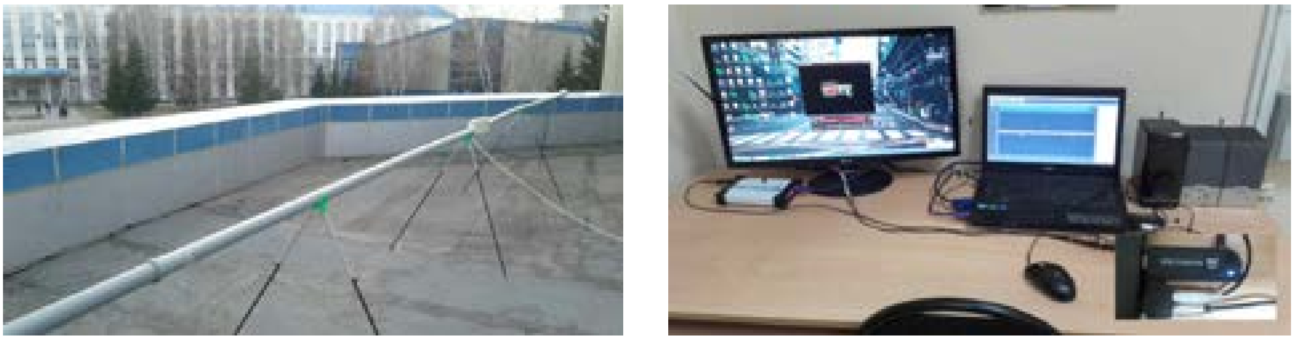

Figure 6 − Antenna (upper part) and an instrument complex for registering meteors in the radio range.

Results and discussion

In optical observations of meteors, it is quite easy to identify their images. In addition to them, only flying apparatuses are fast moving objects in the celestial sphere: satellites and airplanes. Both of them in the pictures are quite different from meteors, and they do not appear in the sky often.

When registering radio waves reflected from plasma meteor tracks, there are difficulties associated with various kinds of interference: natural and technogenic. Important criteria for difference are the temporal structure of the radio pulse and its duration. In this case, it should be taken into account that the parameters of the reflected pulse are determined by the concentration of free electrons per unit length of the plasma track. “Saturated tracks” with an electron density of more than $2 \cdot 10^{14}$ electrons per meter reflect radio waves most effectively (virtually mirror image). Such tracks are created by quite massive particles that generate meteors brighter than 5 magnitude. In this case, radio waves are reflected in much the same way as from a metal surface.

At lower concentrations of free electrons, they talk about “unsaturated” meteor tracks. In this case, it is more correct to talk not about reflection, but about the scattering of radio waves. In both cases, there is an increase in the intensity of the reflected signal, and after it reaches a maximum, a decrease. At the same time, the duration of the reflected pulse is noticeably longer for “saturated” tracks; it can be up to ten seconds. Here, the intensity of the reflected signal gradually increases at the beginning, while its maximum has the character of a plateau. For “unsaturated” meteor tracks, the duration of the reflected pulse does not exceed 1 second.

They are characterized by a very rapid increase in signal intensity, a sharp maximum and its rapid fall according to an exponential law. The relaxation time is 0.3 – 0.5 seconds. In both cases, the reflected radio pulses are characterized by a discontinuous structure (with a characteristic time of hundredths of a second), which is explained by the interference of radio waves reflected from different parts of the meteor track [21].

These signs made it possible to identify meteor radio echoes in the records and study the statistical daily and seasonal patterns of their appearance. Comparing the results obtained with the data of many other observers, it is possible to estimate the effectiveness of the newly created installation and the adequacy of the applied research methodology.

Important features of the daily course of meteor activity are the presence of a morning (about 06:00 local time) maximum and an evening (about 18:00 local time) minimum in the number of meteors. In this case, the time dispersion of the maximum and minimum positions is about 2 hours. It’s clear that sporadic meteors are considered in this case, since the presence of an active meteor shower at the moment can radically change the picture. It is especially important to take this into account for meteor showers with circumpolar radiants (Cassiopeids, Perseids, Draconids, and others). Figure 7 shows the daily distribution of meteor reflections on August 13, 2019, obtained at the CAR NKU.

This distribution compares well with the data of other observers shown in Figure 8.

The dynamics of the daily course of meteor phenomena recorded in the radio range throughout the month is shown in Figures 9 and 10. It is obvious that the month with an active meteor shower will be the most indicative for the study of the correct operation of the system. In this case, an excess of the daily number of meteors in the epoch of maximum will be detected. One of the best periods in this case should be considered August with its giant shower, the Perseids [25].

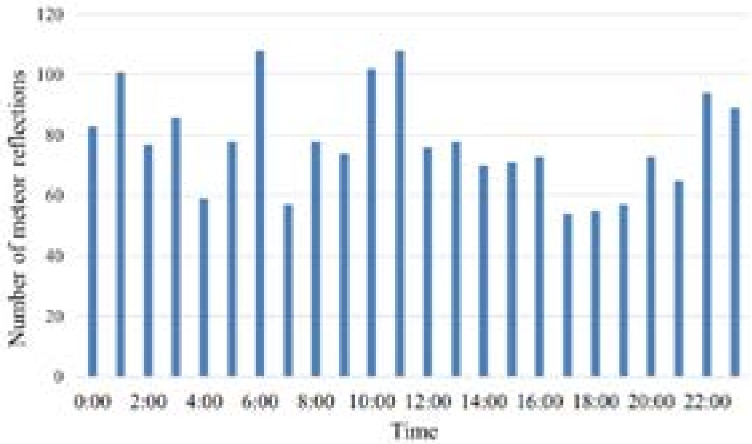

Figure 7 − The daily distribution of meteor reflections on August 13, 2019, CAR NKU, Petropavlovsk

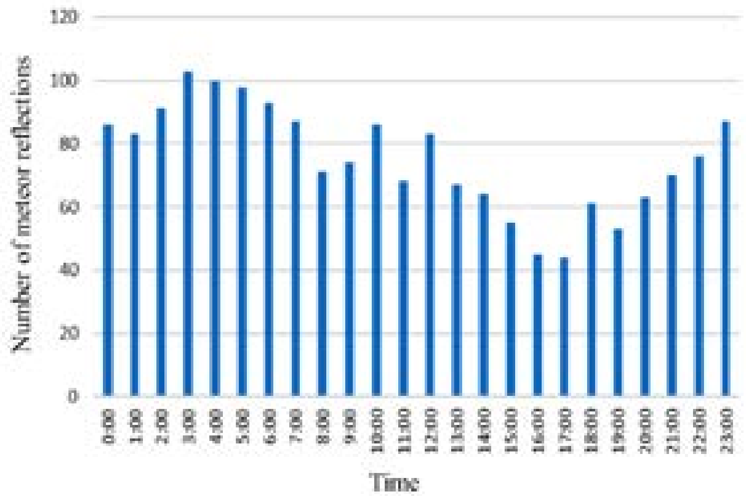

Figure 8 − Daily distribution of meteors for 13.08.2019, data from Mario Bombardini, Italy [24].

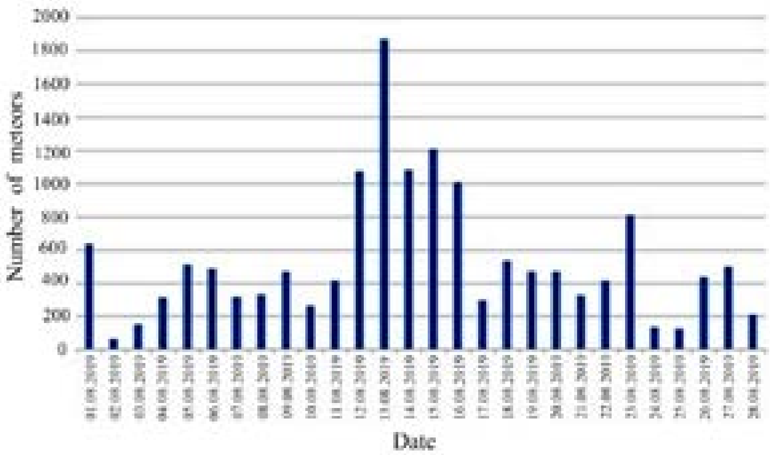

Figure 9 − Distribution of the daily number of meteors for August 2019 according to radio observations at the CAR NKU, Petropavlovsk.

Figure 9 clearly shows a wide maximum of Perseid activity from August 12 to 16 with a sharp peak on August 13. The relatively high meteor activity on August 1 can be associated with the combined action of the Cassiopeid and δ – Aquarid showers near this date, and the increase in meteor activity on August 23 with the simultaneous action of several weak meteor showers. Among them, the poorly studied ϰ–Cygnids meteor shower is best known [25].

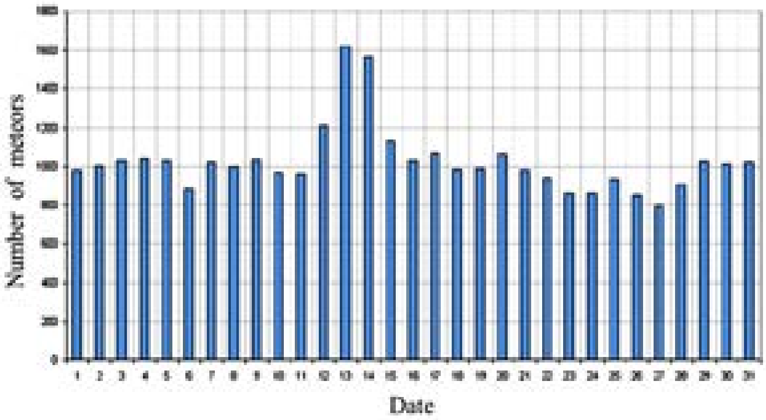

Figure 10 − Distribution of the daily number of meteors for August 2019 according to radio observations by F. Verbelen, Kampenhout (Belgium) at a frequency (49.99 MHz) [26].

Comparison of the radio observations results of the meteor phenomena frequency presented in Figures 9 and 10 shows their good mutual agreement. Thus, it can be argued about the achievement of a fairly confident registration of meteors by the radio echo method with the help of instruments available at CAR NKU.

Conclusions

We think that the combination of both optical and radio observations of meteor phenomena will be most effective in studying the features of the distribution of meteoroids in the vicinity of the Earth's orbit. At the same time, as noted, the methods of optical registration of meteors require their further development. And there are several possibilities here.

So the use of the new camera CANON 2000 D [27] could be an alternative to installing a meteor patrol. This camera in combination with a wide–angle lens CANON ZOOM LENS EF–S 10–22 mm has proven itself in the implementation of a panoramic view of the twilight segment in the summer. The field of view of a CANON 2000 D camera with a wide–angle lens is more than 90 degrees in azimuth. The camera has a higher sensitivity compared to previous models. With its help, an extensive set of high–quality images of noctilucent clouds in the 2021 season was obtained. In the same season, test observations of the Perseids were also carried out (Fig. 11), which made it possible to obtain high–quality images of meteors.

Figure 11 − Perseid meteors images taken with CANON 2000 camera with CANON ZOOM LENS EF–S 10–22 mm lens.

These results give good prospects for the implementation of new generation meteor patrols. In the future, it is planned to install three such cameras on a common tripod using a tracking module.

The use of an optical image brightness amplifier in the investigation of little–studied weak meteor showers is very promising. At the same time, observations of meteors of the ϰ–Cygnids shower are the most promising. In addition, with the use of this amplifier, it is planned to conduct experiments on the registration of meteors in the near infrared range. This is associated with the possibility of the registration of the meteors generated by extremely friable bodies, as well as icy meteoroids.

In addition, to register bright meteors and fireballs, a new All Sky camera ASI224VC with an Arecont 1.55 lens was purchased (Fig. 12 on the left). The camera is equipped with a protective acrylic dome and can work offline with recording information on a micro SD card. The field of view of this camera is 180 degrees [28].

Figure 12 − All Sky ASI224VC camera with Arecont 1.55 lens.

However, the highest expectations are associated with the new highly sensitive CANON RF camera [29], the use of which will make it possible to perform video recording of meteor phenomena with characteristics that are noticeably superior to their visual observations. Unlike previous models, this camera is distinguished by a very high light sensitivity, which makes it possible to register meteors up to 7–8 magnitudes. The use of this camera in conjunction with the tracking device Sky–Watcher Star Adventurer will greatly expand the possibilities of optical monitoring of meteor phenomena.

References

1. Babadzhanov P.B. (1987) Meteory i ih nabljudenie [Meteors and their observation] M.: Nauka.
2. Bronshtjen V.A. (1985) Fizika meteornyh javlenij [Meteors and their observation] M.: Nauka.
3. Bronshtjen V.A. (1987) Meteory, meteority, meteoridy [Meteors, meteorites, meteorids] M.: Nauka.
4. Rendtel J., Arlt R. Handbook for Meteor Observers. International Meteor Organization, Potsdam, 2015.
5. Southworth R.B. (1967) Spase density of radio meteors. Spec. Rept. Smithson. Astrophys. Obs. No. 239. P. 75–97.
6. Harris A. W., D'Abramo G. "The population of near–Earth asteroids". Icarus, 257, (2015): p. 302–312.
7. Voloshhuk Ju.I. (1989) Meteority i meteornoe veshhestvo [Meteorites and meteor matter] Kiev.
8. Ortiz J. L., Madiedo J. M., Morales N., Santos–Sanz P., and Aceituno F. J. (2015). "Lunar impact flashes from Geminids: analysis of luminous efficiencies and the flux of large meteoroids on Earth". Monthly Notices of the Royal Astronomical Society, 454, 344–352.

9. Korec M. (2015). “QHY (5L–II–M) CCD camera for video meteor observation”. In Rault J.–L. and Roggemans P., editors, Proceedings of the International Meteor Conference Mistelbach, Austria, 27–30 August 2015. IMO, pages 85–89.

10. Ott T., Drolshagen E., Koschny D., and Poppe B. (2016). “PaDe – The particle detection program”. In Roggemans A. and Roggemans P., editors, Proceedings of the International Meteor Conference, Egmond, the Netherlands, 2–5 June 2016. International Meteor Organization, pages 209–213.

11. Solodovnik A.A., Maugazina A.O. (Chehija) K voprosu ob jeffektivnosti primenenija cifrovyh prijomnikov izluchenija k registracii meteornyh javlenij [On the effectiveness of the use of digital radiation receivers for the registration of meteor phenomena] Materialy mezhdunarodnoj nauchno–prakticheskoj konferencii «Jeffektivnye instrumenty sovremennyh nauk 2016» Chehija, Praga, 22–30 aprelja 2016, Praha Publishing House «Education and Science» s.r.o. Chehija, p. 38 – 42.

12. Askarova M.M., Sartin S.A., Terehin N.S., Varkushina M.A. (2019) Primenenie imejushhegosja v centre Astrofizicheskih issledovanij oborudovanija dlja nabljudenija meteornyh potokov [Application of the equipment available at the Astrophysical Research Center for observing meteor showers] Vestnik SKGU im. M. Kozybaeva, g. Petropavlovsk, p. 78–82.

13. Harakteristiki zerkal’noj kamery Canon EOS 1000D. https://prophotos.ru/devices/canon–eos–1000d/spec (accessed on May 12, 2022).

14. Harakteristiki PZS – matricy SBIG 3200 ME astrokamera–sbig–stf–3200me–class–2 (accessed on May 12, 2022)

15. Bagrov A.V., Bolgova G.T., Leonov V.A. (2003) Televizionnyj monitoring meteornyh javlenij dlja izuchenija jevoljucii meteornyh potokov [Television monitoring of meteor events to study the evolution of meteor showers] Kinematika i fizika nebesnyh tel. №4. P. 265268.

16. Solodovnik A.A., Maugazina A.O. (2016) Opyt primenenija jelektronno–opticheskogo preobrazovatelja MPN – 8KM v astronomicheskih nabljudenijah [Experience in the use of the electron-optical converter MPN – 8KM in astronomical observations] Materialy mezhdunarodnoj nauchno–prakticheskoj konferencii «Jeffektivnye instrumenty sovremennyh nauk 2016» Chehija, Praga, 22–30 aprelja, Praha Publishing House «Education and Science» s.r.o – Chehija, p. 33 – 38.

17. Lovell B. (1958) Meteornaja astronomija [Meteor astronomy] M.: Fizmatgiz.

18. Lebedinec V.N., Korpuskov V.N., Sosnova A.K. (1971) Issledovanie meteornyh potokov radiolokacionnym metodom [Radar survey of meteor showers] Trudy IJeM – Obninsk: Izd–vo IJeM, № 24. p. 100 – 113.

19. Kashheev B.D., Lebedinec V.N. (1961) Radiolokacionnye issledovanija meteornyh javlenij [Radar surveys of meteor phenomena] M., 124 S.

20. Janches D., Swarnalingam N., Plane J. M. C., Nesvornэ D., Feng W., Vokrouhlickэ D., and Nicolls M. J. (2015). “Radar detectability studies of slow and small zodiacal dust cloud particles: II. A study of three radars with different sensitivity”. Astrophys. J., 807:1, 13.

21. Sartin S.A., Solodovnik A.A., Useinov B.M., Zhukeshov A.M., Amrenova A.U. (2020) Opyt registracii otrazhenija radiosignalov ot plazmennyh meteornyh trekov v observatorii SKGU [Experience in recording the reflection of radio signals from plasma meteor tracks at the NKZU Observatory] Scientific Journal al-Farabi Kazakh national university. Series Physical. SSN 1563-0315, eISSN 2663-2276, №1 (72). p. 49–57.

22. Kaiser T.R. (1955) The interpretation of radio echoes from meteor trails. Spec. Suppl. J. Atm. Terr. Phys, Vol. 2, P. 55–56.

23. FMLIST – database of worldwide FM radio, DAB and TV. https://www.fmlist.org/ul_login.php 05.05.2020. (accessed on May 12, 2022)

24. RMOB – radio meteor observing bulletin. https://www.rmob.org/index.php (accessed on May 12, 2022)

25. Kulikovskij P.G. (1971) Spravochnik ljubitelja astronomii [Astronomy Lover’s Handbook]. M.: Nauka.

26. Felix Verbelen. Radio meteors August 2019. https://www.meteornews.net/ (accessed on May 12, 2022)

27. Harakteristiki zerkal’noj kamery Canon EOS 2000D [Canon EOS 2000D SLR Camera Features] **canon.ru**›cameras/eos–2000d/specifications/ (accessed on May 12, 2022)

28. All Sky kamera harakteristiki [All Sky Performance Camera] https://astronomy–imaging–camera.com/product/asi224mc (accessed on May 12, 2022)

29. Harakteristiki bezzerkal’noj kamery Canon EOS RP [Canon EOS RP mirrorless camera specifications]. https://www.canon.ru/cameras/eos-rp/specifications/ (accessed on May 12, 2022)

Funded by Al-Farabi KazNU.

IRSTI 27.35.55; 27.31.21 https://doi.org/10.26577/ijmph.2022.v13.i2.05

A.B. Zhumageldina[1,2*], K.R. Yesmakhanova[1,2], Zh.Zh. Pashen[1]

[1]L.N. Gumilyov Eurasian National University, Astana, Kazakhstan,
[2]Ratbay Myrzakulov Eurasian International Centre for Theoretical Physics, Astana, Kazakhstan
*e-mail: ainurzhumageldina@gmail.com
(Received 27 April 2022; received in revised form 17 October 2022; accepted 9 November 2022)

Darboux transformation and exact solutions of nls-mb equations

Abstract. A nonlinear wave is one of the basic objects of physics. They are inherent to plasma physics and solid state physics, gravity and nuclear physics, field theory and optics, hydrodynamics and aerodynamics, kinetics of chemical reactions and population dynamics. It is well known that the constuction of explicit solutions for an integrable system plays a significant part in the definition and explanation of nonlinear phenomena. In this article, we will focus on integrable nonlinear Schrodinger and Maxwell-Bloch equations (NLS-MB) that represents the propagation of optical impulses in an inhomogeneous fibreglass with erbium-doped losses or amplification due to an external potential. Lax representation of NLS-MB will be given. Based on relevant Lax pair, Darboux transformation for NLS-MB will be obtained. Exact solutions will be derived through the Darboux transformation. Graphs of the obtained solutions will be constructed. By using our approach one can find also other differerent exact solutions of NLS-MB equations.
Keywords: NLS-MB equations, Lax pair, Darboux transformation, soliton, exact solutions.

Introduction

Nonlinear wave equations represent common and significant phenomena arising in different physical contexts, including plasma, acoustics, optics, and waves on water, and as a consequence they continue to attract considerable attention from researchers. Frequently nonlinear waves are mathematically defined by nonlinear partial differential equations. In certain physical modes, these PDEs are completely integrable and, as a consequence, have a remarkably deep mathematical structure. For instance, complete integrability is related to the existence of an endless number of conservation laws; the existence of a Lax pair makes it possible to develop and use different analytical tools. The behavior of solutions of integrable nonlinear equations shows a lot of interesting phenomena. These PDEs admit multiple types of exact solutions, including bound states, and solutions of finite kind and solitons. Furthermore, these equations are interesting not only from a mathematical viewpoint, but also significant from a practical point of view, since they determinate equations for many particular physical conditions.

Over the past few years, long-range optical fiber communication has attracted great interest from scientists around the world. The transmission of soliton pulses in ultrafast communication systems plays an especially important role and is considered the tool of the future to achieve low loss, efficiency and high speed communication. Many equations have been studied by mathematicians and physicists as models for fiber optic communication.To take into account the influence of large pulse widths, the dynamics of the system is controlled by the coupled system of the nonlinear Schrodinger equation and Maxwell-Bloch equation (NLS-MB) [1]. The nonlinear Schrödinger equation (NSE) describes the propagation of optical pulses through nonlinear optical fibers in the picosecond range [2]. For soliton-based communication systems, fiber attenuation must be compensated for to be more competitive, reliable, and cost-effective than traditional systems. Maxwell-Block (MB) equations describe a type of pulse propagation called self-induced transparency (SIT) [3]. This type of pulse reaches a steady state, where the width, energy and shape of the pulse remain unchanged after several classical absorption lengths, and the pulse velocity is much lower than the speed of light in this medium. Together they are known as the NLS-MB equations.

In this article we will construct the Darboux transform of the Lax pair of the NLS-MB equation, new exact solutions will be directly constructed starting from the seed solution. Because obtaining of exact solutions to the integrable equations is one of the most essential and meaningful topics.

Materials and Methods

There are some methods for constructing solutions, such as the inverse scattering transformation method [4], the Hirota bilinear transformation method [5], The Backlund [6] and Darboux transformation (DT) methods [7-11], the Fokas approach [12], the long-time asymptotic approach [13], and so on. Among them, the Darboux transformation is the most effective method for finding explicit solutions to integrable equations. The unique advantage of DT in solving integrable equations is that their solutions are constructed using a purely algebraic procedure.

This article consists of three main sections. In the first section Lax representation of the integrable NLS-MB equations will be introduced. Then we will give the detailed proof of the Darboux transformation for NLS-MB equations in section 2. In section 3 we will derive new and different kind of solutions based on obtained Darboux transformation and construct their graphs. Last section devoted to conclusion.

Literature review

For the first time Maimistov and Manykin [4] derived the coupled NLS-MB system to consider the propagation of ultrashort pulses in a light guide with a two-level resonant medium with Kerr nonlinearity. Many scientists have worked on this, achieving significant results [5,6]. These equations has also been reduced using the Painleve analysis [7]. In addition, the Lax pair and the multisoliton solution of the NLS-MB equations were proposed by Kakei and Satsuma [8]. There has been a lot of research done on the NLS-MB equations recently. The multisoliton solution is given in reference [9]. Single soliton and single respiratory solutions of the NLS-MB equations were obtained using the Darboux transformation (DT) [10-12].

The Darboux transform (DT) of an integrable system was first proposed by Matveev and Salle [6] . The main idea is that they construct a DT for a linear system and an adjoint system. They then join the two DTs together and find the double DT (i.e. BDT). Moreover, the BDT of some integrable equations was constructed in [14, 15]. Numerous successful implementations of Darboux transformation in various fields of physics and applied mathematics ensure its importance from an applied point of view [17, 18]. It is proved that this method, based on lax pairs, is one of the most productive algorithmic procedures for obtaining explicit solutions to nonlinear evolution equations. An effective way to create obvious solutions for many integrated systems is Darboux Transformation (DT) [6-10].

1. Lax representation of the integrable NLS-MB

If an optical pulse propagates through a nonlinear waveguide, the evolution of the pulse is determined by the NLS-MB equations. The NLS-MB equations are written as [1, 4].

$$q_t = i[\tfrac{1}{2}q_{xx} + |q|^2 q] + 2p, \tag{1}$$

$$p_x = 2i\omega_0 p + 2q\eta, \tag{2}$$

$$\eta_x = -(qp^* + q^* p). \tag{3}$$

where:

q – the complex field envelope;

p – measure of polarization of the resonant medium;

η – inverse population between two levels of wave functions of two energy levels of resonant atoms;

ω – the real constant parameter, it corresponds to the frequency;

$*$ – is the complex conjugate.

NLS-MB equations' linear eigenvalue problem is expressed as

$$\Psi_x = U\Psi \tag{4}$$

$$\Psi_t = V\Psi \tag{5}$$

where

$$\Psi = \begin{pmatrix}\Psi_1\\ \Psi_2\end{pmatrix} \tag{6}$$

$$U = \begin{bmatrix} \lambda & q \\ -q^* & -\lambda \end{bmatrix} \equiv \lambda\sigma_3 + U_0, \tag{7}$$

$$\begin{aligned} V = \ & i\left(\begin{bmatrix} 1 & 0 \\ 0 & -1 \end{bmatrix}\lambda^2 + \begin{bmatrix} 0 & q \\ -q^* & 0 \end{bmatrix}\lambda + \frac{1}{2}\begin{bmatrix} |q|^2 & q_x \\ q_x^* & -|q|^2 \end{bmatrix}\right) + \\ & + \frac{1}{\lambda - i\omega_0}\begin{bmatrix} \eta & -p \\ -p^* & -\eta \end{bmatrix} \equiv i\sigma_3\lambda^2 + i\lambda V_1 + \frac{i}{2}V_0 + \frac{1}{\lambda - i\omega_0}V_{-1} \end{aligned} \tag{8}$$

here

λ – the complex eigenvalue parameter constant;

U and V – the Lax pair of NLS-MB equations.

2. Darboux transformation for the NLS-MB equations.

In this section Darboux transformation will be introduced for the integrable NLS-MB equations. Firstly, to construct Darboux transformation of NLS-MB equation, we consider the transformation about linear function Ψ.

$$\Psi' = T\Psi = (\lambda I - S)\Psi \tag{9}$$

therefore

$$\Psi'_x = U'\Psi' \tag{10}$$

$$\Psi'_t = V'\Psi' \tag{11}$$

where $S = \begin{pmatrix} s_{11} & s_{12} \\ s_{21} & s_{22} \end{pmatrix}$ and $I = \begin{pmatrix} 1 & 0 \\ 0 & 1 \end{pmatrix}$. U' and V' depend on q', p', η', λ and it dependence is the same as the dependence of p, p, η, λ on U and V. To hold equations (10) and (11) , T must satisfy

$$T_x + TU = U'T \tag{12}$$

$$T_t + TV = V'T \tag{13}$$

The relation between q, p, η and new solutions q', p', η' which is called Darboux transformation can be got by using equations (12) and (13). From equation (12) we have

$$\begin{aligned} & -S_x + \lambda^2 I\sigma_3 + \lambda I U_0 - \lambda S\sigma_3 - SU_0 - \\ & -\lambda^2\sigma_3 I + \lambda\sigma_3 S - \lambda U'_0 I + U'_0 S = 0 \end{aligned} \tag{14}$$

Collecting different degrees of λ, we get the following set of identities

$$\lambda\colon IU_0 - S\sigma_3 + \sigma_3 S - U'_0 I = 0 \tag{15}$$

which further leads to

$$U'_0 = U_0 + [\sigma_3, S], \tag{16}$$

$$\begin{aligned} \lambda^0\colon S_x = \sigma_3 S^2 + \begin{pmatrix} 0 & q \\ -q^* & 0 \end{pmatrix} S - \\ -S\sigma_3 S - S\begin{pmatrix} 0 & q \\ -q^* & 0 \end{pmatrix}, \end{aligned} \tag{17}$$

from above several identities, we can get

$$q' = q + 2s_{21}, \tag{18}$$

$$q^{*\prime} = q^* + 2s_{21}, \tag{19}$$

and S should have a condition $s_{12} = s_{21}^*$. By (13), following identity can be obtained

$$\begin{aligned} & -S_t + i\lambda^3 I\sigma_3 + i\lambda^2 IV_1 + \frac{i}{2}\lambda IV_0 + \frac{\lambda}{\lambda - i\omega_0}IV_{-1} - iS\sigma_3\lambda^2 - i\lambda SV_1 - \frac{i}{2}SV_0 - \\ & -\frac{1}{\lambda - i\omega_0}SV_{-1} - i\lambda^3\sigma_3 I + i\lambda_2\sigma_3 S - i\lambda_2 V'_1 I + \\ & + i\lambda V'_1 S - \frac{i}{2}\lambda V'_0 I + \frac{i}{2}V'_0 S - \frac{\lambda}{\lambda - i\omega_0}V'_{-1}I + \frac{1}{\lambda - i\omega_0}V'_{-1}S = 0 \end{aligned} \tag{20}$$

Comparing the coefficient of λ^i $(i = 0,1,2)$ of the two sides of equation (20) as we did before with equation (14), we have

$$\lambda^2\colon IV_1 - iS\sigma_3 + i\sigma_3 S - iV'_1 I = 0 \tag{21}$$

which leads to

$$V'_1 = V_1 + [\sigma_3, S], \tag{22}$$

$$\lambda: \frac{i}{2} IV_0 - ISV_1 + IV'_1 S - \frac{i}{2} V'_0 I = 0 \qquad (23)$$

$$\lambda^0: S_t = V_{-1} - V'_{-1} + \frac{i}{2} V'_0 S - \frac{i}{2} S V_0, \qquad (24)$$

$$\frac{1}{\lambda - i\omega_0}: i\omega_0 IV_{-1} - SV_{-1} - SV_{-1} - \\ - i\omega_0 V'_{-1} I + V'_{-1} S = 0 \qquad (25)$$

further it leads to

$$V'_{-1} = (S - i\omega_0 I) V_{-1} (S - i\omega_0 I)^{-1} \qquad (26)$$

Thus, from the above identities, after simplifications, several important equations (16-19), (21-26) were obtained that lead to Darboux transformations for the NLS-MB system later.

Now in order to determine the values of p', $p^{*\prime}$ and η' we put into Eq. (26) values of S, V_{-1}, V'_{-1} and get

$$p' = \frac{2\eta(s_{11} - i\omega_0) s_{12} - p^* s_{12}^2 + p(s_{11} - i\omega_0)^2}{\triangle} \qquad (27)$$

$$p^{*\prime} = \frac{-2\eta(s_{22} - i\omega_0) s_{21} + p^*(s_{11} - i\omega_0)^2 - p s_{21}^2}{\triangle} \qquad (28)$$

$$\eta' = \frac{\eta[(s_{11} - i\omega_0)(s_{22} - i\omega_0) + s_{12} s_{21}] - p^* s_{12}(s_{22} - i\omega_0) + p(s_{11} - i\omega_0) s_{21}}{\triangle} \qquad (29)$$

where

$$\triangle = (s_{11} - i\omega_0)(s_{22} - i\omega_0) - s_{12} s_{21}.$$

The main step is to find the exact value of S expressed by solving the column of equations (4) and (5). Suppose, that

$$S = H \begin{pmatrix} \lambda_1 & 0 \\ 0 & \lambda_2 \end{pmatrix} H^{-1} \equiv H \Lambda H^{-1} \qquad (30)$$

$$H = \begin{pmatrix} \Psi_1(\lambda_1, x, t) & \Psi_1(\lambda_2, x, t) \\ \Psi_2(\lambda_1, x, t) & \Psi_2(\lambda_2, x, t) \end{pmatrix}, \qquad (31)$$

where λ_1 and λ_1 are complex constants, $\det \mathrm{H} \neq 0$. From equations (4) and (37) we have

$$H_x = \sigma_3 H \Lambda + \begin{pmatrix} 0 & q \\ -q^* & 0 \end{pmatrix} H \qquad (32)$$

At the same time, from equations (5) and (31) can be derived:

$$H_t = \sigma_3 H \Lambda^2 + i V_1 H \Lambda + \frac{i}{2} V_0 H + \\ + V_{-1} H \begin{pmatrix} \frac{1}{\lambda_1 - i\omega_0} & 0 \\ 0 & \frac{1}{\lambda_1 - i\omega_0} \end{pmatrix} \qquad (33)$$

Then we can verify by direct calculation that S defined by equation (30) actually satisfies equations (18) (24). To satisfy the S' and V'_{-1} constraints as above, we obtain

$$\lambda_2 = -\lambda_1^* \qquad (34)$$

$$H = \begin{pmatrix} \Psi_1(\lambda_1, x, t) & -\Psi_2^*(\lambda_1, x, t) \\ \Psi_2(\lambda_1, x, t) & \Psi_1^*(\lambda_1, x, t) \end{pmatrix} \qquad (35)$$

Thus, we replacing equations (35) and (30) again to equations (18) and (26) and obtain the following Darboux transformations for NLS-MB.

$$q' = q + 2 \frac{(\lambda_1 + \lambda_1^*) \Psi_1 \Psi_2^*}{\triangle} \qquad (36)$$

$$\begin{aligned} p' &= -\frac{2\eta}{\triangle^2} \left[|\Psi_1|^2 \left(1 - \frac{\tilde{\ }_1}{\tilde{\ }_2} \right) - |\Psi_2|^2 \left(1 - \frac{\tilde{\ }_2}{\tilde{\ }_1} \right) \right] \Psi_1 \Psi_2^* + \\ &+ \frac{p^*}{\triangle^2} \left[2 - \frac{\tilde{\ }_1}{\tilde{\ }_2} - \frac{\tilde{\ }_2}{\tilde{\ }_1} \right] \Psi_1^2 \Psi_2^{*2} + \frac{p}{\triangle^2} \left[|\Psi_1|^4 \frac{\tilde{\ }_1}{\tilde{\ }_2} - 2|\Psi_1|^2 |\Psi_2|^2 + |\Psi_2|^4 \frac{\tilde{\ }_2}{\tilde{\ }_1} \right] \end{aligned} \qquad (37)$$

$$\begin{aligned} \eta' &= -\frac{p^*}{\triangle^2} \left[|\Psi_1|^2 \left(1 - \frac{\tilde{\ }_2}{\tilde{\ }_1} \right) - |\Psi_2|^2 \left(1 - \frac{\tilde{\ }_1}{\tilde{\ }_2} \right) \right] \Psi_1 \Psi_2^* + \\ &+ \frac{p}{\triangle^2} \left[|\psi_1|^2 \left(1 - \frac{\tilde{\ }_1}{\tilde{\ }_2} \right) - |\Psi_2|^2 \left(1 - \frac{\tilde{\ }_2}{\tilde{\ }_1} \right) \right] \Psi_2 \Psi_1^* + \\ &+ \frac{\eta}{\triangle^2} \left[|\Psi_1|^4 + |\Psi_2|^4 + 2 \left(\frac{\tilde{\ }_2}{\tilde{\ }_1} + \frac{\tilde{\ }_1}{\tilde{\ }_2} - 1 \right) |\Psi_1|^2 |\Psi_2|^2 \right] \end{aligned} \qquad (38)$$

Here $\Psi_i \equiv \Psi_i(\lambda_1, x, t)$, $\tilde{\lambda}_i \equiv \lambda_i - i\omega_0$, $i = 1,2$ and $\triangle = |\Psi_1|^2 + |\Psi_2|^2$.

3. Exact solutions of the NLS-MB equations

In this section our aim is to derive new and different solutions of NLS-MB using obtained DT. Firstly, in order to costruct one-soliton solution we assume seed solutions as $q = 0, p = 0, \eta = 1$, then we take eigenfunctions in the following form:

$$\Psi_1 = \mathrm{e}^{\lambda_1 x + \left(\mathrm{i}\lambda_1{}^2 + \frac{1}{\lambda_1 + \omega_0}\right)\mathrm{t} + \delta_1}, \tag{44}$$

$$\Psi_2 = \mathrm{e}^{-\lambda_1 x - \left(\mathrm{i}\lambda_1{}^2 + \frac{1}{\lambda_1 - \omega_0}\right)\mathrm{t} + \delta_1} \tag{45}$$

where

δ_1 – arbitrary fixed real constant and $\lambda_1 = \mathrm{a} + \mathrm{ib}$. Substituting these two eigenfunctions into the the following Darboux transformations given in (36-38) and choosing $a = 0.5$, $b = 0.5$ $\omega_0 = 1.5$, $\delta_1 = 1$ then one-solitone solution of NLS-MB can be obtained, the evolution of which is shown in the figure. 1 clearly shows that q, p, and η are bright solitons, because their waves under the flat non-vanishing plane.

$$q' = \frac{(2.0+0.0\, i)\mathrm{e}^{-\vartheta+\varphi+1}\mathrm{e}^{\tau-\omega+1}}{\mathrm{e}^{-\tau+\omega+1.0}\mathrm{e}^{-\vartheta+\varphi+1}+\mathrm{e}^{\vartheta-\varphi+1}\mathrm{e}^{\tau-\omega+1}}; \tag{46}$$

$$\begin{aligned} p' &= [(1.600000000 + 0.0\, i)\mathrm{e}^{\tau-\omega+1}\mathrm{e}^{-\vartheta+\varphi+1}\mathrm{e}^{\tau-\omega+1} - (0.5 - 1.0\, i) \times \\ &\times \mathrm{e}^{-\tau+\omega+1}\mathrm{e}^{-\vartheta+\varphi+1})]/[\mathrm{e}^{-\tau+\omega+1.0}\mathrm{e}^{-\vartheta+\varphi+1} + \mathrm{e}^{\vartheta-\varphi+1}\mathrm{e}^{\tau-\omega+1}]^2 \end{aligned} \tag{47}$$

$$\begin{aligned} \eta' = \; & [(-0.2000000000 - 0.6000000000\, i)\mathrm{e}^{-\vartheta+\varphi+1.0}\mathrm{e}^{-\tau+\omega+1.0} - \\ & -(0.6000000000 + 0.2000000000\, i)\mathrm{e}^{\tau-\omega+1.0}\mathrm{e}^{\vartheta-\varphi+1.0}\left(\mathrm{e}^{-\vartheta+\varphi+1.0}\right)^{\mathrm{e}^{-\tau+\omega+1.0}} + \\ & +(1.200000000 + 0.6000000000\, i)\left(\mathrm{e}^{-\vartheta+\varphi+1.0}\right)^2(\mathrm{e}^{-\tau+\omega+1.0})^2 \times \\ & \times (1.0 + 0.2000000000\, i)\mathrm{e}^{\tau-\omega+1.0}\mathrm{e}^{\vartheta-\varphi+1.0}\mathrm{e}^{-\vartheta+\varphi+1.0}\mathrm{e}^{-\vartheta+\varphi+1.0} + \\ & +1.0\left(\mathrm{e}^{\vartheta-\varphi+1.0}\right)^2(\mathrm{e}^{\tau-\omega+1.0})^2)]/(\mathrm{e}^{-\vartheta+\varphi+1.0}\mathrm{e}^{-\tau+\omega+1.0}+\mathrm{e}^{\tau-\omega+1.0}\mathrm{e}^{\vartheta-\varphi+1.0})^2 \end{aligned} \tag{48}$$

here

$$\tau = (0.0294117647 - 0.1176470588\, i)t$$
$$\vartheta = (0.0294117647 + 0.1176470588\, i)t$$

and

$$\omega = (0.5 - 0.5\, i)x$$
$$\varphi = (0.5 + 0.5\, i)x$$

Graphs of one-soliton solutions of the NLS-MB equations are shown in Figure 1:

($|q|^2$) ($|p|^2$) ($|\eta|^2$)

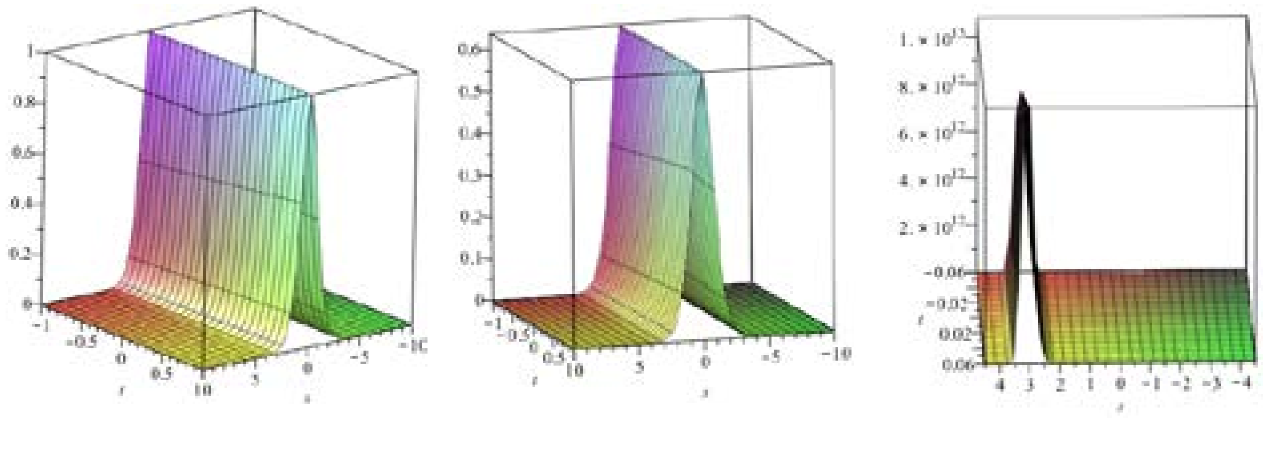

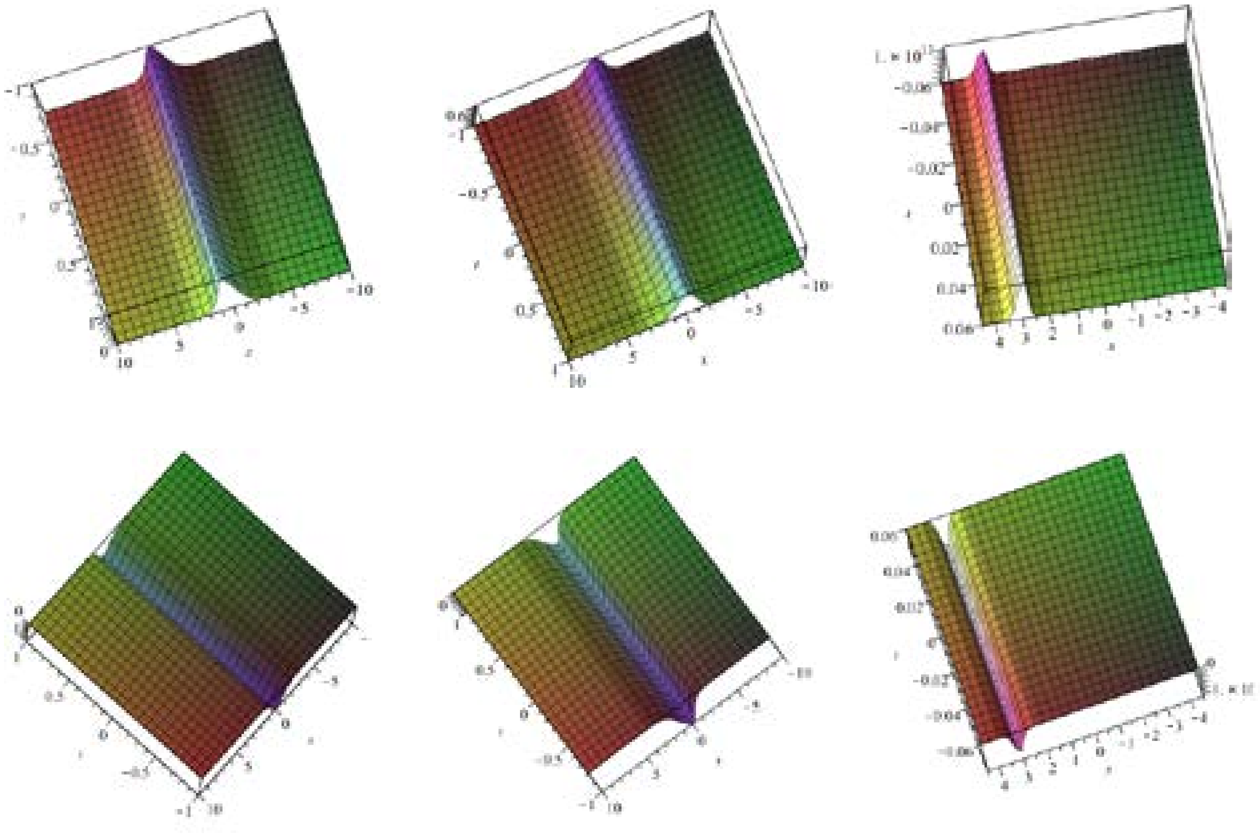

Figure 1 – One-soliton solutions of the NLS-MB equations

We obtained another type of solution for the NLS-MB equations by taking the seed solutions as $= 0, p = 0, \eta = 1$.

$$\Psi_1 = x + \mathrm{it} + 1, \tag{49}$$

$$\Psi_2 = -x - \mathrm{it} \tag{50}$$

Substituting the eigenfunctions Ψ_1 and Ψ_2 from (48)-(49) and the eigenvalues $\lambda_1 = \mathrm{a} + \mathrm{ib}$ and $a = 0.5$, $b = 0.5$, $\omega_0 = 1.5$ into the Darboux transformation (36)-(38), we obtain exact solutions for the system of equations (1)-(3) in the following form:

$$q' = -2.0\ \frac{(x+it+1)(-x+it)}{-2\,t^2-2\,x^2-2\,x-1}; \tag{51}$$

$$p' = -1.600000000\ \frac{(-x+it)(x+it+1)\left(0.5-1.0\,i-2.0\,it^2-2.0\,ix^2+1.0\,x-2.0\,ix\right)}{(-2\,t^2-2\,x^2-2\,x-1)^2}; \tag{52}$$

$$\begin{aligned} \eta' = \ & (-0.8000000000 + 0.0\,i)\times \\ & \times\left[\left(\frac{(0.5+0.5\,i)(x+it+1)(x-it+1)-(0.5-0.5\,i)(-x-it)(-x+it)}{(x+it+1)(x-it+1)+(-x-it)(-x+it)} - 1.5\,i\right)\times\right. \\ & \times\left(\frac{(0.5+0.5\,i)(-x-it)(-x+it)-(0.5-0.5\,i)(x+it+1)^{x-it+1}}{(x+it+1)(x-it+1)+(-x-it)(-x+it)} - 1.5\,i\right)+ \\ & \left.+\frac{(1.0+0.0\,i)(x+it+1)(-x+it)(x-it+1)(-x-it)}{\left((x+it+1)(x-it+1)+(-x-it)(-x+it)\right)^2}\right] \end{aligned} \tag{53}$$

Graphs of solutions of the NLS-MB equations are shown in Figure 2:

$(|q|^2)$ $(|p|^2)$ $(|\eta|^2)$

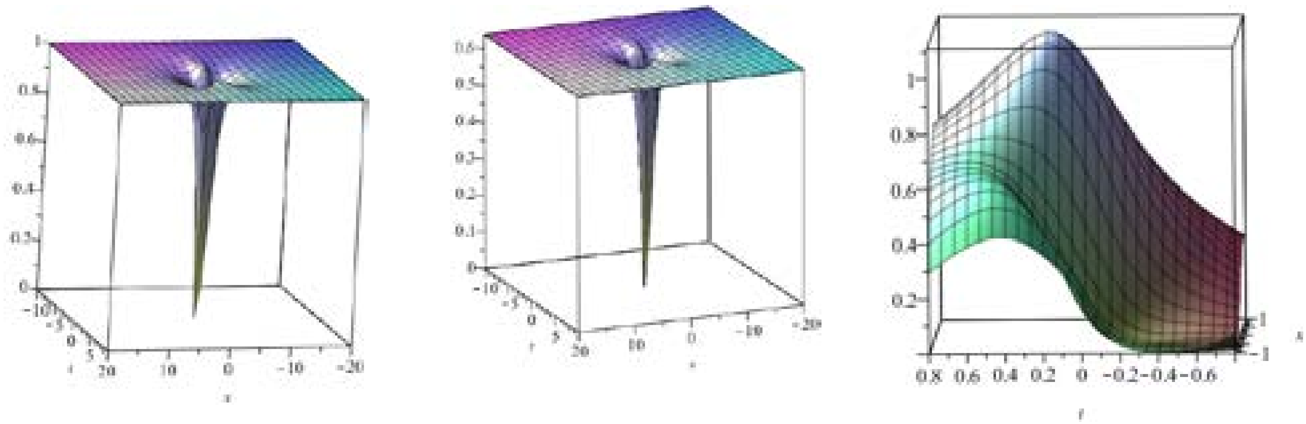

Figure 2 – Exact solutions of the NLS-MB equations

Conclusion

In this article, we studied the nonlinear Schrodinger and Maxwell-Bloch equations (NLS-MB) which describe the propagation of optical solitons in optical fibers with resonant impurities and nonlinear systems doped with erbium.

In the first section we presented a Lax pair formulation for NLS-MB equations. The Lax pair plays an significant role in the research of integrable properties of the NLS equation. The Darboux transformation was constructed and seed solutions were obtained in the second section. The Darboux transformation is the most effective technique of searching for exact solutions of integrable equations. To find Darboux transformation of NLS-MB equation, we considered the transformation about linear function. In the third section on the basis of Darboux transformation, different exact solutions of NLS-MB equations were obtained. Firstly, to construct a one-soliton solution, we took seed solutions as $\boldsymbol{q=0, p=0, \eta=1}$. We chose the appropriate parameter values and built graphs from which you can see the behavior of the solution. Namely, it can be seen from the graph 1 that obtained results corresponded to bright solitons, because their waves under the flat non-vanishing plane. Then in the same section we have obtained other exact solutions. The graphs of these solutions were also presented.

Using our approach a new type of waves can be derived for another integrable coupled system in optics. The nonlinear phenomena studied in this work may be useful in physics, mathematics and other disciplines.

Acknowledgments

The research work is funded by the Science Committee of the Ministry of Education and Science of the Republic of Kazakhstan (grant No AP08856912).

References

1. Maimistov, A.I., Manykin, E.A. “Propagation of ultrashort optical pulses in resonant non-linear light guides.” *Zh. Eksp.Teor. Fiz.* 85, (1983): 1177–1181.

2. Hasegawa, A., Tappert, F. “Transmission of stationary nonlinear optical pulses in dispersive dielectric fibers. I. Anomalous dispersion.” *Appl. Phys. Lett.* 23, (1973): 142–144.

3. McCall, S.L., Hahn, E.L.: “Self induced transparency by pulsed coherent light.” *Phys. Rev. Lett.* 18, (1967): 908–911.

4. Neugebauer, G., Meinel, R. "General N-soliton solution of the AKNS class on arbitrary background." *Phys. Lett. A.* 100, (1984): 467–470.

Kakei, S., Satsuma, J. "Multi-soliton solutions of a coupled system of the nonlinear Schrödinger equation and the Maxwell–Bloch equations." *J. Phys. Soc. Jpn*. 63, (1994): 885-894.

5. Neugebauer, G., Meinel, R. "General N-soliton solution of the AKNS class on arbitrary background." *Phys. Lett. A* 100, (1984): 467–470.

6. He, J.S., Cheng, Y., Li, Y.S. "The Darboux transformation for the NLS-MB equations." *Commun. Theor. Phys.* 38, (2002): 493– 496.

7. Yesmakhanova, K., Nugmanova, G., Shaikhova, G., Myrzakulov, R., Bekova, G. "Coupled dispersionless and generalized Heisenberg ferromagnet equations with self-consistent sources: Geometry and equivalence." *International Journal of Geometric Methods in Modern Physics.* 17(7), (2020): 2050104-2050104.

8. Bekova, G., Shaikhova, G., Yesmakhanova, K., Myrzakulov, R. "Darboux transformation and soliton solution for generalized Konno-Oono equation" *Journal of Physics: Conference Series.* 1416, (2019): 012003.

9. Kutum, B.B., Yesmakhanova, K.R., Shaikhova, G.N. "The differential-q-difference 2D Toda equation: bilinear form and soliton solutions" *Journal of Physics: Conference Series; Bristol.* 1391 (2019): 1742-6596.

10. Bekova, G.T., Shaikhova, G.N., Yesmakhanova, K.R., Myrzakulov, R. "Conservation laws for two dimensional nonlinear Schrödinger equation" *AIP Conference Proceedings.* (2019): 030003.

11. Yesmakanova K R, Shaikhova G.N, Bekova G.T, Myrzakulova Zh.R. "Determinant Representation of Darboux transformation for the (2+1)-Dimensional Schrodinger-Maxwell-Bloch Equation." *Advances in Intelligent Systems and Computing.* 441 (2016): 183-198.

12. Li, X.Y., Zhao, Q.L. "A new integrable symplectic map by the binary nonlinearization to the super AKNS system." *J. Geom. Phys*. 121, 2017: 123–137.

13. Zhang, N., Xia, T.C., Hu, B.B. "A Riemann–Hilbert approach to complex Sharma–Olver equation on half line." *Commun. Theor. Phys*. 68, (2017): 580–594.

14. Wang, D.S., Wang, X.L. "Long-time asymptotics and the bright N-soliton solutions of the Kundu–Eckhaus equation via the Riemann–Hilbert approach. Nonlinear Anal." *Real World Appl.* 41, (2018): 334–361.

15. Maimistov, A.I., Basharov, A.M. *Nonlinear Optical Waves.* Berlin: Springer, 1999.

16. Hasegawa, A ., *Optical Solitons in Fibers* Berlin: Springer, 1989.

17. Agrawal, G. P, *Nonlinear fiber optics* New York: Academic Press, 1989.

18. Porsezian, K., Mahalingam, A., Shanmugha Sundaram, P., *Chaos, Solitons and Fractals.* 11, (2000): 12-61.

IRSTI 29.15.03 https://doi.org/10.26577/ijmph.2022.v13.i2.06

A. Muratkhan[1], A. Orazymbet[1], M. Zhakipova[1],
M. Assylbek[2], S. Toktarbay[1,2*]

[1]Al-Farabi Kazakh National University, Almaty, Kazakhstan
[2]Kazakh National Women's Teacher Training University, Almaty, Kazakhstan
*e-mail: saken.yan@yandex.ru
(Received 8 September 2022; accepted 14 December 2022)

A shadows from the static black hole mimickers

Abstract. In this work, we study shadows from the naked singularity spacetime. The most analytical solutions of black hole shadows only investigated the case that the geodesic equations for photons can separate variables. We review the spherical null naked singularity metric and this spherically symmetric naked singularity spacetime metric is the solution of Einstein equations with an anisotropic fluid source which has no photon sphere. We also review a static, axially-symmetric singular solution of the vacuum Einstein's equations without an event horizon which is can be used to describe the exterior gravitational field of a mass distribution with quadrupole moment. Moreover, the corresponding spacetime is characterized by the presence of naked singularities. It is theoretically known that not only a black hole can cast shadow, but other compact objects such as naked singularities, gravastar or boson stars can also cast shadows. We present the analytical calculation of shadows for both naked singularities spacetime and compare with the shadow of Schwarzschild static black hole, we show that this can serve as a black hole mimicker.
Keywords: compact object, naked singularity, shadow.

Introduction

By the Event Horizon Telescope (EHT) collaboration have unveiled the first image of the supermassive black hole shadow at the centre of our own Milky Way galaxy [1]. The Event Horizon Telescope (EHT) has mapped the first image of a black hole at the centre of the more distant Messier 87 galaxy in 2019 [2]. However, the images of two black holes similar, even they from the two completely different types of galaxies and two very different black hole masses. These results allows us to tests and verify of gravity theories and corresponding black hole solutions near a regime of the gravitational field for which the validity of General Relativity (GR). Therefore, it is important to consider any theory or calculation that satisfies the observational results in order to understand the nature of the geometry in the vicinity of an astrophysical black hole candidate and to test the validity of black hole hypotheses.

Black hole mimickers are possible alternatives for black holes, they would look observationally almost like black holes but would have no horizon. The properties in the near-horizon region where gravity is strong can be quite different for both type of objects, but at infinity it could be difficult to discern black holes from their mimickers.

In [3] it was provide a review of the current state of the research of the black hole (BH) shadow, focusing on analytical studies (see [4–7]. A black hole captures all light falling onto it and it is not possible to obtain a direct image of them, an observer will see a dark spot in the sky where the BH is supposed to be located. Due to the strong bending of light rays by the Black Hole gravity, both the size and the shape of this spot are different from what we naively expect on the basis of Euclidean geometry from looking at a non-gravitating black ball. Also, the authors [3] tried to give a complete list that have historically been used to refer to the visual appearance of a black hole and related concepts and they noted that despite the different names and different physical formulation of the problem, all these concepts are strongly intertwined. The word 'shadow' in different languages has several meanings. In the case of the BH shadow, it can be understood as a dark silhouette of the BH against a bright background which, however, is strongly influenced by the gravitational bending of light.

In [8], the authors construct a space-time configuration that has a central naked singularity, but without photon sphere, and it can give both a shadow and a negative perihelion precession. Their results imply that if the presence of a shadow and positive perihelion 2 precession implies either a black hole or a naked singularity, the presence of a shadow and negative perihelion precession simultaneously would only imply a naked singularity.

This work is organized as follows. In Sec.II we review the metric of null naked singularity spacetime which is the solution of Einstein's field equations with an anisotropic fluid source, we calculate the shadows from this spacetime in section III and using the same procedure, in section IV we investigate the shadows in the axisymmetric spacetime. Finally, Sec. V contains a summary of our results.

Spherical symmetric null naked singularity

There has been a significant amount of work regarding the singular spacetimes and a lot of literature where timelike, lightlike geodesics around the black hole and naked singularity are investigated. Generally, shadow is considered to be formed due to the existence of a photon sphere outside the event horizon of a black hole.

The line element representation for null naked singularity given by [9],

$$ds^2 = \frac{dt^2}{\left(1+\frac{M}{r}\right)^2} + \left(1+\frac{M}{r}\right)^2 dr^2 + +r^2(d\theta^2 + sin^2\,\theta\, d\phi^2), \tag{1}$$

where M is the Arnowitt-Deser-Misner (ADM) mass of the above spacetime. The expression

of the Kretschmann scalar and Ricci scalar for this spacetime are:

$$R_{\alpha\beta\gamma\delta}R^{\alpha\beta\gamma\delta} = \frac{4M^2((M-2r)^2 r^4 + 4(M+r)^2 r^4 + (M+r)^4 (M+2r)^2)}{r^4 (M+r)^8}, \tag{2}$$

$$R = \frac{2M^3(M+4r)}{r^2(M+r)^4}. \tag{3}$$

From the above expressions of the Kretschmann scalar and Ricci scalar it can be seen that the spacetime has a strong curvature singularity at the center $r = 0$. No null surfaces such as an event horizon exist around the singularity in this spacetime.

This metric this is the solution of Einstein's field equations with an anisotropic fluid source The energy-momentum tensor for anisotropic fluid given as

$$T_{ab} = diag(\rho, p_r, p_\theta, p_\varphi). \tag{4}$$

The solutions of EFE for the energy density and pressures as:

$$\rho = -T^t{}_t = \frac{M^2(M+3r)}{r^2(M+r)^3} \tag{5}$$

$$p_r = T^r{}_r = -\frac{M^2(M+3r)}{r^2(M+r)^3} \tag{6}$$

$$p_\theta = p_\varphi = T^\theta{}_\theta = T^\varphi{}_\varphi = \frac{3M^2}{r^4}\left(1+\frac{M}{r}\right)^{-4} \tag{7}$$

and it is also shown that this metric satisfies all energy conditions, i.e. strong, weak and null energy conditions [6]; The anisotropy in the pressures is:

$$p_r - p_\theta = -\frac{M^2(M^2+4Mr+6r^2)^2}{r^2(M+r)^4} \tag{8}$$

The equation of state (α) for an anisotropic fluid can be written as:

$$\alpha = \frac{p_r + p_\theta + p_\varphi}{3\rho} \tag{9}$$

from the equations eq.(5- 7) the equation of state for this spacetime as

$$\alpha = \frac{2}{\left(3+\frac{M}{r}\right)\left(1+\frac{M}{r}\right)} - \frac{1}{3} \tag{10}$$

where if r tends to zero, equation of state becomes $-1/3$; if r tends to infinity, equation of state becomes $+1/3$.

From the above equation (1) the expansion of component of metric tensor can be written as

$$g_{tt} \approx -\left[1-\frac{2M}{r}+3\left(\frac{M}{r}\right)^2-\dots\right], \qquad (11)$$

it is clear that in the large r limit, this metric is symptotically flat. Even though the metric resembles the Schwarzschild metric at a large distance, near the singularity, the causal structure of this spacetime becomes different from the causal structure of Schwarzschild spacetime.

Shadows of null naked singularity

Even though the metric resembles the Schwarzschild metric at a large distance, near the singularity, the causal structure of this spacetime becomes different from the causal structure of Schwarzschild spacetime. The most analytical solutions of black hole shadows only investigated the case that the geodesic equations for photons can separate variables. For example, In Kerr black hole space-time for the null geodesics has a third motion of constant, namely the Carter constant which is can be found by the calculation of HamiltonJacobi equation, except for the energy E and the z-component of the angular momentum L_z and the photon motion system is integrable.[11].

Let's rewrite the line element 1 in this form:

$$ds^2 = -A(r)dt^2 + \frac{1}{A(r)}dr^2 + +r^2(d\theta^2 + sin^2\theta\, d\phi^2), \qquad (12)$$

where the functions

$$A(r) = \frac{1}{\left(1+\frac{M}{r}\right)^2}, \qquad (13)$$

The Hamilton of a photon is given by

$$H = \frac{1}{2}g^{\mu\nu}P_\mu P_\nu, \qquad (14)$$

The photon motions can be obtained from the Hamiltom equation

$$\dot{P}_\mu = -\frac{\partial H}{\partial x^\mu}, \dot{x}^\mu = \frac{\partial H}{\partial P_\mu}, \qquad (15)$$

where $P_\mu = \frac{dx^\mu}{d\lambda}$ is the four-momentum of the photon, and λ is the affine parameter.

In additional, due to symmetries of the metric one can introduce two integrals of motion, corresponding to cyclic coordinates t and φ, i.e., the conserved quantities of energy and angular momentum, respectively.

$$-P_t = E, P_\varphi = L, \qquad (16)$$

From the Hamiltonian 14 with the eq.16 we can reduce

$$P_r^2 = \frac{E^2}{A(r)^2} - \frac{1}{r^2 A(r)}\left(P_\theta + \frac{1}{\sin^2\theta}L^2\right). \qquad (17)$$

Because of the spherical symmetry, we can choose the orbit of the photon in the equatorial plane, which means$\theta = \frac{\pi}{2}, P^\theta = 0$. Also, the orbit equation for lightlike geodesics is $dr/d\varphi$, then, using eq.16 and eq.17 the orbit equation becomes

$$\left(\frac{dr}{d\varphi}\right)^2 = \left(\frac{P_r}{P_\varphi}\right)^2 = \frac{1}{r^2 A(r)}\left(\frac{r^2}{A(r)}\frac{E^2}{L^2}-1\right). \qquad (18)$$

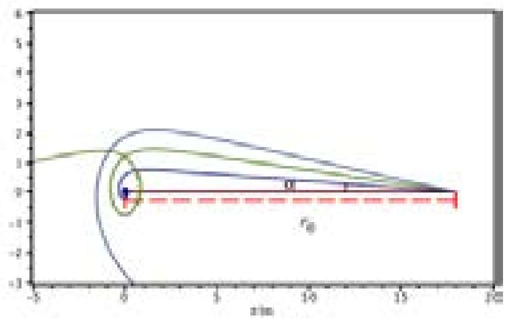

Figure 1 − Formation of a shadow in the case of a null naked singularity

We can see that eq.(18) is the same form as an energy conservation law in one-dimensional classical mechanics $(dr/d\varphi)^2 + V_{eff}(r) = 0$, where the effective potential depends on the impact parameter $b = L/E$.

According to (18), we can rewrite the effective potential for the metric (1)

$$V_{eff} = \frac{1}{r^2}\left(1+\frac{m}{r}\right)^2 - \frac{E^2}{L^2}\left(1+\frac{m}{r}\right)^4. \quad (19)$$

The unstable circular orbits of lightlike geodesics can be found when the equations for effective potential

$$V_{eff} = 0, V_{eff,r} = 0, V_{eff,rr} < 0, \quad (20)$$

From the above equation, one can determine the impact parameter b with a minimum radius of circular orbit

$$\frac{R^2}{A(R)} = b^2, \quad (21)$$

Let us also introduce the function

$$h(r)^2 = \frac{r^2}{A(r)}, \quad (22)$$

it is clear that the impact parameter and the function $h(r)$ are related by $b = h(R)$, then the equation 18 can be rewrite as a following

$$\left(\frac{dr}{d\varphi}\right)^2 = \frac{1}{r^2 A(r)}\left(\frac{h(r)^2}{h(R)^2} - 1\right). \quad (23)$$

Assume that a static observer at radius coordinate r_O sends light rays into the past.

Then, the angle α between such a light ray and the radial direction is can be calculated by

$$\cot\alpha = \frac{\sqrt{g_{rr}}}{\sqrt{g_{\varphi\varphi}}}\frac{dr}{d\varphi}\Big|_{r=r_0} = \frac{\frac{1}{A(r)^{1/2}}}{r}\frac{dr}{d\varphi}\Big|_{r=r_0}, \quad (24)$$

from the eq.(23) and eq.(24) we obtain

$$\cot^2\alpha = \frac{h\,(R)^2}{h\,(r_0)^2} - 1, \quad (25)$$

By elementary trigonometry, we get

$$\sin^2\alpha = \frac{h\,(R)^2}{h\,(r_0)^2}, \quad (26)$$

or

$$\sin^2\alpha = \frac{(R+m)^2}{(r_0+m)^2}. \quad (27)$$

From the condition in eq. (20), in the null naked singularity spacetime, the minimum turning point radius (r_{tp}) of the photon is $r_{tp} = R = 0$, then for an observer the angular size of the shadow is

$$\sin\alpha = \frac{m}{r_0+m}, \quad (28)$$

Then for an observer at a large distance the angular size

$$\alpha \approx \frac{m}{r_0}, \quad (29)$$

Synge calculated the shadow in the Schwarzschild spacetime as [8]

$$\sin^2\alpha_{Sch} = \frac{27m^2}{r_0^2}\left(1-\frac{2m}{r_0}\right). \quad (30)$$

For large distances we have:

$$\alpha_{Sch} \approx \frac{3\sqrt{3}m}{r_0}. \quad (31)$$

Shadow in *q*-metric

In spherical coordinates, the $q-$ metric can be written in a compact and simple form as

$$ds^2 = -g_{tt}dt^2 + g_{rr}dr^2 + \\ +g_{\theta\theta}d\theta^2 + g_{\phi\phi}d\phi^2. \quad (32)$$

where

$$g_{tt} = \left(1-\frac{2m}{r}\right)^{1+q},$$

$$g_{rr} = g_{tt}^{-1}\left(1+\frac{m^2\sin^2\theta}{r^2-2mr}\right)^{-q(2+q)},$$

$$g_{\theta\theta} = r^2 g_{rr}, g_{\phi\phi} = \left(1-\frac{2m}{r}\right)^{-q} r^2\sin^2\theta. \quad (33)$$

This metric is the simplest static vacuum solutions of Einstein's filed equations with quadrupole investigated in [13] and the geometric properties of the metric analyzed in detail. In the literature, this metric is known as the Zipoy–

Voorhees metric, δ - metric, γ - metric and q-metric [14–21]. Interior solutions of Einstein's field equations was found in [22] and the new generating method with the perfect fluid source presented in [23] which includes the multipole moments. Consider that the orbit of the photon in the equatorial plane. The first integral of timelike geodesic equation is

$$g_{\alpha\beta}\dot{x}^{\alpha}\dot{x}^{\beta} = 0. \quad (34)$$

Hence

$$-g_{tt}\dot{t}^2 + g_{rr}\dot{r}^2 + g_{\varphi\varphi}\dot{\varphi}^2 = 0. \quad (35)$$

We have used the expression for the energy E and the angular moment L which are constants of motion that associated with the Killing vector fields $\xi_t = \partial_t$ and $\xi_\varphi = \partial_\varphi$, respectively.

Consider the the boundary curve of the shadow corresponds to past-oriented light rays that asymptotically approach one of the unstable circular light orbits at radius r_{ph}. Therefore we have to consider the limit $R \to r_{ph}$ in (26) for getting the angular radius α_{sh} of the shadow

by the same procedure as in section III,

$$\sin^2\alpha_{sh} = \frac{h(r_{ph})^2}{h(r_0)^2}. \quad (36)$$

If we consider that the parameter $q \neq 0$, then the r_{ph} is

$$r_{ph} = (3+2q)m. \quad (37)$$

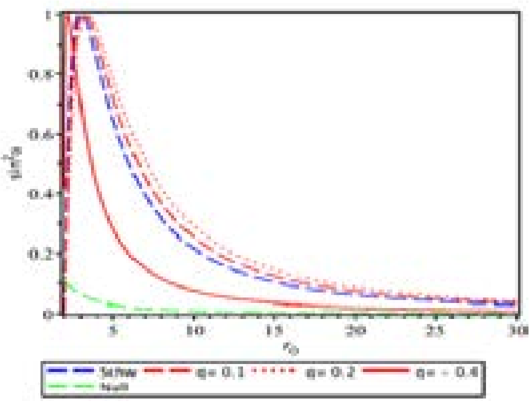

Figure 2 − Angular size of shadows in a different scenarios as a function of sin α_{sh}^2, for Schwarzschild (blue), q − metric (red) and for null naked singularity (green)

The critical value b_{cr} of the impact parameter is connected with r_{ph} by $b_{cr} = h(r_{ph})$

$$b_{cr} = m(2q+1)^{-q-\frac{1}{2}}(2q+3)^{3+\frac{3}{2}}, \quad (38)$$

the final calculation of angular radius of the shadow in the q−metric space-time is

$$sin^2\alpha_{sh} = \frac{m^2}{r_0^2}(1+2q)^{-1-2q} \times$$
$$\times (3+2q)^{3+2q}\left(1-\frac{2m}{r_0}\right)^{1+2q}. \quad (39)$$

It is clear that when $q = 0$ it is reduce to the radius of photon sphere in the Schwarzschild spacetime, i.e., $r_{ph} = 3m$ and, after substitution into (36) we can find the angular radius α_{sh} of the shadow in the Schwarzschild spacetime.

In figure 2 shown the angular size of shadows in a different scenarios. For the large observer at r_0 they have not same angular size. The near the naked singularity apacetime, the size of shadows are quite different and the the size of shadow from the null naked singularity has a small angular size. At the large distance, Eq.(40) becomes

$$\alpha_{sh} = \frac{m}{r_0}(1+2q)^{-\frac{1}{2}-q}(3+2q)^{\frac{3}{2}+q}. \quad (40)$$

If q = 0, for large distances the shadow can be approximated and the expression reduce to the similar angular size of shadow in Schwarzschild spacetime as $\frac{3\sqrt{3}}{r_0}$.

Conclusions and remarks

In this work, we reviewed the null naked singularity solution of Einstein's filed equations that absence of photon sphere and calculated shadow size for a static observer. The angular size of the shadow in any spherically symmetric and static metric, for any position r_0 of a static observer, can be calculated in the simple manner.

We calculated the size of shadows in Null naked singularity and static q-metric spacetime. The near the naked singularity apacetime, a size of shadows are quite different from the Schwarzschild spacetime, the null naked singularity spacetime has a shadow with small angular size. For the q-metric spacetime, the size of the shadow directly depends the value of quadrupole parameter. Near the naked singularity, the quantum gravity effects should be dominant, and therefore, such quantum gravity effects might be manifested or can be observed in the shadow cast by a naked singularity. This will require a detailed analysis of the various features encoded in such shadows.

For the large distance observer at r_0 the null naked singularity and q-metric spacetime asymptotically resembles the Schwarzschild spacetime. As a result, the null naked singularity and static q-metric spacetime can be thought of as a Schwarzschild black hole mimickers.

Reference

1. Akiyama, E.A. " Event Horizon Telescope Results. I. The Shadow of the Supermassive Black Hole in the Center of the Milky Way." *The Astrophysical Journal Letters* Volume 930, Number 2. (2022):L12.
2. Akiyama, E.A. " Event Horizon Telescope Results. V. Physical Origin of the Asymmetric Ring." *The Astrophysical Journal Letters* Volume 875, Number 1. (2019):L5.
3. Perlick, V., Tsupko, O.Y., "Light propagation in a plasma on an axially symmetric and stationary spacetime: Separability of the Hamilton–Jacobi equation and shadow." *Journal of Mathematical Physics* Volume 947, Number 1. (2022):L9.
4. Dey, D., Shaikh, R., Joshi, P.S., "Perihelion precession and shadows near black holes and naked singularities." *Physical Review D* (2020).
5. Joshi, A.B., Dey, D., Joshi, P.S., "Shadow of a naked singularity without photon sphere", *Physical Review D*. Volume 102, (2020):L3-1.
6. Madan, S., Bambhaniya, P., "Tidal force effects and periodic orbits in null naked singularity spacetime." *General Relativity and Quantum Cosmology* (2022).
7. Carter, B., "Global Structure of the Kerr Family of Gravitational Fields." *Physical Review Journals Archive* Volume 174, 1559 (1968):L5.
8. Synge, J.L., "The Escape of Photons from Gravitationally Intense Stars." *Monthly Notices of the Royal Astronomical Society* Volume 131, Pages 463–466, (1966):L3.
9. Toktarbay, S. , Quevedo, H., Abishev, M., Muratkhan, A., "Gravitational field of slightly deformed naked singularities." *European Physical Journal C* Volume 82, 382 (2022).
10. Zipoy, D.M., "Topology of some spheroidal metrics." *Journal of Mathematical Physics* Volume 7, 1137–1143 (1966).
11. Voorhees, B.H., "Static axially symmetric gravitational fields." *Phys. Rev. D* Volume 2, 2119–2122 (1970).
12. Malafarina, D., Magli, G., Herrera, L., in *General Relativity and Gravitational Physics*, *American Institute of Physics Conference Series*, Volume 751, ed. by Espositio, G., Lambiase G., Marmo, G., Scarpetta, G., Vilasi G. (2005), *American Institute of Physics Conference Series*, Volume 751, (1966).
13. Abishev, M., Boshkayev, K., Quevedo, H., Toktarbay, S., "Accretion disks around a mass with quadrupole." *Gravitation, Astrophysics and Cosmology,* (2016).
14. Boshkayev, K., Gasper´ E., ın, Guti´errez- Pin˜eres, A.C., Quevedo, H., Toktarbay, S., "Motion of test particles in the field of a naked singularity." *Physical Review D* Volume 93, (2016):L2.
15. Boshkayev, K., Quevedo, H., Toktarbay, S., Zhami, B., Abishev, M., "On the equivalence of approximate stationary axially symmetric solutions of the Einstein field equations." *Grav. Cosmol.* Volume **22**(4), (2016).
16. Benavides-Gallego, C.A., Abdujabbarov, A., Malafarina, D., Ahmedov, B., Bambi, C, "Charged particle motion and electromagnetic field in Unknown node type: font spacetime." *Physical Review D* Volume 99, (2019):L4-15.
17. Turimov, B., Ahmedov, B., Koloˇs, M., "Axially symmetric and static solutions of Einstein equations with self-gravitating scalar field." *Physical Review D* Volume 98, (2018):L8-15.
18. Stewart, B.W., Papadopoulos, D., Witten, L., Berezdivin, R., Herrera, L., "An interior solution for the gamma metric." *General Relativity and Gravitation* Volume 14(1), 97 (1982).
19. Quevedo, H., Toktarbay, S., "Generating static perfect-fluid solutions of Einstein's equations." *J.Math. Phys.* Volume 56, (2015).

Funded by Al-Farabi KazNU.

IRSTI 27.29.17, 27.29.25, 27.41.19 https://doi.org/10.26577/ijmph.2022.v13.i2.07

R.E. Uteshova[1,2], Zh.M. Kadirbayeva[1,2*],
G. Marat[2], B.B. Minglibayeva[3]

[1]Institute of Mathematics and Mathematical Modeling, Almaty, Kazakhstan
[2]International Information Technology University, Almaty, Kazakhstan
[3]Kazakh National Women Teacher Training university, Almaty, Kazakhstan
*e-mail: zhkadirbayeva@gmail.com
(Received 09 November 2022; received in revised form 21 November 2022; accepted 12 December 2022)

A novel numerical implementation for solving problem for loaded depcag

Abstract. In this work, we propose a new computational approach is implemented to solve a two-point BVP for a loaded differential equation with piecewise constant argument of generalized type (DEPCAG) based on the Dzhumabaev parameterization method. In this method, as parameters, we take the values of the desired solution at the partition points which are chosen taking into account the specifics of the equation. The problem under consideration reduces to an equivalent parametric problem for ordinary differential equations. A solution to this problem, which in turn are found from a system of linear algebraic equations. The found values of the parameters are used to determine the values of the unknown function at the remaining points of the interval by solving auxiliary initial-value problems. We develop a novel numerical implementation for solving the considered a two-point BVP for loaded DEPCAG and provide two examples illustrating its application, where Mathcad software will be used for the calculation.
Keywords: piecewise-constant argument of generalized type, loadings, two-point boundary-value problem, Dzhumabaev parametrization method, numerical solution.

1 Introduction and preliminaries

The study of loaded differential equations is of interest both from the practical and theoretical points of view, in mathematical modeling and in general mathematics itself. In [1-9], various boundary-value problems for loaded differential equations are studied and solved by different methods.

Differential equations with piecewise constant argument of generalized type, introduced by M. Akhmet [10], arise in modeling of diverse phenomena and are widely used in applications such as neural networks, hybrid systems, dynamic systems with discontinuities, etc. The theory of such equations has been extensively developed; see, for instance, [10-15]. However, there still remain open questions regarding boundary-value problems for such equations on a finite interval.

The parametrization method proposed by professor D. Dzhumabaev [16, 17] is an effective method of qualitative investigate and numerical solving BVPs for a wide class of differential and integro-differential equations.

This paper is concerned with solving numerically a two-point BVP for a system of loaded DEPCAG by the modification of Dzhumabaev's parametrization method.

We consider the following a two-point BVP for the system of loaded DEPCAG:

$$\dot{x}(t) = A_0(t)x + A_1(t)x(\theta_1) + \\ +K(t)x(\gamma(t)) + f(t), t \in (0, T), \quad (1)$$

$$B_0x(0) + C_0x(T) = d, x \in R^n, d \in R^n, \quad (2)$$

where $(n \times n)$-matrices $A_0(t)$, $A_1(t)$, and $K(t)$ are continuous on $[0, T]$, the n-vector-function $f(t)$ is piecewise continuous on $[0, T]$ with the possible discontinuity of the first kind at the point $t = \theta_1$; B_0 and C_0 are constant $(n \times n)$-matrices. Here $0 = \theta_0 < \theta_1 < \theta_2 = T$, $\|x\| = \max_{i=\overline{1,n}} |x_i|$.

The argument $\gamma(t)$ is a step function defined as

$$\gamma(t) = \xi_0 \text{ if } t \in [\theta_0, \theta_1); \theta_0 < \xi_0 < \theta_1,$$

and

$\gamma(t) = \xi_1$ if $t \in [\theta_1, \theta_2)$; $\theta_1 < \xi_1 < \theta_2$.

We will call a function $x(t)$ a solution to problem (1), (2) if:

(i) it is continuous on $[0, T]$ and differentiable on $(0, \mathrm{T})$ with the possible exception of the points θ_0 and θ_1, at which the one-sided derivatives exist;

(ii) it satisfies (1) on each interval (θ_{i-1}, θ_i), $i = \overline{1,2}$; at the points θ_0 and θ_1, Eq. (1) is satisfied by the right-hand derivatives of $x(t)$;

(iii) it satisfies the boundary condition (2).

2 A numerical algorithm for solving problem (1), (2)

We divide the interval $[0, T]$ as follows: $[0, T) = \cup_{r=1}^{4}[t_{r-1}, t_r)$. Here $t_0 = \theta_0$, $t_1 = \xi_0$, $t_2 = \theta_1$, $t_3 = \xi_1$, and $t_4 = \theta_2 = T$.

Let $C([0, T], \theta, R^{4n})$ denote the space of function quadruples $x[t] = (x_1(t), x_2(t), x_3(t), x_4(t))$, whose components $x_r: [t_{r-1}, t_r) \to R^n$ are continuous on $[t_{r-1}, t_r)$ and have finite limits $\lim_{t \to t_r - 0} x_r(t)$ for all $r = \overline{1,4}$. The space is equipped with the norm $\|x[\cdot]\|_2 = \max_{\mathrm{r}=\overline{1,4}} \sup_{t \in [t_{r-1}, t_r)} \|x_r(t)\|$.

The restrictions of $x(t)$ to the partition subintervals, denoted by $x_r(t)$ ($x_r(t) = x(t)$ for $t \in [t_{r-1}, t_r)$, $r = \overline{1,4}$), satisfy the following multipoint boundary-value problem

$$\frac{dx_1}{dt} = A_0(t)x_1 + K(t)x_2(t_1) + \\ +A_1(t)x_3(t_2) + f_1(t),\ t \in [t_0, t_1), \tag{3}$$

$$\frac{dx_2}{dt} = A_0(t)x_2 + K(t)x_2(t_1) + \\ +A_1(t)x_3(t_2) + f_1(t),\ t \in [t_1, t_2), \tag{4}$$

$$\frac{dx_3}{dt} = A_0(t)x_3 + K(t)x_4(t_3) + \\ +A_1(t)x_3(t_2) + f_2(t),\ t \in [t_2, t_3), \tag{5}$$

$$\frac{dx_4}{dt} = A_0(t)x_4 + K(t)x_4(t_3) + \\ +A_1(t)x_3(t_2) + f_2(t),\ t \in [t_3, T), \tag{6}$$

$$B_0 x_1(0) + C_0 \lim_{t \to T-0} x_4(t) = d, \tag{7}$$

$$\lim_{t \to t_p - 0} x_p(t) = x_{p+1}(t_p),\ p = \overline{1,3}. \tag{8}$$

Here $f_1(t) = f(t)$ if $t \in [t_0, t_2)$ and $f_2(t) = f(t)$ if $t \in [t_2, t_4)$.

Applying the substitution $x_r(t) = w_r(t) + \mu_r$ on each r-th subinterval, with $\mu_r = x_r(t_{r-1})$, $r = \overline{1,4}$, we pass to the boundary-value problem with parameters μ_r:

$$\frac{dw_1}{dt} = A_0(t)(w_1 + \mu_1) + K(t)\mu_2 + \\ +A_1(t)\mu_3 + f_1(t),\ t \in [t_0, t_1), \tag{9}$$

$$w_1(t_0) = 0, \tag{10}$$

$$\frac{dw_2}{dt} = A_0(t)(w_2 + \mu_2) + K(t)\mu_2 + \\ +A_1(t)\mu_3 + f_1(t),\ t \in [t_1, t_2), \tag{11}$$

$$w_2(t_1) = 0, \tag{12}$$

$$\frac{dw_3}{dt} = A_0(t)(w_3 + \mu_3) + K(t)\mu_4 + \\ +A_1(t)\mu_3 + f_2(t),\ t \in [t_2, t_3), \tag{13}$$

$$w_3(t_2) = 0, \tag{14}$$

$$\frac{dw_4}{dt} = A_0(t)(w_4 + \mu_4) + K(t)\mu_4 + \\ +A_1(t)\mu_3 + f_2(t),\ t \in [t_3, T), \tag{15}$$

$$w_4(t_3) = 0, \tag{16}$$

$$B_0\mu_1 + C_0\mu_4 + C_0 \lim_{t \to T-0} w_4(t) = d, \tag{17}$$

$$\mu_p + \lim_{t \to t_p - 0} w_p(t) = \mu_{p+1},\ p = \overline{1,3}. \tag{18}$$

A pair $(w^*[t], \mu^*)$, whose components are $w^*[t] = (w_1^*(t), w_2^*(t), w_3^*(t), w_4^*(t)) \in C([0, T], \theta, R^{4n})$ and $\mu^* = (\mu_1^*, \mu_2^*, \mu_3^*, \mu_4^*) \in R^{4n}$, is called a solution to problem (9)-(18) if the functions $w_r^*(t)$, $r = \overline{1,4}$, are continuously differentiable on $[t_{r-1}, t_r)$ and satisfy equations (9), (11), (13), (15) with respective initial conditions and additional conditions (17), (18) with $\mu_j = \mu_j^*$, $j = \overline{1,4}$.

Let us show the equivalence between problems (1), (2) and (9)-(18). If a function $x^*(t)$ solves problem (1), (2), then the pair $(w^*[t], \mu^*)$, where $w^*[t] = (x^*(t) - x^*(t_0), x^*(t) - x^*(t_1), x^*(t) - x^*(t_2), x^*(t) - x^*(t_3))$ and $\mu^* = (x^*(t_0), x^*(t_1), x^*(t_2), x^*(t_3))$, is a solution of problem (9)-(15). Conversely, if a pair $(\tilde{w}[t], \tilde{\mu})$ with elements $\tilde{w}[t] = (\tilde{w}_1(t), \tilde{w}_2(t), \tilde{w}_3(t), \tilde{w}_4(t)) \in C([0, T], \theta, R^{4n})$ and $\tilde{\mu} = (\tilde{\mu}_1, \tilde{\mu}_2, \tilde{\mu}_3, \tilde{\mu}_4) \in R^{4n}$, is a solution of (9)-(18), then the function $\tilde{x}(t)$ defined as $\tilde{x}(t) = \widetilde{w}_r(t) + \tilde{\mu}_r, t \in [t_{r-1}, t_r), \mathrm{r} = \overline{1,4},$ and $\tilde{x}(T) = \lim\limits_{t \to T-0} \widetilde{w}_{m+1}(t) + \tilde{\mu}_{m+1}$, will be a solution of the original problem (1), (2).

Let $X_r(t)$ be a fundamental matrix of the equation $\frac{dx}{dt} = A_0(t)x$ on $[t_{r-1}, t_r]$, $\mathrm{r} = \overline{1,4}$. Then we can represent the solutions of initial-value problems (9)-(16) in the following form:

$$w_1(t) = X_1(t) \int\limits_{t_0}^{t} X_1^{-1}(\tau) A_0(\tau) d\tau \, \mu_1 + X_1(t) \int\limits_{t_0}^{t} X_1^{-1}(\tau) K(\tau) d\tau \, \mu_2 +$$
$$+ X_1(t) \int_{t_0}^{t} X_1^{-1}(\tau) A_1(\tau) d\tau \, \mu_3 + X_1(t) \int_{t_0}^{t} X_1^{-1}(\tau) f_1(\tau) d\tau \,, t \in [t_0, t_1), \tag{19}$$

$$w_2(t) = X_2(t) \int\limits_{t_1}^{t} X_2^{-1}(\tau) A_0(\tau) d\tau \, \mu_2 + X_2(t) \int\limits_{t_1}^{t} X_2^{-1}(\tau) K(\tau) d\tau \, \mu_2 +$$
$$+ X_2(t) \int_{t_1}^{t} X_2^{-1}(\tau) A_1(\tau) d\tau \, \mu_3 + X_2(t) \int_{t_1}^{t} X_2^{-1}(\tau) f_1(\tau) d\tau \,, t \in [t_1, t_2), \tag{20}$$

$$w_3(t) = X_3(t) \int\limits_{t_2}^{t} X_3^{-1}(\tau) A_0(\tau) d\tau \, \mu_3 + X_3(t) \int\limits_{t_2}^{t} X_3^{-1}(\tau) K(\tau) d\tau \, \mu_4 +$$
$$+ X_3(t) \int_{t_2}^{t} X_3^{-1}(\tau) A_1(\tau) d\tau \, \mu_3 + X_3(t) \int_{t_2}^{t} X_3^{-1}(\tau) f_2(\tau) d\tau \,, t \in [t_2, t_3), \tag{21}$$

$$w_4(t) = X_4(t) \int\limits_{t_3}^{t} X_4^{-1}(\tau) A_0(\tau) d\tau \, \mu_4 + X_4(t) \int\limits_{t_3}^{t} X_4^{-1}(\tau) K(\tau) d\tau \, \mu_4 +$$
$$+ X_4(t) \int_{t_3}^{t} X_4^{-1}(\tau) A_1(\tau) d\tau \, \mu_3 + X_4(t) \int_{t_3}^{t} X_4^{-1}(\tau) f_2(\tau) d\tau \,, t \in [t_3, T). \tag{22}$$

If we substitute the limit values for $w_r(t)$, $\mathrm{r} = \overline{1,4}$, present in conditions (17) and (18), by their corresponding expressions found from (19)-(22), we arrive at the system of linear algebraic equations in parameters μ_r, $r = \overline{1,4}$:

$$B_0\mu_1 + C_0\mu_4 + C_0 a_4(A_0, T)\mu_4 + C_0 a_4(K, T)\mu_4 +$$
$$+ C_0 a_4(A_1, T)\mu_3 = d - C_0 a_4(f_2, T), \tag{23}$$

$$\mu_1 + a_1(A_0, t_1)\mu_1 + a_1(K, t_1)\mu_2 + a_1(A_1, t_1)\mu_3 -$$
$$-\mu_2 = -a_1(f_1, t_1), \tag{24}$$

$$\mu_2 + a_2(A_0, t_2)\mu_2 + a_2(K, t_2)\mu_2 + a_2(A_1, t_2)\mu_3 -$$
$$-\mu_3 = -a_2(f_1, t_2), \tag{25}$$

$$\mu_3 + a_3(A_0, t_3)\mu_3 + a_3(K, t_3)\mu_4 + a_3(A_1, t_3)\mu_3 -$$
$$-\mu_4 = -a_3(f_2, t_3). \tag{26}$$

Here by $a_r(P, t)$ we denote the unique solutions of the auxiliary initial-value problems

$$\frac{dz}{dt} = A_0(t)z + P(t), t \in [t_{r-1}, t_r),$$

$$z(t_{r-1}) = 0, \mathrm{r} = \overline{1,4}.$$

Let us rewrite system (23)-(26) in the matrix form:

$$\mathrm{Q}(\theta_1)\mu = -F(\theta_1), \mu \in R^{4n}, \tag{27}$$

where

$$F(\theta_1) = (-d + C_0 a_4(f_2, T), a_1(f_1, t_1), a_2(f_1, t_2), a_3(f_2, t_3))$$

and

$$Q(\theta_1) =$$

$$= \begin{pmatrix} B_0 & O & C_0 a_4(A_1,T) & C_0[I + a_4(A_0,T) + a_4(K,T)] \\ I + a_1(A_0,t_1) & a_1(K,t_1) - I & a_1(A_1,t_1) & O \\ O & I + a_2(A_0,t_2) + a_2(K,t_2) & a_2(A_1,t_2) - I & O \\ O & O & I + a_3(A_0,t_3) + a_3(A_1,t_3) & a_3(K,t_3) - I \end{pmatrix},$$

here I and O are the identity matrix and the zero matrix, respectively, both of dimension n.

It may be verified without difficulty that the solvability of problem (1), (2) and that of system (27) are equivalent. The solution of system (27) is a vector $\mu^* = (\mu_1^*, \mu_2^*, \mu_3^*, \mu_4^*) \in R^{4n}$, whose components are $\mu_r^* = x^*(t_{r-1}), r = \overline{1,4}$. To find the values of the solution to problem (1),(2) at the remaining points of $[0,T]$, we plug the values μ_r^* into equations (3)-(6) and solve them as ordinary differential equations subject to the initial conditions $x^*(t_{r-1}) = \mu_r^*$.

Based on the above findings, we develop the following numerical algorithm for solving the boundary-value problem (1),(2).

1. Divide intervals $[t_{r-1},t_r]$, $r = \overline{1,4}$, into M_r parts. Find the approximate values of the coefficients and the right-hand side of (27) by solving the following matrix and vector initial-value problems:

$$\frac{dz}{dt} = A_0(t)z + f_1(t), z(t_0) = 0, t \in [t_0,t_1);$$

$$\frac{dz}{dt} = A_0(t)z + f_1(t), z(t_1) = 0, t \in [t_1,t_2);$$

$$\frac{dz}{dt} = A_0(t)z + f_2(t), z(t_2) = 0, t \in [t_2,t_3);$$

$$\frac{dz}{dt} = A_0(t)z + f_2(t), z(t_3) = 0, t \in [t_3,t_4);$$

$$\frac{dz}{dt} = A_0(t)z + A_0(t), z(t_{r-1}) = 0,$$
$$t \in [t_{r-1},t_r), r = \overline{1,4}\ ;$$

$$\frac{dz}{dt} = A_0(t)z + A_1(t), z(t_{r-1}) = 0,$$
$$t \in [t_{r-1},t_r), r = \overline{1,4}\ ;$$

$$\frac{dz}{dt} = A_0(t)z + K(t), z(t_{r-1}) = 0, t \in [t_{r-1},t_r),$$
$$r = \overline{1,4}\ .$$

2. Construct the linear in parameters

$$Q_*(\theta_1)\mu^* = -F_*(\theta_1), \mu^* \in R^{4n}\ . \qquad (28)$$

Solve system (28) to find μ^*. As noted above, the components of μ^*=$(\mu_1^*, \mu_2^*, \mu_3^*, \mu_4^*)$ are $\mu_r^* = x^*(t_{r-1}), r = \overline{1,4}$.

3. Solve the following initial-value problems

$$\frac{dz}{dt} = A_0(t)z + K(t)\mu_2^* + A_1(t)\mu_3^* +$$
$$+f_1(t), z(t_0) = \mu_1^*, t \in [t_0,t_1];$$

$$\frac{dz}{dt} = A_0(t)z + K(t)\mu_2^* + A_1(t)\mu_3^* +$$
$$+f_1(t), z(t_1) = \mu_2^*, t \in [t_1,t_2];$$

$$\frac{dz}{dt} = A_0(t)z + K(t)\mu_4^* + A_1(t)\mu_3^* +$$
$$+f_2(t), z(t_2) = \mu_3^*, t \in [t_2,t_3];$$

$$\frac{dz}{dt} = A_0(t)z + K(t)\mu_4^* + A_1(t)\mu_3^* +$$
$$+f_2(t), z(t_3) = \mu_4^*, t \in [t_3,t_4]$$

and determine the values of the solution $z^*(t)$ at the remaining points of the partition subintervals.

3 Examples

Example 1. Let us consider the following problem

$$\frac{dx}{dt} = \begin{pmatrix} t^2 & -3 \\ 5t & t+1 \end{pmatrix} x + \begin{pmatrix} 4 & t^3 \\ t & -4 \end{pmatrix} x(\gamma(t)) +$$
$$+ \begin{pmatrix} 1 & t \\ 4 & t^2 - 3 \end{pmatrix} x(1) + f(t), t \in (0,2), \qquad (29)$$

$$\begin{pmatrix} 1 & 8 \\ 4 & 0 \end{pmatrix} x(0) + \begin{pmatrix} 5 & -4 \\ 8 & 9 \end{pmatrix} x(1) = \begin{pmatrix} 46 \\ 187 \end{pmatrix},$$
$$x \in R^2. \qquad (30)$$

Here if $t \in (0,1)$: $\gamma(t) = \xi_0 = \frac{1}{2}$,

$$f(t) = \begin{pmatrix} \frac{31t^3}{8} - 5t^4 + 3t^2 + 10t + 2 \\ 3t^2 - 26t^3 - t^4 + \frac{71t}{4} - \frac{21}{2} \end{pmatrix};$$

if $t \in (1,2)$: $\gamma(t) = \xi_1 = \frac{3}{2}$,

$$f(t) = \begin{pmatrix} \frac{5t^3}{8} - 5t^4 + 3t^2 + 10t - 38 \\ 3t^2 - 26t^3 - t^4 + \frac{31t}{4} + \frac{5}{2} \end{pmatrix}.$$

The exact solution of problem (29), (30) is $x^*(t) = \begin{pmatrix} 5t^2 - 3 \\ t^3 - 1 \end{pmatrix}$.

To solve problem (29), (30) numerically, we implement the proposed algorithm. The interval $[0,2]$ is partitioned into the subintervals $\left[0, \frac{1}{2}\right]$, $\left[\frac{1}{2}, 1\right]$, $\left[1, \frac{3}{2}\right]$, $\left[\frac{3}{2}, 2\right]$. We take the step size $h = 0.05$ to numerically solve the auxiliary initial-value problems on the partition subintervals (step 1 of the algorithm).

Consider the system (28), where

$$Q_*(1) = \begin{pmatrix} 1 & 8 & 0 & 0 & -14.682896 & -10.74399 & -59.087058 & -8.667082 \\ 4 & 0 & 0 & 0 & -8.707397 & 28.771313 & 55.683542 & 50.097028 \\ 0.685574 & -1.788367 & 0.64101 & 1.749837 & -1.306734 & 1.398719 & 0 & 0 \\ 0.70852 & 0.992797 & 1.075304 & -3.217662 & 2.455186 & -1.576427 & 0 & 0 \\ 0 & 0 & 0.662779 & 0.307998 & -2.46031 & 1.374989 & 0 & 0 \\ 0 & 0 & 4.666998 & -1.497835 & 2.255643 & -1.566625 & 0 & 0 \\ 0 & 0 & 0 & 0 & -3.095413 & -0.532168 & -0.827204 & 2.513766 \\ 0 & 0 & 0 & 0 & 4.801938 & -0.492894 & 4.366706 & -0.105952 \end{pmatrix} \quad F_*(1) = \begin{pmatrix} -548.417452 \\ 548.953597 \\ -5.534698 \\ 2.725685 \\ -6.349978 \\ -2.345375 \\ -7.045047 \\ 45.377496 \end{pmatrix}$$

Solving the system (28), we find (step 2 of the algorithm):

$$\mu_1^* = \begin{pmatrix} -2.999981352 \\ -0.999992433 \end{pmatrix},$$

$$\mu_2^* = \begin{pmatrix} -1.750002872 \\ -0.874993786 \end{pmatrix},$$

$$\mu_3^* = \begin{pmatrix} 1.999989979 \\ -0.000015784 \end{pmatrix},$$

$$\mu_4^* = \begin{pmatrix} 8.249993363 \\ 2.374987821 \end{pmatrix}.$$

The results of all calculations are obtained using Mathcad software.

The proximity of the exact solution to the numerical solutions satisfies the estimate (step 3 of the algorithm).

If $h = 0.05$, then

$$\max_{k=\overline{0,40}} \|x^*(t_k) - \tilde{x}(t_k)\| < 0.00002.$$

If $h = 0.025$, then

$$\max_{k=\overline{0,80}} \|x^*(t_k) - \tilde{x}(t_k)\| < 0.000001.$$

If $h = 0.0125$, then

$$\max_{k=\overline{0,160}} \|x^*(t_k) - \tilde{x}(t_k)\| < 0.00000009.$$

Example 2. Let us consider the following problem

$$\frac{dx}{dt} = \begin{pmatrix} t & 1 & t^2 \\ 2 & t & 2t^3 \\ t^2 & 0 & 4t \end{pmatrix} x + \begin{pmatrix} 1 & t & 2 \\ 0 & 5 & 5t \\ 6 & t+2 & 3t \end{pmatrix} x(\gamma(t)) +$$

$$+ \begin{pmatrix} 4t^2 & 6 & 0 \\ 5t & t-3 & 8 \\ 1 & 0 & t \end{pmatrix} x\left(\frac{1}{2}\right) + f(t), t \in (0,1), \tag{31}$$

$$\begin{pmatrix} 2 & 0 & 6 \\ 4 & 2 & 1 \\ 4 & 5 & -7 \end{pmatrix} x(0) + \begin{pmatrix} 1 & 5 & 11 \\ 0 & -4 & 2 \\ 6 & 8 & 9 \end{pmatrix} x(1) = \begin{pmatrix} -109 \\ -65 \\ 59 \end{pmatrix}, x \in R^3. \tag{32}$$

Here

$$\gamma(t)=\xi_0=\frac{1}{4}, f(t)=\begin{pmatrix} \frac{27}{64}t-5t^3-t^4+\frac{131}{8} \\ 18t^3-5t^4-2t^5+13t^2+\frac{425}{16}t+\frac{5119}{64} \\ 3t^2-11t^3+\frac{4671}{64}t+\frac{187}{32} \end{pmatrix}, t\in\left(0,\frac{1}{2}\right);$$

$$\gamma(t)=\xi_1=\frac{3}{4}, f(t)=\begin{pmatrix} \frac{95}{8}-5t^3-\frac{167}{64}t-t^4 \\ 18t^3-5t^4-2t^5+13t^2+\frac{385}{16}t+\frac{4149}{64} \\ 3t^2-11t^3+\frac{4381}{64}t-\frac{679}{32} \end{pmatrix}, t\in\left(\frac{1}{2},1\right).$$

The exact solution of problem (31), (32) is $x^*(t)=\begin{pmatrix} 7t-3 \\ 5t^3+2t \\ t^2-9 \end{pmatrix}$.

To solve problem (31), (32) numerically, we implement the proposed algorithm. The interval $[0,1]$ is partitioned into the subintervals $\left[0,\frac{1}{4}\right]$, $\left[\frac{1}{4},\frac{1}{2}\right]$, $\left[\frac{1}{2},\frac{3}{4}\right]$, $\left[\frac{3}{4},1\right]$. We take the step size $h=0.025$ to numerically solve the auxiliary initial-value problems on the partition subintervals (step 1 of the algorithm).

Solving the system (28), we find (step 2 of the algorithm):

$$\mu_1^*=\begin{pmatrix} -2.999999976 \\ -0.000000021 \\ -9.000000037 \end{pmatrix},$$

$$\mu_2^*=\begin{pmatrix} -1.249999988 \\ 0.578125004 \\ -8.937500018 \end{pmatrix},$$

$$\mu_3^*=\begin{pmatrix} 0.499999994 \\ 1.624999997 \\ -8.749999997 \end{pmatrix}$$

$$\mu_4^*=\begin{pmatrix} 2.249999991 \\ 3.609375057 \\ -8.437499952 \end{pmatrix}.$$

The results of calculations, obtained using Mathcad software, are presented in Table 1 (step 3 of the algorithm).

Table 1 – The proximity of the exact solution $x^*(t)$ to the numerical solutions $\tilde{x}(t)$ of the problem (31), (32)

k	$\mathbf{t_k}$	$\lvert x_1^*(t_k)-\tilde{x}_1(t_k)\rvert$	$\lvert x_2^*(t_k)-\tilde{x}_2(t_k)\rvert$	$\lvert x_3^*(t_k)-\tilde{x}_3(t_k)\rvert$
0	0	0.2422E-7	0.2137E-7	0.3679E-7
1	0.025	0.2275E-7	0.1788E-7	0.3500E-7
2	0.05	0.2134E-7	0.1458E-7	0.3322E-7
3	0.075	0.2000E-7	0.1145E-7	0.3146E-7
4	0.1	0.1873E-7	0.0853E-7	0.2969E-7
5	0.125	0.1750E-7	0.0581E-7	0.2790E-7
6	0.15	0.1632E-7	0.0331E-7	0.2607E-7
7	0.175	0.1516E-7	0.0105E-7	0.2421E-7
8	0.2	0.1402E-7	0.0097E-7	0.2230E-7
9	0.225	0.1287E-7	0.0271E-7	0.2034E-7
10	0.25	0.1171E-7	0.0418E-7	0.1833E-7
11	0.275	0.1052E-7	0.0534E-7	0.1626E-7
12	0.3	0.0927E-7	0.0618E-7	0.1414E-7
13	0.325	0.0794E-7	0.0666E-7	0.1198E-7
14	0.35	0.0650E-7	0.0677E-7	0.0978E-7
15	0.375	0.0493E-7	0.0646E-7	0.0755E-7
16	0.4	0.0319E-7	0.0572E-7	0.0532E-7
17	0.425	0.0126E-7	0.0449E-7	0.0311E-7
18	0.45	0.0092E-7	0.0273E-7	0.0094E-7
19	0.475	0.0338E-7	0.0039E-7	0.0115E-7
20	0.5	0.0617E-7	0.0258E-7	0.0311E-7

Table continuation

$\mathbf{k}$	$\mathbf{t_k}$	$\lvert x_1^*(t_k) - \tilde{x}_1(t_k)\rvert$	$\lvert x_2^*(t_k) - \tilde{x}_2(t_k)\rvert$	$\lvert x_3^*(t_k) - \tilde{x}_3(t_k)\rvert$
21	0.525	0.0571E-7	0.0476E-7	0.0767E-7
22	0.55	0.0530E-7	0.1191E-7	0.1234E-7
23	0.575	0.0499E-7	0.1884E-7	0.0171E-7
24	0.6	0.0481E-7	0.2550E-7	0.2189E-7
25	0.625	0.0481E-7	0.3185E-7	0.2669E-7
26	0.65	0.0503E-7	0.3785E-7	0.3143E-7
27	0.675	0.0554E-7	0.4342E-7	0.3605E-7
28	0.7	0.0640E-7	0.4849E-7	0.4047E-7
29	0.725	0.0768E-7	0.5298E-7	0.4460E-7
30	0.75	0.0947E-7	0.5678E-7	0.4833E-7
31	0.775	0.1185E-7	0.5977E-7	0.5152E-7
32	0.8	0.1493E-7	0.6181E-7	0.5402E-7
33	0.825	0.1884E-7	0.0627E-7	0.5564E-7
34	0.85	0.2372E-7	0.6226E-7	0.5616E-7
35	0.875	0.2973E-7	0.6022E-7	0.5533E-7
36	0.9	0.3707E-7	0.5628E-7	0.5281E-7
37	0.925	0.4597E-7	0.5009E-7	0.4825E-7
38	0.95	0.5668E-7	0.4119E-7	0.4120E-7
39	0.975	0.6951E-7	0.2907E-7	0.3114E-7
40	1	0.8484E-7	0.1306E-7	0.1744E-7

4 Conclusion

In this paper, we developed a numerical algorithm of the Dzhumabaev's parameterization method for solving the linear two-point BVP for the system of loaded DEPCAG. This technique can be applied to various kinds of functional-differential equations.

5 Acknowledgement

This research is funded by the Science Committee of the Ministry of Education and Science of the Republic of Kazakhstan (Grant No. AP08855726).

References

1. Nakhushev A.M. "Nagruzhennye uravnenia i ih primenenie [Loaded equations and their applications]." Moscow: Nauka, 2012. – (In Russian)

2. Dzhenaliev M.T., Ramazanov M.I. "Nagruzhennye uravnenia kak vozmuchenia differencial'nyh uravnenij [Loaded equations as perturbations of differential equations]." Almaty: Gylym, 2010. (In Russian)

3. Abdullaev V.M., Aida-zade K.R. "Numerical method of solution to loaded nonlocal boundary value problems for ordinary differential equations." *Comput. Math. Math. Phys.* 54 (2014): 1096-1109. https://doi.org/10.7868/S0044466914070023

4. Yuldashev T.K., Abdullaev O.Kh. "Unique solvability of a boundary value problem for a loaded fractional parabolic-hyperbolic equation with nonlinear terms." *Lobachevskii J. Math.* 42 (2021): 1113–1123. https://doi.org/10.1134/S1995080221050218

5. Assanova A.T., Kadirbayeva Zh.M. "Periodic problem for an impulsive system of the loaded hyperbolic equations." *Electronic Journal of Differential Equations* 72 (2018): 1-8.

6. Assanova A.T., Imanchiyev A.E., Kadirbayeva Zh.M. "Numerical solution of systems of loaded ordinary differential equations with multipoint conditions." *Comput. Math. Math. Phys.* 58 (2018): 508–516. https://doi.org/10.1134/S096554251804005X

7. Assanova A.T., Kadirbayeva Zh.M. "On the numerical algorithms of parametrization method for solving a two-point boundary-value problem for impulsive systems of loaded differential equations." *Comp. and Applied Math.* 37 (2018): 4966–4976. https://doi.org/10.1007/s40314-018-0611-9

8. Kadirbayeva Zh.M., Kabdrakhova S.S., Mynbayeva S.T. "A Computational Method for Solving the Boundary Value Problem for Impulsive Systems of Essentially Loaded Differential Equations." *Lobachevskii J. of Math.* 42 (2021): 3675- 3683. https://doi.org/10.1134/S1995080222030131

9. Assanova A.T., Bakirova E.A., Kadirbayeva Z.M., Uteshova R.E. "A computational method for solving a problem with parameter for linear systems of integro-differential equations." *Computational and Applied Mathematics*. 39(3) (2020): 248. https://doi.org/10.1007/s40314-020-01298-1

10. Akhmet M., and Yilmaz E. *Neural Networks with Discontinuous/Impact Activations*. New York: Springer, 2014.

11. Akhmet M.U. *Nonlinear hybrid continuous/discrete time models.* Amsterdam-Paris: Atlantis, 2011.

12. Castillo S, Pinto M, Torres R. "Asymptotic formulae for solutions to impulsive differential equations with piecewise constant argument of generalized type." *Electron. J. Differential Equations* 2019 (2019): 1–22.

13. Akhmet M.U. "On the reduction principle for differential equations with piecewise-constant argument of generalized type." *J. Math. Anal. Appl.* 1 (2007): 646-663. https://doi.org/10.1016/j.jmaa.2007.03.010

14. Chiu KS, Pinto M. "Periodic solutions of differential equations with a general piecewise constant argument and applications." *Electron. J. Qual. Theory Differ. Equ.* 2010 (2010): 1–19.

15. Bakirova E.A., Kadirbayeva Zh.M., Nessipbayeva A.N. "Modification of the parametrization method for solving a boundary value problem for loaded DEPCAG." *Journal of Mathematics, Mechanics and Computer Science (Bulletin of KazNU*). 115(3) (2022): 16–24.

16. Dzhumabaev D.S. "Criteria for the unique solvability of a linear boundary-value problem for an ordinary differential equation." *USSR Comput. Math. Math. Phys.* 1 (1989): 34–46.

17. Temesheva S.M., Dzhumabaev D.S., Kabdrakhova S.S. "On one algorithm to find a solution to a linear two-point boundary value problem." *Lobachevskii J. of Math.* 42 (2021): 606-612.

Funded by Al-Farabi KazNU

IRSTI 30.17.53 https://doi.org/10.26577/ijmph.2022.v13.i2.08

Balaji Chandrashekar*, Rudresha Chandrappa,
Vidya Shree Venkatesh and Maruthamanikandan Sokalingam

Presidency University, Bengaluru, India
*e-mail: balaji.c@presidencyuniversity.in
(Received 17 October 2022; received in revised form 24 October 2022; accepted 27 November 2022)

Thermomagnetic ferroconvection in an anisotropic permeable layer exposed to a modulated magnetic field

Abstract. The impact of a sinusoidal mode of magnetic field involving time-dependent on the threshold of magnetic smart liquid advection in a saturated Darcy-permeable framework is investigated using a regular perturbation technique. Aniso tropic permeability and thermal anisotropy are used to describe the flow through permeable medium. The regular perturbation technique is based on minimum amplitude of time-fluctuated magnetic field, the threshold condition is computed with regard to correction in a critical Rayleigh number and wavenumber. Correction in Rayleigh number is identified by modulating the magnetic field, modulation frequency, magnetic parameter, mechanical anisotropy, thermal anisotropy and Vadasz number. At intermediate frequency values, the impact of various physical factors is perceived to be noteworthy. It is found that by fine tuning the frequency of magnetic field modulation, we can either accelerate or postpone the onset of ferroconvection. The most sophisticated scientific application packages, Wolfram Mathematica 11.3 is used to extract the numerical values as well as plotting graphs. The problem sheds some light on convective heat transfer mechanisms in ferromagnetic fluid with time-varying magnetic field.
Keywords: Magnetic liquid, Anisotropy, Stability, Porous medium.

Introduction

A ferrofluid (magnetic nanofluid) is a liquid carrier that includes a solution of nanoscopic magnetic particles immersed in a surfactant coating. In comparison with conventional fluids, magnetic nanofluids are responsive to external magnetic fields even in the absence of gravitational force. Numerous studies on these fluids have been undertaken as an outcome of their diverse applications in computer disk drives, bio-medical, magnetic resonance, robotic systems and dynamic sound system, to mention a few [1, 2]. In order to improve the thermal conductivity of fluids, magnetic nanoparticles are suspended in them. Depending on the nanoparticle, fluids can often have a hundred times greater thermal conductivity than the carrier fluids. In this background, this article attempts a comprehensive review on magnetic fluid owing to its prospective value as a heat transfer phenomenon. An initial description of thermomagnetic convection was given by Finlayson [3], purely by showing how a horizontal surface of magnetic fluid with a variable magnetic susceptibility leads to a non-consistent force of the magnetic field. Future, many authors attracted towards the work of Finlayson and investigated the commencement of magnetic fluid convection under a variety of handy constraints [4-6]. According to recent work performed with the higher order Galerkin technique, it is clarified that the MFD viscosity plays a role in delaying the advent of ferroconvection in a sparsely packed permeable medium exposed to varying gravity fields [7].

In various sectors, such as charges in electrode materials and the resonance of a ferromagnetic field, modulation (oscillation) of a suitable parameter can affect the motion and can result in improved stability. Many theoretical and experimental investigation dealing with fluctuations in the magnetic field on the advection of a magnetic liquid and collision between harmonic and subharmonic conditions have been carried out by numerous authors [8-11] using the Floquet theory. In the articles [12, 13], it is reported that the nonzero flow field of the base state is caused by a double vortex reflecting an external magnetic field modulated symmetrically by two iron bars below and above a ferrofluid layer. The temperature distribution through an electrically charged liquid with internal heat source and couple stresses exposed to magnetic field fluctuation is discussed in detail [14]. Recently, a work is carried out on the advent of magnetic nanofluid under the influence of fluctuated magnetic field ferroconvection in a sparsely arranged permeable structure, it is revealed that convection can be delayed or advanced by controlling the parameters of the study [15].

Temperature profile through fluid-saturated nanopores has piqued the interest of many researchers due to its natural phenomenon and diverse applications in science and technology. This includes the use of geothermal energy resources, the eradication of nuclear excess, aquifers leftover removal, drying processes, and so on. Harton, Rogers, and Lapwood [16, 17] pioneered work on fluid-saturated permeable structures located between two identically flat surfaces and heated directly beneath, and the overall problem has been termed as "Horton-Rogers-Lapwood or Darcy-Benard". Moreover, numerous authors have addressed the topic in depth and the growing number of research in this area is extensively documented [18, 19]. The majority of scientific and experimental research on the advection of flow in porous environments has focused on isotropic materials. More than that, in many real scenarios, the mechanical and thermal assets of porous materials are anisotropic, which can be seen in several industrial and environmental situations as a result of irregular pattern of permeable matrix. Anisotropy can also be noticed in synthetic porous materials like nanoparticles used in chemical manufacturing techniques and coating materials.

The effect of Vadaz number on convection in a Darcy-permeable framework with rotating fluid surface is well explained in the articles [20, 21], it is noted that, unlike the problem in pure liquids, over stable advection in permeable medium at marginal stability is not limited to a specific range of Prandtl number values. By adopting the assumptions that the layer is anisotropic, homogenous, and has an infinite horizontal extent, [22] a theoretical examination of the thermal gradients in the permeable structure is handled. A permeability with anisotropy in thermal diffusivity produces two distinct convection cells when a symmetry axis is assumed and a $(90° - \theta)$ angle is made against perpendicular motion is discussed in detail [23]. In addition, anisotropic permeable matrix subjected to inclined layer, time–periodic temperature/gravity, rotation and double diffusivity has been reported in the literatures [25-28] respectively. The impact of thermal modulation on the advent of the ferroconvection in Darcian permeable materials confirms that subcritical point exists for balanced temperature fluctuation for minimum frequency. Moreover, for unbalanced and bottom wall fluctuation only supercritical state presents [29]. A weakly nonlinear unsteadiness in a rotary permeable anisotropic smart ferrofluid medium using Runge–Kutta–Gill numerical technique has been carried out in recent years [30].

Convection control is a phenomenon that is vital and intriguing in a wide range of magnetic fluid technologies, as well as conceptually challenging. The unamplified Rayleigh-Bénard advection in the ferromagnetic liquid has derived a plenty of attention. Notwithstanding, substantial attention turned out to be devoted to the combined impact of the modulated magnetic field and permeable anisotropy layer on the advent of ferroconvection. In this paper, the presented analysis is with reference to the presumption that the modulation dimension is very minimal and the convective currents are weak, allowing nonlinear effects to be ignored. Thus, depending on the frequency of magnetic field modulation, the advent of ferroconvection can be advanced or delayed in the presence of Darcian-anisotropic permeable medium. Present work aims to provide an introduction to vertical harmonic vibrations, magnetic factors, and anisotropy as they relate to natural convection.

Mathematical model

Permeable medium is considered, which is bound between two plates kept separate by a distance d (see Fig. 1). In mechanical and thermal aspects, the permeable medium is presumed to be closely packed and have vertical anisotropy. A vertical downward gravity force, as well as a uniform temperature difference ΔT between the two surfaces, act on the fluid. The reference rectangular coordinate frame's origin is at the bottom, with the z–axis pointing up vertically.

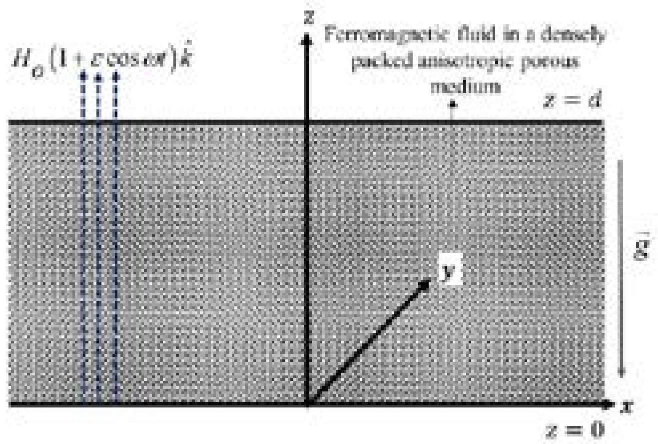

Figure 1 – Physical configuration

The magnetic field imposed externally is time-dependent and is used as

$$\vec{H}_o^{Ext}(t) = H_o^{Ext}(t) = H_o(1+\varepsilon \cos\omega\, t)\hat{k} \quad (1)$$

where H_o is a uniform magnetic field, ε and ω are modulation amplitude and frequency respectively.

The equation of continuity is

$$\nabla \bullet \vec{v} = 0, \quad (2)$$

The conservation of linear momentum with anisotropic inverse permeability $\vec{K} = K_x^{-1}(\hat{\imath}\hat{\imath}+\hat{\jmath}\hat{\jmath}) + K_z^{-1}(\hat{k}\hat{k})$, for modified Darcy model is taken in the form [3, 25, 28]

$$\rho_o\left[\frac{1}{\varepsilon_p}\frac{\partial \vec{v}}{\partial t} + \frac{1}{\varepsilon_p^2}(\vec{v}\bullet\nabla)\vec{v}\right] = \\ = -\nabla p + \rho\vec{g} + \nabla\bullet(\vec{H}\vec{B}) - \mu_f \vec{K}\bullet\ \vec{v}, \quad (3)$$

where $\vec{v}$ is the actual velocity component, ρ is the density, ρ_o is the reference density, ε_p is the porosity, p is the pressure, $\vec{g} = -g\hat{k}$ is the acceleration due to gravity, μ_f is the viscosity, $\vec{H}$ is the overall magnetic field, $\vec{B}$ is the magnetic induction.

We adopted the Oberbeck–Boussinesq approximation in the study. For the derivation of appropriate equations, giving a rigorous basis for the Oberbeck-Boussinesq approximation, one can refer [31]. According to the above-mentioned assumption, and for small departures from reference temperature T_o the density ρ, as a function of temperature T, the density equation of state involving constant coefficient of volume expansion β is given by

$$\rho = \rho_o\big(1-\beta(T-T_o)\big), \quad (4)$$

In energy transport equation the thermal conductivity $\vec{K}_T = K_{T_x}(\hat{\imath}\hat{\imath}+\hat{\jmath}\hat{\jmath}) + K_{T_z}(\hat{k}\hat{k})$ is assumed to be anisotropic and is of the form

$$\varepsilon_p C_1\frac{DT}{Dt} + (1-\varepsilon_p)(\rho_0 C)_s\frac{\partial T}{\partial t} + \mu_o T\left(\frac{\partial \vec{M}}{\partial T}\right)_{V,H}\cdot\frac{D\vec{H}}{Dt} = \nabla\cdot\left(\vec{K}_T\nabla T\right), \quad (5)$$

where $C_1 = \rho_o C_{V,H} - \mu_o \vec{H}\cdot\left(\partial\vec{M}/\partial T\right)_{V,H}$, $C_{V,H}$ is the specific heat at constant volume and magnetic field.

Maxwell's equations, simplified for a non-conducting fluid with no displacement current, become

$$\nabla\bullet\vec{B} = 0, \nabla\times\vec{H} = 0 \quad (6)$$

and

$$\vec{B} = \mu_0\left(\vec{H}+\vec{M}\right) \quad (7)$$

We adopt that the magnetization $\vec{M}$ is aligned with magnetic field, but allows a dependence on the magnitude of the magnetic field as well as temperature,

$$\vec{M} = \frac{\vec{H}}{H}M(H\ ,T) \quad (8)$$

The magnetic equation of state is linearized about the magnetic field H_o and an average temperature T_o to give

$$M = M_o + \chi_m (H - H_o) - K_m (T - T_o) \quad (9)$$

where χ_m and K_m are the differential magnetic susceptibility and the pyromagnetic coefficient respectively. The temperatures of bottom and top surfaces respectively are

$$T(0) = T_o + \left(\frac{1}{2}\right)\Delta T, T(d) = T_o - \left(\frac{1}{2}\right)\Delta T \quad (10)$$

We now look at the necessary conditions for heat flow to continue in the above-noted permeable layer saturated in nanoscopic magnetic liquid. An undisturbed medium will be quiescent and be provided by

$$\vec{v} = \vec{v}_b = \vec{0}, p = p_b(z), \rho = \rho_b(z), T = \\ = T_b(z), \vec{H} = \vec{H}_b = H_o(z,t) = H_o^{Ext}(t), \\ \vec{M} = \vec{M}_b = M_o(z,t), \vec{B} = \vec{B}_b = B_o(z,t) \quad (11)$$

The temperature $T = T_b(z)$ is a solution of

$$K_{T_x}\left(\frac{\partial^2 T_b}{\partial x^2} + \frac{\partial^2 T_b}{\partial y^2}\right) + K_{T_z}\frac{\partial^2 T_b}{\partial z^2} = 0 \quad (12)$$

The solution of (12) subjected to the boundary conditions (10) is

$$T_b = T_o + \Delta T\left(\frac{1}{2} - \frac{z}{d}\right) \quad (13)$$

The magnetic field, magnetization and the related magnetic induction equations followed by (13) and the stationary basic state quantities are

$$H_b = \left[1 + \frac{\chi_o H_o \Delta T \delta}{(1+\chi_o)T_o}\left(\frac{1}{2} - \frac{z}{d}\right)\right] \quad (14)$$

$$M_b = \left[M_o + \frac{H_o \chi_o \Delta T \delta}{(1+\chi_o)T_o}\left(\frac{1}{2} - \frac{z}{d}\right)\right] \quad (15)$$

$$B_b = \mu_o (M_o + H_o) \quad (16)$$

where $\delta = \frac{(1+\varepsilon Re\{e^{-i\omega t}\})}{(1+\chi_o)}$, Re stands for the real part. We do not record the expressions of p_b and ρ_b as these are not explicitly required in the remaining part of the paper.

Linear Stability Analysis

The stability of the system is studied by superimposing infinitesimal disturbances on the basic state and we now have

$$\vec{v} = \vec{v}_b + \vec{v}', p = p_b + p', \rho = \rho_b + \rho', T = \\ = T_b + T', \\ \vec{H} = \vec{H}_b + \vec{H}', \vec{M} = \vec{M}_b + \vec{M}', \vec{B} = \vec{B}_b + \vec{B}', \quad (17)$$

where the prime indicates that the quantities are infinitesimal perturbations.

Substituting (17) into (2) – (9), and using the basic state solutions, we get the linearized equations governing the perturbations in the form

$$\nabla \bullet \vec{v}' = 0, \quad (18)$$

$$\frac{\rho_o}{\varepsilon_p}\left[\frac{\partial \vec{v}'}{\partial t}\right] = -\nabla p' + \beta \rho_o g T' \hat{k} - \mu_f \vec{K} \bullet \vec{v}' + \\ + \mu_o (M_o + H_o)\frac{\partial \vec{H}'}{\partial t} - \\ - \left(\frac{\mu_o \chi_o H_o \delta \Delta T}{T_o d}\right)\frac{\partial \phi'}{\partial z}\hat{k} + \left(\frac{\mu_o \chi_o^2 H_o^2 \delta^2 \Delta T}{T_o^2 (1+\chi_o) d}\right) T' \hat{k}, \quad (19)$$

$$C_3 \frac{\partial T'}{\partial t} - \varepsilon_p C_2 \left(\frac{\Delta T}{d}\right) w' - \frac{\mu_o \chi_o H_o \delta}{T_o (1+\chi_o)} T' \frac{\partial}{\partial t} H_o \delta + \frac{\varepsilon_p \mu_o \chi_o H_o^2 \delta^2}{T_o}\left(\frac{\partial T'}{\partial t} - w' \frac{\Delta T}{d}\right) - \\ - \delta \mu_o \chi_o \left(\frac{\partial \phi'}{\partial z}\right)\frac{\partial}{\partial t} H_o - \mu_o \chi_o H_o \delta \frac{\partial}{\partial t}\left(\frac{\partial \phi'}{\partial z}\right) + \frac{\mu_o \chi_o^2 H_o^2 \Delta T}{T_o (1+\chi_o) d}\delta^2 w' = K_{T_z}\left[\eta \nabla_1^2 T' + \frac{\partial^2 T'}{\partial z^2}\right], \quad (20)$$

$$(1+\chi_o)\nabla^2\phi' - \left(\frac{\chi_o H_o \delta}{T_o}\right)\frac{\partial T'}{\partial z} = 0 \qquad (21)$$

Here ϕ is the magnetic potential and $\vec{H} = \nabla\phi'$, $C_3 = \varepsilon_p C_2 + (1-\varepsilon_p)(\rho_o C)_s$, $C_2 = \rho_o C_{V,H}$, $\vec{v}' = (U', V', W')$. For the ferromagnetic fluid layer and Darcy-anisotropic permeable medium, the boundaries are assumed to be stress-free, isothermal the boundary conditions at $z = 0$ and $z = d$ are

$$W' = \frac{\partial^2 W'}{\partial z^2} = T' = \frac{\partial \phi'}{\partial z} = 0, \qquad (22)$$

By operating curl twice on (19), we omit p' from it, and then we render the resulting equation and (19) – (21) dimensionless by setting

$$(x^*, y^*, z^*)d = (x', y', z'), T^* = \left(\frac{T'}{\Delta T}\right),$$
$$W^* = \left(\frac{C_2 d W'}{K_{T_z}}\right), t^* = \left(\frac{K_{T_z} t}{C_2 d^2}\right),$$
$$\phi^* = \left(\frac{(1+\chi_o)\phi'}{K_m \Delta T d}\right), \omega^* = \left(\frac{C_2 d^2 \omega'}{K_{T_z}}\right), \qquad (23)$$

to obtain non-dimesnional equations as (on dropping '*' for simplicity),

$$\left(\frac{1}{Va}\frac{\partial}{\partial t}\nabla^2 + \nabla_1^2 + \frac{1}{\xi}\frac{\partial^2}{\partial z^2}\right)W =$$
$$= [R + RM_1\psi^2]\nabla_1^2 T - RM_1\psi^2\frac{\partial}{\partial z}(\nabla_1^2\phi), \qquad (24)$$

$$\lambda_p\frac{\partial T}{\partial t} - W + M_2\left(\frac{T_o\psi^2}{\chi_o(1+\chi_o)}\right)\left(\frac{\partial T}{\partial t} - W\right) +$$
$$+\frac{M_2}{\varepsilon_p}\delta^2 W - M_2\frac{1}{H_o}\frac{\partial}{\partial t}H_o\delta\left(\frac{\partial\phi}{\partial z}\right) -$$
$$-M_2\left(\frac{\psi^2}{(1+\chi_o)}\right)\frac{\partial}{\partial t}\left(\frac{\partial\phi}{\partial z}\right) - M_2\frac{1}{H_o}T\frac{\partial}{\partial t}H_o\psi =$$
$$= \eta\nabla_1^2 T + \frac{\partial^2 T}{\partial z^2}, \qquad (25)$$

$$\nabla^2\phi = \frac{\partial T}{\partial z}, \qquad (26)$$

where, $\psi = (1 + \varepsilon\, Re\{e^{-i\omega t}\})$, ω is the frequency of modulation, $\nabla^2 = \nabla_1^2 + \frac{\partial^2}{\partial z^2}$ and $\nabla_1^2 = \frac{\partial^2}{\partial x^2} + \frac{\partial^2}{\partial y^2}$. The dimensionless parameters are $Va = \frac{\varepsilon_p \gamma d^2}{K_z \kappa}$, the Vadasz number, $R = \frac{\beta g \Delta T d^3 K_z}{\gamma\kappa}$, the Darcy-Rayleigh number, $M_1 = \frac{\mu_o \chi_o \Delta T H_o^2}{T_o(1+\chi_o)^3\beta\rho_o g d^3}$, the buoyancy-magnetization parameter, $RM_1 = \frac{\mu_o\chi_o^2(\Delta T)^2 H_o^2 K_z}{\mu_f\kappa(1+\chi_o)^3}$, the magnetic Rayleigh number and $M_2 = \frac{\mu_o\chi_o^2 H_o^2}{C_2(1+\chi_o)T_o}$, the magnetization parameter, $\xi = \frac{K_x}{K_z}$ is the mechanical anisotropy parameter, $\eta = \frac{K_{T_x}}{K_{T_z}}$ is the thermal anisotropy parameter, $\kappa = \frac{K_1}{C_2}$, $\gamma = \frac{\mu_f}{\rho_o}$, $\lambda_p = \frac{C_3}{\varepsilon_p C_2}$.

The parameter M_2 is equivalent to the order of 10^{-6} [3]. Hence M_2 is omitted in further calculations. For simplicity λ_p and ε_p is assumed to be one. At $z = 0$ and $z = d$ the boundary condition (22) in the non-dimesnional form is given by

$$W = \frac{\partial^2 W}{\partial z^2} = T = \frac{\partial\phi}{\partial z} = 0 \qquad (27)$$

After eliminating the coupling between (24) – (26) we obtain a single differential equation for the vertical component of velocity W as

$$L\nabla^2 W = R\nabla^2\nabla_1^2 W + RM_1\psi^2\nabla_1^4 W \qquad (28)$$

where

$$L = \left(\frac{1}{Va}\frac{\partial}{\partial t}\nabla^2 + \nabla_1^2 + \frac{1}{\xi}\frac{\partial^2}{\partial z^2}\right)\left(\frac{\partial}{\partial t} - \eta\nabla_1^2 - \frac{\partial^2}{\partial z^2}\right)$$

The boundary condition (27) in terms of the vertical component of velocity at $z = 0$ and $z = d$ become [32]

$$W = \frac{\partial^2 W}{\partial z^2} = \frac{\partial^4 W}{\partial z^4} = \frac{\partial^6 W}{\partial z^6} = 0 \qquad (29)$$

Solution procedure

In view of small amplitude ($\varepsilon < 1$) assumption, we now seek the eigenfunctions W and eigenvalues R of (28) for a modulated magnetic field that is different from the constant magnetic field. The eigenfunction W and eigenvalue R should be a function of ε and they should be obtained for a given Vadasz number Va, buoyancy-magnetization parameter M_1, mechanical anisotropy parameter ξ, thermal anisotropy parameter η and frequency ω. Hence, we figured out (28) followed by the assumption of Venazian [33] of the form

$$\binom{W}{R} = \binom{W_0}{R_0} + \varepsilon\binom{W_1}{R_1} + \varepsilon^2\binom{W_2}{R_2} + +\varepsilon^3\binom{W_3}{R_3} + \cdots\cdots\cdots \quad (30)$$

On substituting (30) over (28) and comparing the correlative terms up to order of ε^2, yields

$$GW_0 = 0, \quad (31)$$

$$GW_1 = R_1\nabla^2\nabla_1^2 W_0 + R_1 M_1 \nabla_1^4 W_0 + +2\,Re\{e^{-i\omega t}\} R_0 M_1 \nabla_1^4 W_0, \quad (32)$$

$$GW_2 = R_1\nabla^2\nabla_1^2 W_1 + R_2\nabla^2\nabla_1^2 W_0 + +R_1 M_1 \nabla_1^4 W_1 + R_2 M_1 \nabla_1^4 W_0$$

$$+2\,Re\{e^{-i\omega t}\} R_0 M_1 \nabla_1^4 W_1 + +2\,Re\{e^{-i\omega t}\} R_1 M_1 \nabla_1^4 W_0, \quad (33)$$

where

$$G = L\nabla^2 - R_0\left[\frac{\partial^2}{\partial z^2} + (1+M_1)\nabla_1^2\right]\nabla_1^2$$

The function W_0 is the solution of unmodulated Rayeligh-Benard problem in ferromagnetic fluids [3]. The marginally stable solution for that problem is

$$W_0 = \left[e^{i(\alpha_x x + \alpha_y y)}\right] \sin \pi\, z, \quad (34)$$

corresponding to the lowest mode of convection with the Rayleigh number R_0 is given by

$$R_0 = \frac{\left(\frac{\pi^2}{\xi}+\alpha^2\right)(\pi^2+\eta\alpha^2)(\pi^2+\alpha^2)}{\alpha^2[\pi^2+(1+M_1)\alpha^2]}, \quad (35)$$

Following the analysis of [29, 33], one obtains the first non-zero correction to R_0

$$R_{2c} = \frac{R_0^2 M_1^2 \alpha^6}{[\pi^2+(1+M_1)\alpha^2]}\sum_{n=1}^{\infty}\frac{Q_n}{L_n}, \quad (36)$$

where

$$Q_n = -2\begin{pmatrix}(\eta\alpha^2+n^2\pi^2)(n^2\pi^2+\alpha^2)\left(\frac{n^2\pi^2}{\xi}+\alpha^2\right) - R_0\alpha^2[n^2\pi^2+(1+M_1)\alpha^2] \\ -\omega^2\frac{1}{Va}(n^2\pi^2+\alpha^2)^2\end{pmatrix}$$

$$L_n = \begin{pmatrix}(\eta\alpha^2+n^2\pi^2)(n^2\pi^2+\alpha^2)\left(\frac{n^2\pi^2}{\xi}+\alpha^2\right) - R_0\alpha^2[n^2\pi^2+(1+M_1)\alpha^2] \\ -\omega^2\frac{1}{Va}(n^2\pi^2+\alpha^2)^2\end{pmatrix}^2 +\omega^2\left(-\frac{1}{Va}(\eta\alpha^2+n^2\pi^2)(n^2\pi^2+\alpha^2)^2 - (n^2\pi^2+\alpha^2)\left(\frac{n^2\pi^2}{\xi}+\alpha^2\right)\right)^2$$

Results and discussion

The outcome of time-periodic magnetic field fluctuation on the onset of ferroconvection in a horizontal anisotropic densely arranged permeable layer is investigated using the linear stability analysis, the analytical solution was accomplished by means of the standard normal mode approach proposed by Venezian [33]. The shift in the correction to the critical Rayleigh number R_{2c} equation is computed by means of the regular perturbation technique as a function of the modulated magnetic field frequency ω, magnetic parameter M_1, mechanical anisotropy parameter ξ, thermal anisotropy parameter η and Vadasz number Va and the results are depicted with the help of Figures 2 through 5. The stabilizing or destabilizing impact of magnetic field fluctuation is determined by the sign of R_{2c}. A positive R_{2c} means supercritical instability occurs while a negative R_{2c} means subcritical instability occurs, in contrast to system without time-varying magnetic field.

Figure 2(a) and 2(b) shows the variability of R_{2c} on ω and M_1 at $\xi = 0.7$, $\eta = 0.5$ and $Va = 5$. Among these figures it is obvious that an increament in M_1 augments the magnitude of the R_{2c}, provided ω is minimum (see fig. 2(a)), while moderate and large ω (see fig. 2(b)) decrements the magnitude of

R_{2c}. It is proved in Fig. 2(a) that at weak modulation frequency, $R_{2c} < 0$ signifying that the magnetic field modulation destabilizes the physical framework while from Fig. 2(b), it is clear that $R_{2c} > 0$ for moderate and strong frequency. It implies that R_{2c} stabilizes the framework of the problem.

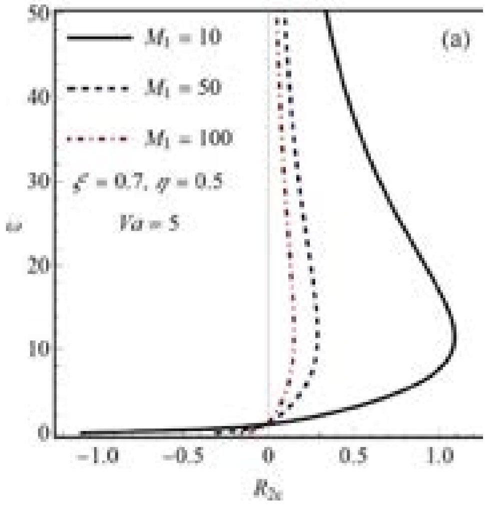

Figure 2(a) – Plot of small and moderate ω verses R_{2c} with variation in M_1.

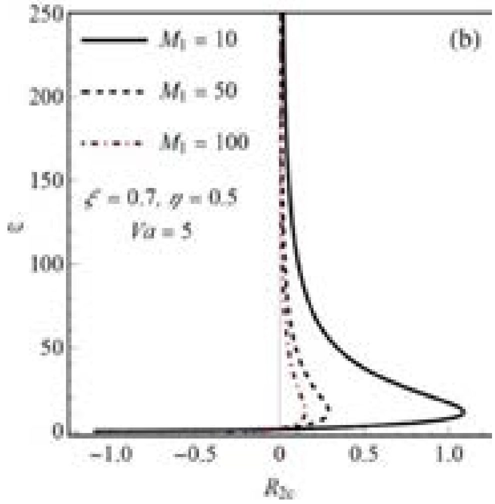

Figure 2(b) – Plot of large ω verses R_{2c} with variation in M_1.

The diversification of R_{2c} upon ω and Va for a specific term $\xi = 0.7$, $\eta = 0.5$ and $M_1 = 50$ is shown in Figures 3(a) and 3(b). We observe from this figures that as raising Va advances the range of R_{2c}. At $\omega = 10$, the peak point of R_{2c} spreads by enhancing Va. The force of Vadasz number Va on the steadiness of the mechanism is exactly opposite to M_1. The most notable outcome of the problem can be elucidated by exploring the outcomes of Figs. 2-3. Comparing the Vadasz number discrepancy with magnetic parameter, we reveal that the least value of R_{2c} is lower. This explicitly reveals that over M_1, the Vadasz number plays a vital role in augmenting ferroconvection and magnetic number is a crucial in postponing ferroconvection.

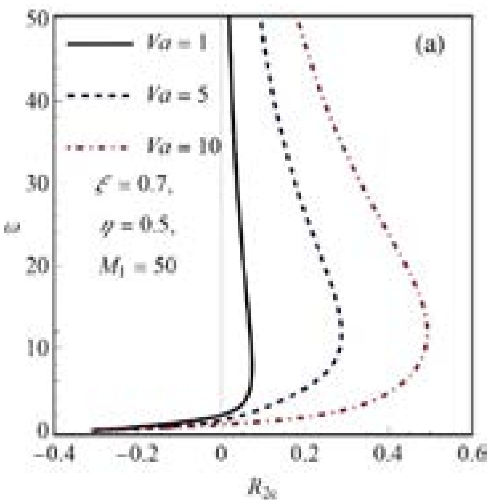

Figure 3(a) – Plot of small and moderate ω verses R_{2c} with variation in Va.

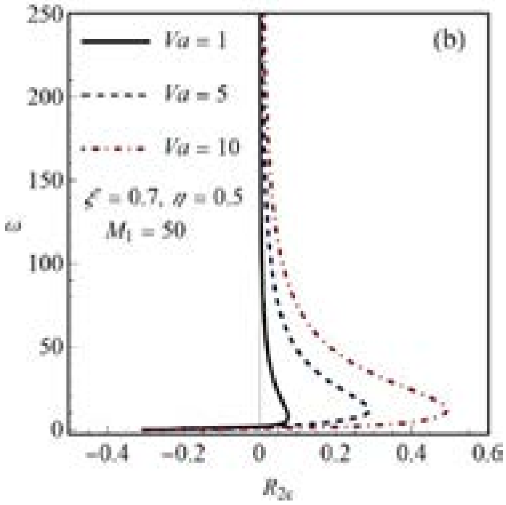

Figure 3(b) – Plot of large ω verses R_{2c} with variation in Va.

The force of mechanical anisotropy ξ on R_{2c} at $M_1 = 50$, $\eta = 0.5$ and $Va = 5$ is shown in Figures 4(a) and 4(b) for weak and moderately large ωrespectively. We note that a rise in the range of ξ results in a fall in the range of R_{2c}. This signifies that, the impact of growth in ξ, minimizes the outgrowth of time-varying magnetic field. It is meaningful to emphasize that at moderate and significant value of frequency, $\xi = 0.1, 0.5, 0.7$ experience a strong destabilizing influence. Conversely, at small value of ω, mechanical anisotropy $\xi = 0.1, 0.5, 0.7$minimizes the fluctuation impact of magnetic force.

The result of thermal anisotropy η is shown in 5 (a) and 5 (b) to elucidate the system's stableness for a fixed value of $M_1 = 50$, $\xi = 0.7$ and $Va = 5$. According to our observation, the large value of η delays the onset of convection as expected when η increases as a function of R_{2c}.

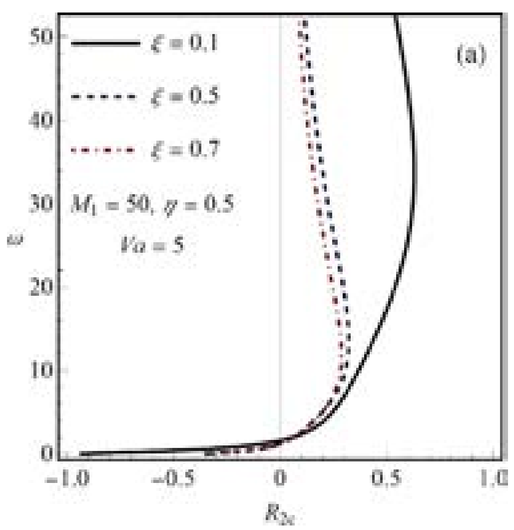

Figure 4(a) – Plot of small and moderate ω verses R_{2c} with variation in ξ.

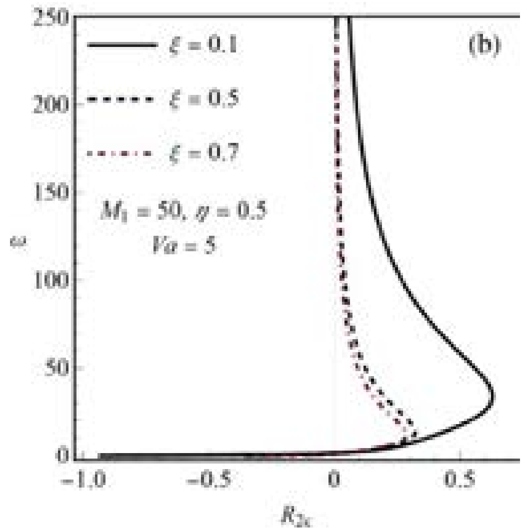

Figure 4(b) – Plot of large ω verses R_{2c} with variation in ξ.

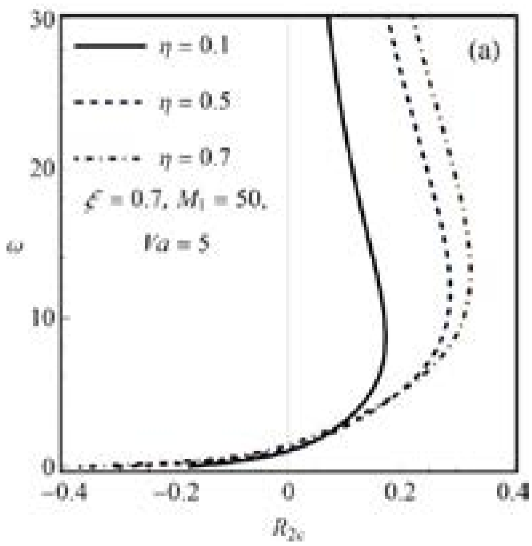

Figure 5(a) – Plot of small and moderate ω verses R_{2c} with variation in η.

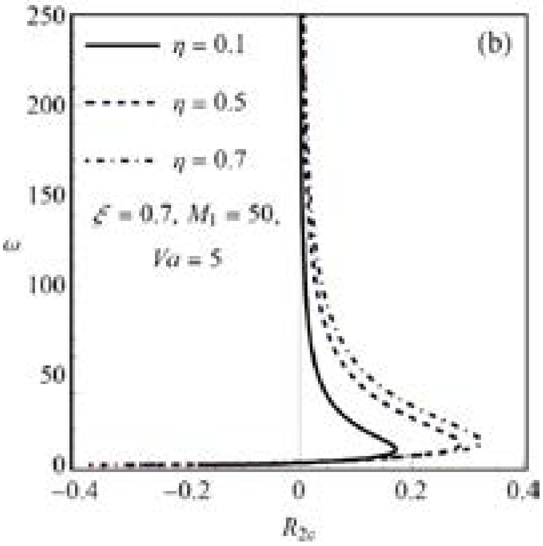

Figure 5(b) – Plot of large ω verses R_{2c} with variation in η.

Conclusions

The impact of magnetic field fluctuation on the advent of nanoscopic magnetic liquid advection in a thickly condensed anisotropic saturated permeable configuration is carefully elucidated adopting stability test and the succeeding conclusions are outlined:

- The weak frequency ω of magnetic field fluctuation is destabilizing while strong frequency of modulated magnetic field is continuously stabilizing.
- The effect of magnetic mechanism M_1 on magnetic field modulation is to stabilize at minute frequency and destabilize at balanced and strong frequency.
- The outcome of Vadasz number Va makes system stable expect for minute values of ω in the modulated magnetic field.
- At moderate and large ω, an increase in mechanical anisotropy ξ strengthens the impact of magnetic field fluctuation, whereas an increase in thermal anisotropy η weakens the impact of fluctuated magnetic field. However, at low ω, enhancing the parameters ξ and η gives opposite result of modulated magnetic field.
- The outcome of magnetic field fluctuation vanishes at high ω in each case.

References

1. Bashtovoy, V, and B M Berkovsky. *Magnetic Fluids and Applications Handbook*. Begell House, 1996.
2. Odenbach, Stefan. *Ferrofluids: Magnetically Controllable Fluids and Their Applications*. Vol. 594. Springer, 2008.
3. Finlayson, B A. “Convective Instability of Ferromagnetic Fluids.” *Journal of Fluid Mechanics* 40, no. 4 (1970): 753–67.
4. Gupta, M Das, and A S Gupta. “Convective Instability of a Layer of a Ferromagnetic Fluid Rotating about a Vertical Axis”. *International Journal of Engineering Science* 17, no. 3 (1979): 271–77.
5. Stiles, P. J., F. Lin, and P. J. Blennerhassett. “Heat Transfer through Weakly Magnetized Ferrofluids”. *Journal of Colloid And Interface Science* 151, no. 1 (1992): 95–101.
6. Maruthamanikandan, S., Nisha Mary Thomas, and Soya Mathew. “Thermorheological and Magnetorheological Effects on Marangoni-Ferroconvection with Internal Heat Generation”. *Journal of Physics: Conference Series* 1139, no. 1 (2018).
7. Vidya Shree, V, C Rudresha, C Balaji, and S Maruthamanikandan. “Effect of MFD Viscosity on Ferroconvection in a Fluid Saturated Porous Medium with Variable Gravity”. *Journal of Mines, Metals and Fuels* 70, no. 3A (2022): 98–103.
8. Aniss, S., M. Belhaq, and M. Souhar. “Effects of a Magnetic Modulation on the Stability of a Magnetic Liquid Layer Heated from Above”. *Journal of Heat Transfer* 123, no. 3 (2001): 428–33.
9. Singh, Jitender, and Renu Bajaj. “Parametric Modulation in the Taylor–Couette Ferrofluid Flow”. *Fluid Dynamics Research* 40, no. 10 (2008): 737–52.
10. Engler, H., and S. Odenbach. "Influence of parametric modulation on the onset of thermomagnetic convection". In *PAMM: Proceedings in Applied Mathematics and Mechanics*, vol. 9, no. 1, pp. 515-516. Berlin: WILEY-VCH Verlag, 2009.
11. Belyaev, A V, and B L Smorodin. “Convection of a Ferrofluid in an Alternating Magnetic Field”. *Journal of Applied Mechanics and Technical Physics* 50, no. 4 (2009): 558–65.
12. Lange, Adrian, and Stefan Odenbach. “Thermomagnetic Convection in Magnetic Fluids Subjected to Spatially Modulated Magnetic Fields”. *Physics Procedia* 9 (2010): 171–75.
13. Lange, Adrian, and Stefan Odenbach. “Patterns of Thermomagnetic Convection in Magnetic Fluids Subjected to Spatially Modulated Magnetic Fields”. *Physical Review E* 83, no. 6 (2011): 66305.
14. Keshri, Om Prakash, Anand Kumar, and Vinod K. Gupta. “Effect of Internal Heat Source on Magneto-Stationary Convection of Couple Stress Fluid under Magnetic Field Modulation”. *Chinese Journal of Physics* 57, no. 2018 (2019): 105–15.
15. Balaji, C, C Rudresha, V Vidya Shree, and S Maruthamanikandan. “Ferroconvection In A Sparsely Distributed Porous Medium With Time-Dependent Sinusoidal Magnetic Field”. *Journal of Mines, Metals and Fuels* 70, no. 3A (2022): 28–34.
16. Horton, C W, and F T Rogers Jr. “Convection Currents in a Porous Medium”. *Journal of Applied Physics* 16, no. 6 (1945): 367–70.
17. Lapwood, ER303660032. “Convection of a Fluid in a Porous Medium”. In *Mathematical Proceedings of the Cambridge Philosophical Society*, 44:508–21. Cambridge University Press, 1948.
18. Nield, Donald A, and Adrian Bejan. *Convection in Porous Media*. Vol. 3. Springer, 2006.

19. Vafai, Kambiz. *Handbook of Porous Media*. Crc Press, 2015.

20. Vadasz, Peter. "Coriolis Effect on Gravity-Driven Convection in a Rotating Porous Layer Heated from Below". *Journal of Fluid Mechanics* 376 (1998): 351–75.

21. Govender, S. "Vadasz Number Influence on Vibration in a Rotating Porous Layer Placed Far Away from the Axis of Rotation". *Journal of Heat Transfer* 132, no. 11 (2010).

22. Tyvand, Peder A. "Thermohaline Instability in Anisotropie Porous Media". *Water Resources Research* 16, no. 2 (1980): 325–30.

23. Storesletten, Leiv. "Natural Convection in a Horizontal Porous Layer with Anisotropic Thermal Diffusivity". *Transport in Porous Media* 12, no. 1 (1993): 19–29.

24. Rees, D. A.S., and A. Postelnicu. "The Onset of Convection in an Inclined Anisotropic Porous Layer". *International Journal of Heat and Mass Transfer* 44, no. 21 (2001): 4127–38.

25. Malashetty, M. S., and D. Basavaraja. "Effect of Time-Periodic Boundary Temperatures on the Onset of Double Diffusive Convection in a Horizontal Anisotropic Porous Layer". *International Journal of Heat and Mass Transfer* 47, no. 10–11 (2004): 2317–27.

26. Govender, Saneshan. "On the Effect of Anisotropy on the Stability of Convection in Rotating Porous Media". *Transport in Porous Media* 64, no. 3 (2006): 413–22.

27. Saravanan, S. "Centrifugal Acceleration Induced Convection in a Magnetic Fluid Saturated Anisotropic Rotating Porous Medium". *Transport in Porous Media* 77, no. 1 (2009): 79–86.

28. Gaikwad, S. N., M. S. Malashetty, and K. Rama Prasad. "Linear and Non-Linear Double Diffusive Convection in a Fluid-Saturated Anisotropic Porous Layer with Cross-Diffusion Effects". *Transport in Porous Media* 80, no. 3 (2009): 537–60

29. Thomas, Nisha Mary, Soya Mathew, and S Maruthamanikandan. "Effect of Time-Dependent Sinusoidal Boundary Temperatures on the Onset Of Ferroconvection in a Porous Medium". *Journal of Mines, Metals and Fuels* 70, no. 3A SE-Articles (July 12, 2022): 78–83.

30. Mahajan, Amit, and Hemant Parashar. "Linear and Weakly Nonlinear Stability Analysis on a Rotating Anisotropic Ferrofluid Layer". *Physics of Fluids* 32, no. 2 (2020).

31. Rajagopal, K R, M Ruzicka, and A R Srinivasa. "On the Oberbeck-Boussinesq Approximation". *Mathematical Models and Methods in Applied Sciences* 6, no. 08 (1996): 1157–67.

32. Chandrasekhar, Subrahmanyan. "Hydrodynamic and Hydromagnetic Stability". *International Series of Monographs on Physics*, 1961.

33. Venezian, Giulio. "Effect of Modulation on the Onset of Thermal Convection". *Journal of Fluid Mechanics* 35, no. 2 (1969): 243–54.

Funded by Al-Farabi KazNU

IRSTI 27.15.25 https://doi.org/10.26577/ijmph.2022.v13.i2.09

A.T. Nurtazin, Z.G. Khisamiev*

Institute of Information and Computational technologies, Pushkin 124, Almaty, Kazakhstan
*e-mail: khisamievZ@mail.ru

(Received 17 November 2022; received in revised form 01 December 2022; accepted 07 December 2022)

Companions of fields of rational and real algebraic numbers

Abstract. Companions of the field of rational numbers and a real-closed algebraic expansion of the field of rational numbers are studied. The description of existentially closed companions of a real-closed algebraic expansion of a field of rational numbers refers to the field of study of classical algebraic structures. The general theory of companions and existentially closed companions, built on the basis of Fraisse's classes in the works of A.T. Nurtazin, is included in the classical field of existentially closed theories in model theory. The basic concept of a companion: two models of the same signature are called companions if for any finite submodel of one of them, there is an isomorphic finite submodel in the other. This approach, applied to specific classical structures and their theories, provides new tools for the study of these objects. The study of the companion class of rational and algebraic real number fields reveals companion fields containing transcendental and possibly algebraic elements with special properties of polynomials defining these elements.

Keywords: companion, field of rational numbers, real closed field, algebraic field extension, algebraic element, transcendental element.

Introduction

The theory of existential closure arose in the middle of the twentieth century in the works of one of the recognized classics of model theory Abraham Robinson [1], [2], as well as in the works [3] – [8]. Currently, it is one of the most significant and most developed areas of modern model theory. In previous studies, the most basic form of the concept of companion theory, widely known in the theory of existential closure, is introduced and studied. The criterion of the countable categoricity of this companion theory was found. Some properties of existentially closed and forcing companions have been studied [3] – [9]. Another promising approach to constructing the theory of existentially closed structures based on Fraisse's works [6] is developed in [9] – [16].

Naturally, the development of the general theory of existentially closed companions should be accompanied by the study of classical structures and theories. Historically, one of the classical mathematical objects is the field of rational numbers and the field of all algebraic real numbers. The work studies companion extensions of the named fields. This study is an example of studying a classical object through an approach developed by Nurtazin A.T. and based on Fraisse classes.

The aim and objectives of the study

The purpose of the work is to describe the companions of the fields of rational and real numbers. For this, for each of the named fields, companions of two types are described, namely, purely transcendental extensions and subsequent algebraic extensions of purely transcendental extensions.

Literature review and problem statement

Let: $\mathbb{Q}$ be the field of rational numbers; $\mathbb{R}$ is a real closed algebraic extension of the field $\mathbb{Q}$; $\mathbb{P}[\overline{x}]$, $\mathbb{P}(\overline{x})$ are, respectively, the ring of polynomials and the field of quotients over the field $\mathbb{P}$ of independent variables $\overline{x}=(x_1,\ldots,x_n)$. All used and not given definitions and designations are taken from the monograph [15]. The basic concept of a companion: two models of the same signature are called companions if for any finite submodel of one of them, there is an isomorphic finite submodel in the other. Consider some basic companions of the field $\mathbb{P}$. The class of companions of the field $\mathbb{P}$ is denoted by $C(\mathbb{P})$.

Obviously, purely algebraic field extensions are not its companions. In turn, the following theorem is devoted to the first basic companions of the field, which are purely transcendental extensions.

Materials and methods

The work uses classical algebraic methods for constructing transcendental and algebraic extensions of this field. To describe a simple algebraic extension $\mathbb{P}(\overline{x})[x]/f$ a purely transcendental extension $\mathbb{P}(\overline{x})$ of the field $\mathbb{P}$, as a companion of f, the set of zeros of the polynomial n is studied and a method for recognizing the companions of the original field $\mathbb{P}$ is indicated.

Results and Discussion

COMPANIONS

Field of quotients

THEOREM 1. Let $\mathbb{P}$ have a field of characteristic 0. Then, the field of quotients $\mathbb{P}(\overline{x})$ is a companion of the field $\mathbb{P}$ i.e. $\mathbb{P}(\overline{x})\in C(\mathbb{P})$.

Proof. Each finite submodel of the ring $\mathbb{P}$ is a submodel of the field $\mathbb{P}(\overline{x})$. Conversely, let there be a finite submodel $\mathfrak{F}$ of the field $\mathbb{P}(\overline{x})$, we can assume that $\mathfrak{F}$ is given by a finite system of equalities and inequalities ($\neq$), the right and left parts of which contain elements $\mathfrak{F}$ and the operations of addition and multiplication of the field $\mathbb{P}(\overline{x})$. We transform this system of equalities and inequalities into an equivalent system $\mathbb{P}(\overline{x})$ $\& S_i(\overline{x})=0 \,\&\, \& T_j(\overline{x})\neq 0$, where $S_i(\bar{x}) = \frac{f_i(\bar{x})}{g_i(\bar{x})}, T_j(\bar{x}) = \frac{u_j(\bar{x})}{v_j(\bar{x})}$ here $f_i(\bar{x}), g_i(\bar{x}), u_j(\bar{x}), v_j(\bar{x}) \in \mathbb{P}[\bar{x}], g_i(\bar{x}), v_j(\bar{x}) \neq 0$

The latter system is equivalent in $\mathbb{P}[\overline{x}]$ system of equations and one inequality $\&(f_i(\bar{x}) = 0)\&T(\bar{x}) = \prod g_i(\bar{x})\, u_j(\bar{x}) v_j(\bar{x}) \neq 0$, where $f_i(\overline{x}), g_i(\overline{x}), u_j(\overline{x}), v_j(\overline{x}) \in \mathbb{P}[\overline{x}], g_i(\overline{x}), v_j(\overline{x}) \neq 0$.

Let us prove the existence of a set $\overline{a}=(a_1,...,a_n)\in\mathbb{P}$, such that in $\mathbb{P}$ is fulfilled $\&(f_i(\bar{a}) = 0)\&T(\bar{a}) \neq 0$ $(\mathbb{P}|=\&(f_i(\bar{a}) = 0)\&T(\bar{a}) \neq 0)$. For any choice of $\bar{a} = (a_1, \ldots, a_n) \in \mathbb{P}$, the equality $\&f_i(\bar{a}) = 0$is obvious, since all the coefficients of the variables and the free terms in $\& f_i(\overline{x})$ are equal to zero. By induction on the number of variables n, we prove the existence of $\bar{a} = (a_1, \ldots, a_n) \in \mathbb{P}$, which is fulfilled $\mathbb{P}\,|{=}\,T(\overline{a})\neq 0$. For $n=1$ we choose $a_1\in\mathbb{P}$ which is not a root $T(x_1)$.

Step of induction. Let $\bar{a}_{n-1} = (a_1, \ldots, a_{n-1}) \in \mathbb{P}$ be such that the higher coefficient of the polynomial $T(\overline{x})$ considered as a polynomial of x_1 over the ring $\mathbb{P}[\overline{x}_{n-1}]$ is not zero. Then, the polynomial $T(\bar{a}_{n-1}, x_n) \neq 0$ and hence there is $a_n\in\mathbb{P}$, such that $\mathbb{P}| = T(\bar{a}) \neq 0$ is satisfied. So $\mathbb{P}|=\&(f_i(\bar{a}) = 0)\&T(\bar{a}) \neq 0$ is done.

The theorem has been proved.

CONSEQUENCE 1. Let $R_i(\overline{x}), S_j(\overline{x})\in\mathbb{P}(\overline{x})$, here $\mathbb{P}$ is formally a real field. The system $\& R_i(\overline{x})=0 \,\&\, \& S_j(\overline{x})\neq 0$ is equivalent in $\mathbb{P}(\overline{x})$ system of one equation and one inequality $P_1(\overline{x})=0 \,\&\, P_2(\overline{x})\neq 0$ where $P_1(\overline{x}), P_2(\overline{x})\in\mathbb{P}[\overline{x}]$.

Simple algebraic extensions

Let $A_f = \{ (\bar{a}, a) | f(\bar{a}, a) = 0, \bar{a}, a \in \mathbb{P}\}$be an annihilator f, where $f(\overline{x},x)\in\mathbb{P}(\overline{x})[x]$. When considering algebraic extensions of the field $\mathbb{P}(\overline{x})$ by means of an irreducible polynomial $f(\overline{x},x)\in\mathbb{P}(\overline{x})[x]$, we will assume that $f(\overline{x},x)\in\mathbb{P}[\overline{x},x]$ and has content 1, as a polynomial in x over the ring $\mathbb{P}[\overline{x}]$.

Then, the divisibility of any polynomial $g(\overline{x},x)\in\mathbb{P}(\overline{x})[x]$ by $f(\overline{x},x)$ is equivalent to the divisibility of a polynomial $g'[\overline{x},x]\in\mathbb{P}(\overline{x})[x]$ such that $g(\overline{x},x)=g'(\overline{x},x)\dfrac{p(\overline{x})}{q(\overline{x})}$, where $g'[\overline{x},x]$is a polynomial with content 1 over the ring $\mathbb{P}[\overline{x}]$, and $q(\overline{x})$ is the least common multiple of the denominators of the coefficients in $g(\overline{x},x)$.

Next, the field $\mathbb{P}$ is one of the fields $\mathbb{Q},\mathbb{R}$.

Consider a simple algebraic extension $\mathbb{P}(\overline{x})[x]/f$ of the field that is the companion of the field $\mathbb{P}$.

THEOREM 2. Let $f(\overline{x},x)$ be an irreducible polynomial over the field $\mathbb{P}(\overline{x})$. Then, the algebraic extension $\mathbb{P}(\overline{x})[x]/f$ of the field $\mathbb{P}(\overline{x})$ is a companion $\mathbb{P}$ if and only if the condition is met: if an arbitrary polynomial $g(\overline{x},x)$ is not divisible by $f(\overline{x},x)$, then there is a tuple $(\overline{a},a)\in\mathbb{P}$ such that $g(\overline{a},a)\in A_f\setminus A_g$ is satisfied.

Proof. Necessity. Let $\{c_1,...,c_k\}\in\mathbb{P}$ be all coefficients of polynomials $g(\overline{x},x)$ and $f(\overline{x},x)$. By the primitive element theorem, there exists an irreducible polynomial $p(y)\in\mathbb{Q}[y]$ and an element $c^*\in\mathbb{P}$ such that $c_i=q_i(c^*),q_i(y)\in\mathbb{Q}[y]$.

Let us replace each of the elements $c_1,...,c_k$ by $q_i(c^*)$ in the polynomials $g(\overline{x},x)$ and $f(\overline{x},x)$, and obtain $g^*(\overline{x},x)=g(\overline{x},x)$ and $f^*(\bar{x},x)=f(\bar{x},x)$,$g^*(\bar{x},x),f^*(\bar{x},x)\in\mathbb{Q}(\bar{x})[x]$.

We have that $g^*(\overline{x},x)$ is not divisible by $f^*(\bar{x},x)$ in $\mathbb{P}(\overline{x})[x]$ ($\mathbb{P}(\bar{x})[x]| = f^*(\bar{x},x)\boxed{|}g^*(\bar{x},x)) \Leftrightarrow \mathbb{P}(\bar{x})[x]| = f^*(\bar{x},x)\boxed{|}g^*(\bar{x},x) \Rightarrow$ there is $(\bar{a},a)\in\mathbb{P}$ such that $g^*(\bar{a},a)\in A_{f^*}\setminus A_{g^*}\Leftrightarrow g(\bar{a},a)\in A_f\setminus A_g$ is satisfied. The necessity has been proved.

Sufficiency. By virtue of consequence 1, we can assume that the existential sentence is true in $\mathbb{P}(\overline{x})[x]/f$, after substituting solutions in it is one equality and one inequality$\mathbb{P}(\bar{x})[x]/f \models h_1(\bar{x},y_f)=0\&h_2(\bar{x},y_f)\neq 0$, where $h_1(\bar{x},y),h_2(\bar{x},y)\in\mathbb{P}[\bar{x},y]$.

Then there is a tuple $(\overline{a},a)\in\mathbb{P}$ such that $h_1(\overline{a},a)\in A_f,h_2(\overline{a},a)\in A_f\setminus A_g$ is satisfied. Thus, $\mathbb{P}\models h_1(\bar{x},y_f)=0\&h_2(\bar{x},y_f)\neq 0$ is satisfied. Sufficiency, and with it the theorem has been proved.

Let $I(A_f)=\{g|g\in\mathbb{P}(\bar{x})[x],A_f\subseteq A_g\}$, where $f\in\mathbb{P}(\overline{x})[x]$.

PROPOSITION 1. Let $f(\overline{x},x)$ be an irreducible polynomial over a field $\mathbb{P}(\overline{x})$. Then the following two properties of the polynomial $f(\bar{x},x)$ are equivalent:

a) If an arbitrary polynomial $g(\overline{x},x)$ is not divisible by $f(\overline{x},x)$ then there is a tuple $(\overline{a},a)\in\mathbb{P}$ that satisfies $g(\overline{a},a)\in A_f\setminus A_g$;

b) The equality $I(A_f)=(f)$ is fulfilled.

Proof. $a)\Rightarrow b)$. Definitely, $I(A_f)\supseteq(f)$. Let $g\in I(A_f)$ and $g\not\in(f)$, moreover, n, then by assumption $a)$ there is a set $(\overline{a},a)\in A_f$ such that $g(\overline{a},a)\neq 0$ is a contradiction. So, $I(A_f)\subseteq(f)$.

$b)\Rightarrow a)$. Let $g(\overline{x},x)$ not be divisible by $f(\overline{x},x)$. According to the condition $I(A_f)=(f)$. From here $g(\overline{x},x)\not\in I(A_f)$ and hence there is a tuple $(\overline{a},a)\in\mathbb{P}$, which is done $g(\overline{a},a)\in A_f\setminus A_g$. The proposition has been proved.

Here is one necessary property of the companion $\mathbb{P}(\overline{x})[x]/f$ of the field $\mathbb{P}$.

PROPOSITION 2. Let $f(\overline{x},x)$ be an irreducible polynomial over a field $\mathbb{P}(\overline{x})$. Then, if the algebraic extension $\mathbb{P}(\overline{x})[x]/f$ of the field $\mathbb{P}(\overline{x})$ is a companion of $\mathbb{P}$,then each projection of the annihilator A_f is an infinite set.

Proof. Assume the opposite, and let the projection A_f be, for example, finite in the variable x_1, i.e.$A_f^1=\{(c_1,\dots,c_k)|\exists\bar{b}_1,\dots,\bar{b}_k)|(c_1,\bar{b}_1),\dots,(c_k,\bar{b}_k)\in A_f,\bar{b}_i=(b_{1i},\dots,b_{ni}),b_{ji},c_i\in\mathbb{P}\}$Then it is fulfilled: $\frac{\mathbb{P}(\bar{x})[x]}{f}|=\exists u_1,\dots,u_n u(f(u_1,u_2,\dots,u_n,u)=0\underset{i}{\&\&}u_1\neq c_i)$ but the same sentence is false in $\mathbb{P}$. Contradiction. In the case when A_f is empty, the same proposition is true in $\mathbb{P}(\overline{x})[x]/f$ but false in $\mathbb{P}$. The proposition is proved.

In the case of a simple algebraic extension $\mathbb{P}(x_1)[x]/f$ of the field $\mathbb{P}(x_1)$, Proposition 2 is inverted.

PROPOSITION 3. Let $f(x_1,x)$ be an irreducible polynomial over a field $\mathbb{P}(x_1)$. Then, an algebraic extension $\mathbb{P}(x_1)[x]/f$ from the field $\mathbb{P}(x_1)$ is a companion of $\mathbb{P}$, if and only if each projection of the annihilator A_f onto each of the coordinate axes Ox_1, Ox is an infinite set.

Proof. The necessity was proved in Proposition 2.

Sufficiency. By Proposition 1 and Theorem 2, it suffices to prove the equality $I(A_f)=(f)$. It's obvious that $I(A_f) \supseteq (f)$. Let us prove the inclusion $I(A_f) \subseteq (f)$

Suppose, $I(A_f) \not\subseteq (f)$, and $g(x_1,x) \in I(A_f) \setminus (f)$. Let $d(x_1,x)$ be the greatest common divisor of polynomials $g(x_1,x)$ and $f(x_1,x)$ over a field $\mathbb{P}(x_1)$. Note that due to the fact $f(x_1,x)$ that the irreducible polynomial $d(x_1,x)$ is an element of the field $\mathbb{P}(x_1)$,we denote it by $d(x_1)$. There are polynomials $p(x_1,x), q(x_1,x) \in \mathbb{P}(x_1)[x]$, such that the equality $p(x_1,x)g(x_1,x)+q(x_1,x)f(x_1,x)=d(x_1)$ is satisfied in the ring $\mathbb{P}(x_1)[x]$. Since $A_g \supseteq A_f$, and by condition, the projection of A_f onto the coordinate axis Ox_1 is an infinite set, it follows from the last representation of the polynomial $d(x_1)$ in the variable x_1 that it has an infinite set of zeros. Contradiction, sufficiency and with it the proposition have been proved.

Let us give a criterion for the mismatch of the ideals $I(A_f)$ and (f).

PROPOSITION 4. Let $f \in \mathbb{P}(\overline{x})[x]$ be an irreducible polynomial over a field $\mathbb{P}(\overline{x})$. The ideals $I(A_f)$ and (f) do not match with $I(A_f) \neq (f)$ if and only if there exists a polynomial $c(\overline{x}) \in \mathbb{P}[\overline{x}]$ such that, to the Cartesian power $\mathbb{P}^{n+1}$ $c(\overline{x}) \in I(A_f)$ is satisfied, i.e. the cylindrical surface A_c in affine space $\mathbb{P}^{n+1}$ contains A_f.

Proof. Necessity. Let be $I(A_f) \neq (f)$. Since $I(A_f) \supseteq (f)$ is always satisfied, then $I(A_f) \not\subseteq (f)$ takes place. Then let be $g(\overline{x},x) \in I(A_f) \setminus (f)$.

Since $f(\overline{x},x)$ the field $\mathbb{P}(\overline{x})$, is irreducible, the greatest common divisor c of polynomials f and g can be represented as $u(\bar{x},x)f(\bar{x},x) + v(\bar{x},x)g(\bar{x},x) = c(\bar{x})$, where $u(\bar{x},x), v(\bar{x},x) \in \mathbb{P}[\bar{x},x], c(\bar{x}) \in \mathbb{P}[\bar{x}]$. From the last relation we deduce that $c(\overline{x}) \in I(A_f)$. The necessity has been proved.

Sufficiency. Let be $c(\overline{x}) \in I(A_f)$ and $I(A_c) \supseteq I(A_f)$. We have a polynomial $c(\overline{x})$ as a polynomial of zero degree in x is not divisible by a polynomial $f(\overline{x},x)$ of degree not less than the first in the same variable, therefore $c(\overline{x}) \in I(A_c) \setminus I(A_f)$.

Sufficiency has been proved.

Consider an example of the mismatch of ideals $I(A_f)$ and (f).

EXAMPLE 1. An example of a simple algebraic extension of the non-companion field of rational numbers. Consider in an affine space $\mathbb{Q}^3$ the curve S, given by the intersection of the cylinder $x^2 + y^2 - 1 = 0$ and the plane $x + y + z = 0$.

The curve S over the field $\mathbb{Q}$ can be equivalently given as the annihilator of $A_f = \{(a,b,c) | f(a,b,c) = 0, a,b,c \in \mathbb{Q}\}$, of the polynomial $f(x,y,z) = (x^2 + y^2 - 1)^2 + (x+y+z)^2$ over the field $\mathbb{Q}$. Let us write the polynomial $f(x,y,z)$ in powers of the variable z : $f(x,y,z) = z^2 + 2(x+y)z + x^4 + y^4 + 2x^2y^2 - x^2 - y^2 + 2xy + 1$. Let us prove that $f(x,y,z)$ is irreducible. Suppose that $f(x,y,z) = (z - p(x,y))(z - q(x,y))$. Obviously $p(x,y) \neq q(x,y)$, , then for a pair $(a,b) \in \mathbb{Q}$ such that $p(a,b) \neq q(a,b)$ is fulfilled by $f(a,b,p(a,b)) = 0$ and $f(a,b,q(a,b)) = 0$. Since from the equation $x+y+z=0$, the value of $c=-a-b$ is uniquely determined, then $p(a,b) = q(a,b)$. A contradiction, thus $f(x,y,z)$ is irreducible.

Thus, the cylindrical surface A_g where $g = x^2 + y^2 - 1$ in the affine space $\mathbb{Q}^3$ contains A_f, therefore, $I(A_f) \neq (f)$ and by Proposition 1 and Theorem 2, we obtain a simple extension $\mathbb{Q}(x,y)[z]/f$ of the field $\mathbb{Q}(x,y)$ that is not a companion of the field $\mathbb{Q}$.

An immediate consequence of Proposition 1 and Theorem 2 is the following description, in terms of ideals, of a simple algebraic extension $\mathbb{P}(\bar{x})[x]/f$ of the field $\mathbb{P}(\bar{x})$, that is a companion of the field $\mathbb{P}$.

THEOREM 3. Let $f(\bar{x},x)$ be an irreducible polynomial over a field $\mathbb{P}(\bar{x})$. An algebraic extension $\mathbb{P}(\bar{x})[x]/f$ of the field $\mathbb{P}(\bar{x})$ is a companion $\mathbb{P}$ if and only if the ideal $I(A_f)$ is the same as the ideal (f).

Algebraic extensions

Let $\mathbb{P}(\bar{x})[y]/f$ and $\mathbb{P}(\bar{x})[y]/f/g$ (here $\mathbb{P}(\bar{x})[y]/f/g = (\mathbb{P}(\bar{x})[y]/f)[z]/g$ be simple algebraic extensions of the fields $\mathbb{P}(\bar{x})$ and $\mathbb{P}(\bar{x})[y]/f$ respectively, and be irreducible polynomials over the fields $\mathbb{P}(\bar{x})$ and $\mathbb{P}(\bar{x})[y]/f$ respectively. Let be $I(A_{fg}) = \{ h | h \in \mathbb{P}(\bar{x})[y,z], A_{fg} \subseteq A_h\}$, $A_{fg} = \{(\bar{a},b,c) \in \mathbb{P} | (\bar{a},b) \in A_f, (\bar{a},b,c) \in A_g\}$

It is obvious that $I(A_{fg})$ is an ideal in the ring $\mathbb{P}(\bar{x})[y,z]$, generated by polynomials $f(\bar{x},y)$ и $g(\bar{x},y,z)$ i.e. $I(A_{fg}) = (f,g)$.

Consider now an algebraic extension of a simple algebraic extension of the field $\mathbb{P}(\bar{x})$.

THEOREM 4. The algebraic extension $\mathbb{Q}(\bar{x})[y]/f/g$ of the field $\mathbb{P}(\bar{x})[y]/f$ is a companion $\mathbb{P}$ if and only if, for any polynomial $h(\bar{x},y,z) \in \mathbb{P}(\bar{x})[y,z]$ such that $h(\bar{x},y,z) \not\in (f,g)$ there is a tuple $(\bar{a},b,c) \in \mathbb{P}$, such that $(\bar{a},b,c) \in A_{fg} \setminus A_h$.

Proof. Necessity. In the algebraic extension $\mathbb{P}(\bar{x})[y]/f/g$ of the field $\mathbb{P}(\bar{x})$, the system $f(\bar{x},y_f) = 0 \,\&\, g(\bar{x},y_f,z_g)=0 \& h(\bar{x},y_f,z_g) \neq 0$ is satisfied; therefore, there is a tuple $(\bar{a},b,c) \in \mathbb{P}$ $(\bar{a},b,c) \in A_{fg} \setminus A_h$.

Sufficiency. Let $\mathbb{P}(\bar{x})[y]/f/g \models \exists u \ldots \exists v \varphi(\bar{x},y_f,z_g,u,\ldots,v)$ be fulfilled. Since $u,\ldots,v \in \mathbb{P}(\bar{x})[y]/f/g$ we assume that this formula is equivalent in the algebraic extension $\mathbb{P}(\bar{x})[y]/f/g$ of the field $\mathbb{P}(\bar{x})$ to the system $h_1(\bar{x},y_f,z_g)=0 \& h_2(\bar{x},y_f,z_g) \neq 0$. Then, there is a tuple $(\bar{a},b,c) \in \mathbb{P}$ such that $(\bar{a},b,c) \in A_{fg} \setminus A_h$. The necessity, and with it the theorem, has been proved.

THEOREM 5. An algebraic extension $\mathbb{Q}(\bar{x})[y]/f/g$ of a field $\mathbb{P}(\bar{x})[y]/f$ is a companion of $\mathbb{P}$ if and only if the ideal $I(A_{fg})$ is the same as the ideal (f,g).

Proof. Necessity. Let be $h(\bar{x},y,z) \not\in (f,g)$. Then, in the algebraic extension $\mathbb{P}(\bar{x})[y]/f/g$ of the field $\mathbb{P}(\bar{x})$ the system $f(\bar{x},y_f) = 0 \& g(\bar{x},y_f,z_g)=0 \& h(\bar{x},y_f,z_g) \neq 0$ is satisfied. Hence, in the companion $\mathbb{P}$ there is a tuple $(\bar{a},b,c) \in \mathbb{P}$, so that $(\bar{a},b,c) \in A_{fg} \setminus A_h$ and $h(\bar{a},b,c) \notin (f,g)$ hence. If $h(\bar{x},y,z) \in (f,g)$, then obviously $h(\bar{x},y,z) \in I(A_{fg})$. The necessity has been proved.

Sufficiency. Let $\mathbb{P}(\bar{x})[y]/f/g \models \exists u \ldots \exists v \varphi(\bar{x},y_f,z_g,u,\ldots,v)$ be fulfilled. Since $u,\ldots,v \in \mathbb{P}(\bar{x})[y]/f/g$ we will assume that this formula is equivalent in the algebraic extension $\mathbb{P}(\bar{x})[y]/f/g$ of the field $\mathbb{P}(\bar{x})$ to the system $h_1(\bar{x},y_f,z_g)=0 \& h_2(\bar{x},y_f,z_g) \neq 0$. By definition, it follows from $h_2(\bar{x},y_f,z_g) \neq 0$ that $h_2(\bar{x},y,z) \notin I(A_{fg})$. Then it follows from the equality $I(A_{fg}) = (f,g)$, that there is a tuple $(\bar{a},b,c) \in \mathbb{P}$, such that $(\bar{a},b,c) \in A_{fg} \setminus A_h$ and satisfies $\mathbb{P} | = h_1(\bar{a},b,c)=0 \& h_2(\bar{a},b,c) \neq 0$. Sufficiency, and with it the theorem has been proved.

Let us formulate a description of the companions of the field $\mathbb{P}$ in the general case.

Let $B = \{\beta_1, \beta_2, \ldots\}, X = \{x_1, x_2, \ldots\}$ be countable sets of independent variables, $\bar{\beta} = (\beta_1, \ldots, \beta_m)$, $\bar{x}_n = (x_1, \ldots, x_n)$, $\bar{f}_n = (f_1, \ldots, f_n)$, where $f_i(\bar{\beta}, \bar{x}_{i-1}^{\bar{f}_{i-1}}, x_i)$ is irreducible in the ring $\mathbb{P}(\bar{\beta})[\bar{x}_{i-1}^{\bar{f}_{i-1}}][x_i]$, where $\bar{x}_i^{\bar{f}_i} = (x_1^{f_1}, \ldots, x_i^{f_i})$, $x_i^{f_i}$ is the root of the polynomial $f_i(\bar{\beta}, \bar{x}_{i-1}^{\bar{f}_{i-1}}, x_i) \in \mathbb{P}(\bar{\beta})[\bar{x}_{i-1}^{\bar{f}_{i-1}}][x_i]$ over the field $f_i(\bar{\beta}, \bar{x}_{i-1}^{\bar{f}_{i-1}}, x_i) \in \mathbb{P}(\bar{\beta})[\bar{x}_{i-1}^{\bar{f}_i}$ $\bar{\beta})[\bar{x}_i^{\bar{f}_i}]$ is defined as follows. Let's put $\mathbb{P}(\bar{\beta})[\bar{x}_1^{\bar{f}_1}] = \mathbb{P}(\bar{\beta})[x_1]/f_1(\bar{\beta}, x_1)$, $\mathbb{P}(\bar{\beta})[\bar{x}_2^{\bar{f}_2}] = \mathbb{P}[\bar{\beta}][\bar{x}_1^{\bar{f}_1}][x_2]/f_2(\bar{\beta}, \bar{x}_1^{\bar{f}_1}, x_2)$. We define $\mathbb{P}(\bar{\beta})[\bar{x}_n^{\bar{f}_n}] = \mathbb{P}(\bar{\beta})[\bar{x}_{n-1}^{\bar{f}_{n-1}}][x_n]/$

$f_n(\bar{\beta}, \bar{x}_{n-1}^{\bar{f}_{n-1}}, x_n)$ by induction. Thus, in the sequence $\mathbb{P}(\bar{\beta})[\bar{x}_1^{\bar{f}_1}], \mathbb{P}(\bar{\beta})[\bar{x}_2^{\bar{f}_2}], \ldots, \mathbb{P}(\bar{\beta})[\bar{x}_n^{\bar{f}_n}]$ – each subsequent field $\mathbb{P}(\bar{\beta})[\bar{x}_{i+1}^{\bar{f}_{i+1}}]$ is a simple algebraic extension of the previous field by means of an irreducible polynomial $f_{i+1}(\bar{\beta}, \bar{x}_i^{\bar{f}_i}, x_{i+1})$. We define the corresponding ideals $I(A_{\bar{f}_n}) = \{ h \in \mathbb{P}(\bar{\beta})[\bar{x}_n^{\bar{f}_n}] | A_{\bar{f}_n} \subseteq A_h\}, A_{\bar{f}_n} = \{(\bar{a}, \bar{b}_n) \in \mathbb{P}? | (\bar{a}, b_{,1}) \in A_{f_1}, \ldots, (\bar{a}, b_1, \ldots, b_n) \in A_{f_n}, \bar{b}_n = (b_1, \ldots, b_n)\}$, where each $f_i \in \mathbb{P}(\bar{\beta})[\bar{x}_{i-1}^{\bar{f}_{i-1}}][x_i], i = 1, \ldots, n$ is irreducible over the corresponding field $\mathbb{Q}(\bar{\beta})[\bar{x}_{i-1}^{\bar{f}_{i-1}}]$.

Let us give a general description of the companions of the field $\mathbb{P}$.

THEOREM 6. An algebraic extension $\mathbb{P}(\bar{\beta})[\bar{x}_n^{\bar{f}_n}] = \mathbb{P}(\bar{\beta})[\bar{x}_{n-1}^{\bar{f}_{n-1}}][x_n]/f_n(\bar{\beta}, \bar{x}_{n-1}^{\bar{f}_{n-1}}, x_n)$ of a field $\mathbb{P}(\bar{\beta})$ is a companion $\mathbb{P}$ if and only if the ideal $I(A_{\bar{f}_n})$ coincides with the ideal $(f_1, \ldots, f_n)$.

The proof is a general reproduction of the proof of Theorem 5.

Discussion of results

The above results give a fairly complete description of the companions of the fields of rational and real numbers. Construction methods can be used for further studies of field companions and their classes.

Conclusion

The general theory of Fraisse's companion classes and their theories, developed by A.T. Nurtazin, constitutes a separate new area in model theory. This approach, applied to specific classical structures and their theories, provides new tools for the study of these objects. The study of the companion class of rational and algebraic real number fields reveals companion fields containing transcendental and possibly algebraic elements with special properties of polynomials defining these elements. The companions of each of the above-named fields are algebraic extensions of the fields of quotients of a certain set of independent variables over the corresponding field, using mutually agreed polynomials.

Acknowledgments

This work was carried out at the Institute of Information and Computational Technologies with the support of the Committee of Science of the Ministry of Education and Science of the Republic of Kazakhstan (Grant no. AP08856114 Companion Theory).

References

1. Barwise J. Robinson A. (1970) Completing theories by forcing, Ann. Math. Logic, 2:119-142. DOI: 10.1016/0003-4843(70)90008-2 (in English).
2. Robinson A. (1951) On the Metamathematics of Algebra. Amsterdam, North-Holland, 540.
3. Belegradek O.V. (1974) Algebraically closed groups, Algebra i Logika, 13:239- 255. DOI: 10.1007/BF01463347 (in Russian).
4. Cohen P.J. (1966) Set Theory and the Continuum Hypothesis. NY, Benjamin, 467.
5. Ershov Yu.L., Palyutin E.A., Taimanov A.D. (1982) Model Theory, A Handbook of Mathematical Logic. Moscow, 492.
6. Fraisse R. (1955) Sur quelques classifications des systemes de relations, Publ.scient. de l'univ. d'Algers, 35-182 (in English).
7. Macintyre A. (1972) On algebraically closed groups, Ann. Math., 96:53-97. DOI: 10.2307/1970894 (in English).
8. Macintyre A. (1972) Omitting quantifier-free types in generic structures, Journal of Symbolic Logic, 37: 512 – 520. DOI: 10.2307/2272737 (in English).
9. Nurtazin A.T. (2016) Countable infinite existentially closed models of universally axiomatizable theories, Siberian Advances in Mathematics, 26: 99-125. DOI: 10.3103/S1055134416020036 (in English).
10. Nurtazin A.T. (2018) Properties of Existentially Closed Models [Svojstva jekzistencial'no zamknutyh modelej], Algebra i Logika, 57: 321–327 (in Russian).
11. Nurtazin A.T. (2018) Properties of exictentionally cloused companions, Algebra and Logic, 57: 211–221 (in English).

12. Nurtazin A.T. (2018) Forcing formulas in Frase structures and classes [Vynuzhdenie formul v strukturah i klassah Frjese], Algebra i Logic, 57: 567–586 (in Russian).

13. Nurtazin A.T. (2018) Forcing formulas in Fraise structures and classes, Algebra and Logic, 57: 368–380 (in English).

14. Nurtazin A.T. (2015) Countable Existentially Closed Models of Universally Axiomatizable Theories [Schetnye jekzistencial'no zamknutye modeli universal'no aksiomatiziruemyh teorij], Matematicheskie Trudy, 18: 48-97 (in Russian).

15. Nurtazin A.T. (2017) Introduction to model theory, quantifier elimination and existential closure [Vvedenie v teoriju modelej, jeliminacija kvantorov i jekzistencial'naja zamknutost'], Almaty: NTs GNTE, 87 (in Russian).

16. Nurtazin A.T. (2018) Any forcing type is implemented in some forcing model. Fourteenth intl. Asian school-seminar "Problems of optimization of complex systems", Issyk-Kul, Kyrgyzstan. 2018. . 109–113 (in Russian).

17. Khisamiev Z.G., Alimzhanova S.A. (2019) Companions of the ring of integers. Mater.scient.conf. IIVT MES RK "Modern problems of informatics and computing technologies", Almaty, Kazakhstan. 2019. P.361–365 (in Russian).

Funded by Al-Farabi KazNU

Contents